SYNTHESIS, STRUCTURAL AND MAGNETIC PROPERTIES OF $Ni_xCo_{1-x}Fe_2O_4$ AND $Co(RE)_{0.1}Fe_{1.9}O_4$ NANO-FERRITES

by

Bongani Ndlovu

BSc, BSc (Hons) (UKZN)

Submitted in fulfilment of the academic requirements for the degree of Master of Science in Physics in the School of Chemistry and Physics, University of KwaZulu-Natal, Durban, South Africa.

April 2017

Abstract

$Ni_xCo_{1-x}Fe_2O_4$ ($x = 0$ to 1 incremented by 0.1) nanoferrites were prepared by the glycol-thermal technique at 200 °C. Formation of single phase cubic spinel structure was confirmed by X-ray diffraction (XRD) data for nearly all the compounds, except $x = 0.7$ to 0.9 which had small impurity phases that were suspected to be due to NiFe formation. The particle or crystallite sizes range from about 8 nm to 14 nm across the composition range. ^{57}Fe Mössbauer spectra measured from 80 K to room temperature were fitted with two sextets and one doublet. We associate the sextets and doublet with magnetically ordered and paramagnetic state Fe^{3+} ions respectively. Paramagnetic state is observed for $x = 0.7$ to 0.9 at room temperature. At 80 K, the hyperfine fields and isomer shifts are more enhanced which demonstrate an increased magnetic ordered. The hyperfine fields for the sample $x = 0.1$ decrease from about 536 kOe at 80 K to 0 kOe at 483 K. A total collapse in magnetic order occurs at about 478 K. Room temperature magnetization measurements performed on a vibrating sample magnetometer (VSM) show a reduction in coercive fields with increased x due to smaller anisotropy of Ni than Co. Energy dispersive X-ray (EDX) analysis confirmed the stoichiometric presence of Ni, Co and Fe atoms on the samples $x = 0.3$ and 0.5 which were further annealed up to 1100 °C. High resolution transmission electron microscopy (HRTEM) data confirmed the XRD results which show increasing cryatallite sizes from about 13 nm to 110 nm after annealing at 1100 °C. Mössbauer spectra revealed a general increase in hyperfine fields with increasing crystallite size which is attributed to stronger superexchange interactions as a result of enhanced particle size. Higher coercivity for larger particles indicates transition from single to multi-domain structure. $Co(RE)_{0.1}Fe_{1.9}O_4$ (RE = Ce, Nd, Sm, Gd, Dy, Er and Yb) nanoferrites were also synthesized by the glycol-thermal technique. Single phase formation was confirmed by XRD data which also revealed crystallite sizes between 8 nm and 14 nm. A decrease in the hyperfine fields and coercivity is observed on substitution of the magnetic Fe^{3+} ions, in $CoFe_2O_4$, with the non-magnetic RE^{3+} ions which is expected. This study has shown strong correlation between coercivity and particle sizes with sample preparation pressure which demonstrates a strong connection between the magnetic properties, crystallite

size and the sample preparation conditions. Some preliminary four probe resistivity measurements in the temperature region 25 °C to 130 °C on pellet samples annealed at 1100 °C are reported which show evidence of semiconducting behaviour. These results also show significant differences in the resistivities determined from each face of a pellet.

Preface

The research contained in this dissertation was completed by the candidate while based in the Discipline of Physics, School of Chemistry and Physics, College of Agriculture, Engineering and Science, University of KwaZulu-Natal, Westville campus, South Africa. The contents of this work have not been submitted in any form to another university and, except where the work of others is acknowledged in the text, the results reported are due to investigations by the candidate.

Signed: _____   Date: April 2017

Name: Bongani Ndlovu

College of Agriculture, Engineering and Science
Declaration 1 - Plagiarism

Bongani Ndlovu declares that

1. The research reported in this dissertation, except where otherwise indicated, is my original research.

2. This dissertation has not been submitted for any degree or examination at any university.

3. This dissertation does not contain other person's data, pictures, graphs or other information, unless specifically acknowledged as being sourced from other persons.

4. This dissertation does not contain other persons writings, unless specifically acknowledged as being sourced from other researchers. When other written sources have been quoted, then:

5. Their words have been re-written but general information attributed to them has been referenced.

6. Where their exact words have been used, their writing has been placed in italics and inside quotation, and referenced.

7. This dissertation does not contain text, graphics or tables copied and pasted from internet, unless specifically acknowledged, and the source being detailed in the dissertation and in the reference sections.

Declaration 2

Publications based on current work

1. Msomi J.Z., **Ndlovu B.**, Moyo T. and Osman N.S.E.. Mössbauer and magnetic properties of annealed $Ni_xCo_{1-x}Fe_2O_4$ nanoparticles. *Journal of Alloys and Compounds*, 683, pp.$149 - 156$, 2016.

2. **Ndlovu B.**, Msomi J.Z. and Moyo T.. Structural and magnetic properties of $Ni_xCo_{1-x}Fe_2O_4$ synthesized by glycol-thermal method. *Submitted* 2017.

3. **Ndlovu B.**, Moyo T. and Msomi J.Z.. Synthesis, structural and magnetic properties of $Co(RE)_{0.1}Fe_{1.9}O_4$ nanoferrites. *In preparation* 2017.

Signed: _____   Date: April 2017

Name: Bongani Ndlovu

Dedication

I dedicate this dissertation to each one of my family members, especially my parents (Mr Mhlushwa and Mrs Thembile Ndlovu) and my brothers (Mlungisi, Mthobisi and Nkosikhona Ndlovu). Ngithi "Ndlovu, Gatsheni, Boya Benyathi..." without your encouragement, support and patience, I couldn't have achieved as much as I have. To my kids Asemahle, Sizwe and their mother Thobekile who have supported me throughout this project.

Contents

Acknowledgements

I'd like to extend my sincerest thanks to my supervisor Dr Thomas Moyo for making it possible for me to do this project. His guidance and support have been much appreciated. The words of wisdom that went beyond "magnetic materials and Mössbauer" to life in general have certainly been excellent. I would also like to thank my co-supervisor Dr Zakhele Msomi for all the support and encouragement that always made me feel I could do it. I would also like to express my appreciation to my colleagues Ntlakanipho Ngwane for being a good friend to me, Nokwanda Ngema for keeping me company in the laboratory while doing measurements and Dr Nadir Osman for his academic support and friendship. Most importantly, I would like express my gratitude to Sasol Ltd for funding this project.

List of Figures

xiii

List of Tables

Chapter 1

Introduction

1.1 Spinel ferrite structure

Spinel ferrites are metal oxides of the form AB_2O_4 where A and B are divalent and trivalent metals or each could be a combination thereof. Figure 1.1 shows the spinel structure. There are two sublattices that are coordinated by oxygen anions in the face centered cubic (fcc) positions, the tetrahedral (A) and the octahedral (B) sites. The metal ions can occupy either the A or B sites, depending on whether the spinel type is normal, inverse or mixed [1]. The spinel ferrite may be represented in the form $M\text{Fe}_2O_4$ where M is a divalent metal. A normal spinel occurs when the M^{2+} ions fully occupy the tetrahedral site which may be represented as $[M^{2+}][\text{Fe}_2^{3+}]O_4^{2-}$. An example of a simple spinel is ZnFe_2O_4 [2]. The inverse spinel occurs when all the M^{2+} ions occupy the octahedral site and the Fe^{3+} ions split between the tetrahedral and octahedral sites which can be represented as $[\text{Fe}^{3+}][M^{2+}\text{Fe}^{3+}]O_4^{2-}$. The examples of an inverse spinel is NiFe_2O_4 and basically CoFe_2O_4 which is partially inverse [1, 3]. The mixed spinel structure occurs when each of the M^{2+} and Fe^{3+} ions occupy both the tetrahedral and octahedral sites. The mixed spinel may be represented by the chemical formula $[M_{1-\delta}^{2+}\text{Fe}_\delta^{3+}][M_\delta^{2+}\text{Fe}_{2-\delta}^{3+}]O_4^{2-}$ where δ is the degree of inversion. MnFe_2O_4 is an example of a mixed spinel. The Ni-Co ferrite has also been found to have a mixed spinel structure [3]. In the current work we have studied the evolutions of the structural, magnetic and electrical properties as the Co^{2+} cations in CoFe_2O_4 are substituted by the Ni^{2+} ions. We also investigated this evolution when a fraction
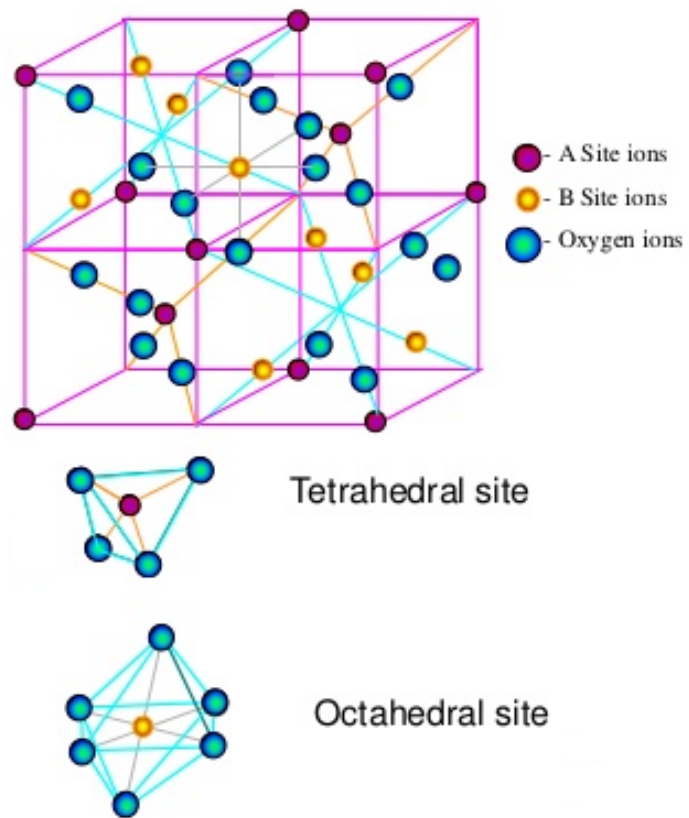
Figure 1.1: Crystal structure of spinel [4].

of the Fe^{3+} ions in $CoFe_2O_4$ were substituted with the rare-earth metal ions (RE^{3+}). The type of structure that forms depends on the ions that are present but may also be influenced by the preparation technique used to produce the samples.

1.2   Synthesis technique

Ferrites are classified in terms of their particle size as bulk or nanomaterials with the latter in the range 1 - 100 nm [1]. Nanomaterials have gained a lot of scientific research attention recently due to their interesting structural, magnetic and electrical properties [1, 5–7]. The properties of nanoferrites depend not only on the type of ions involved but also on the synthesis technique used to prepare them. The synthesis technique that is chosen is dependent on a variety of factors ranging from the desired properties of the products, available resources to the cost of production.

A number of techniques have been employed in the production of nanoparticles over the years and each have their own advantages and disadvantages. Tavakoli *et al.* [8] have reviewed the wet chemistry synthesis methods like chemical vapor condensation (CVC), arc discharge, microemulsion, hydrothermal, sol-gel, sonochemical, microbial and also by mechanical ball milling. A method like ball milling requires a lot of energy and may also introduce some impurities in the final product. The wet chemical synthesis techniques produce fine powders which in many cases require further sintering at elevated temperatures in order to form single phase compounds [3, 5, 6]. The annealing of the samples have been found to increase the particle sizes of the materials [9], which may sometimes not be desirable.

In this work we have synthesized our samples using the glycol-thermal technique. At 200 °C, this is a low temperature wet chemistry technique which produces single phase nanoparticles directly without the requirement of further sintering [9, 10]. High purity chlorides or nitrates are mixed together in deionized water and washed several times until all the impurities are removed before a reaction is conducted in ethylene glycol at 200 °C and high pressure. Further details of the glycol-thermal technique are discussed in section 3.2.

1.3 Magnetic properties

The magnetic properties in ferrites are very much dependent on their spinel structure and also on the cations involved in the A and B sites. In the absence of an externally applied magnetic field, ferrites behave ferrimagnetically due to the antiparallel arrangement of the unequal A and B sublattices which then gives rise to a non-zero net magnetization [1]. Ferrimagnets behave paramagnetically above a critical temperature called Curie temperature T_C. Paramagnetism is the disordered arrangement of magnetic moments in a material. However, the nanoparticle ferrites have been observed to behave superparamagnetically below T_C [6, 10–12]. The nano-size of these ferrites creates single domain structure in which the thermal fluctuations within the structure cause each particle to behave paramagnetically even below T_C. At lower temperature below a blocking temperature T_B, superparamagnetism disappears [13]. The understanding of magnetic ordering in solids, discussed in Chapter 2, is key to the analysis and the interpretation of the experimental findings in this work.

1.4 Electrical properties

Ferrites have been found to have semiconductor behaviour [14]. The electrical resistivity in ferrites depends on the cation distribution on the A and B sites. Gul *et al.* [15, 16] explained the mechanism of conduction, which is a reciprocal of resistivity, as the electron movement from a divalent to a trivalent ion of the same element (e.g. between Fe^{2+} and Fe^{3+} in $FeFe_2O_4$) in the lattice. In another proposed conduction mechanism for ferrites, conduction is said to be through electrons and holes between charged and neutral grains. Abdallah *et al.* [17] have investigated the activation energy required for the two conduction mechanisms and found that the conduction through charged and neutral grains requires more activation energy to occur. The study of electrical resistivity of pellet nanoferrite samples also revealed different properties for different faces of the same pellet [18]. The annealed pellets in the current study were therefore tested for resistivity on both faces.

1.5 Applications

Nanoparticles have a range of practical applications in a variety of fields which include electronics, optical, magnetic and biomedical applications [19, 20]. The high permeability displayed by the nickel-zinc ferrites has allowed these materials to be used in inductors and electromagnetic wave absorbers [20]. The nanoparticle ferrites have also become the subject of interest in biomedicine in recent times. This is based on their nanosize enabling these particles to penetrate biological cells, viruses and proteins which have the sizes in the ranges of about 10-100 μm, 20-450 nm and 10-50 nm respectively [21]. Their magnetic nature enables the nanoparticles to be driven to the intended targets inside the body by controlled external magnetic fields. Ferrofluids which have been used in cancer treatments and drug delivery have been produced from nanoferrites like magnetite, $FeFe_2O_4$. However, the challenge with magnetite is that the Fe ions cannot be differentiated from haemoglobin in the blood. This has led to using MFe_2O_4 with M = Co, Ni, Mn and Zn as alternatives to Fe [22].

1.6 Motivation

We were motivated by the use of $CoFe_2O_4$ in biomedicine, which makes it one of the most important materials to study and understand for the benefit of human health. The role played by $CoFe_2O_4$ in biomedicine has been reported before [23]. Along with Ni, Mn and Zn ferrites, $CoFe_2O_4$ has been found to have the necessary chemical and physical properties for the purposes of biomedical applications which includes hyperthermia and magnetic resonance imaging (MRI) [22]. $CoFe_2O_4$ is known to be a hard magnet with a coercivity and magnetization of about 5.40 kOe and 80 emu/g at room temperature whereas $NiFe_2O_4$ is a soft magnet [3]. The nickel-substituted cobalt ferrites are also highly topical materials [3, 12, 24, 25]. The series $Ni_xCo_{1-x}Fe_2O_4$ was recently studied by Mozaffari *et al.* [24] and Choi *et al.* [3]. The samples were prepared by the sol-gel method and annealed at elevated temperatures.

In another study involving $CoFe_2O_4$, the effect of substituting a fraction of the

Fe^{3+} ions by the rare-earth (RE^{3+}) ions has been reported by Nikumbh *et al.* [5] who investigated the structural and magnetic properties of Co($RE)_x$Fe$_{2-x}$O$_4$. However, the reported samples appear to have some secondary phases and the rare earths seem not to be fully incorporated into the spinel structure. In the current study nickel and rare earth substituted cobalt nanoferrites, Ni$_x$Co$_{1-x}$Fe$_2$O$_4$ (where $x = 0.0$ to 1.0 in steps of 0.1) and Co($RE)_{0.1}$Fe$_{1.9}$O$_4$ (where $RE =$ Ce, Nd, Sm, Gd, Dy, Er, Yb) are prepared by the glycol-thermal technique with better quality samples. The aim is to investigate the variations in the structural, magnetic and electrical properties as the Ni content increases and the RE are incorporated in CoFe$_2$O$_4$. We are interested in finding the range of particle sizes, lattice parameters and XRD densities from the XRD measurements. The saturation magnetization and coercivity were determined from the M-H hysteresis loops. Electrical resistivity measurements were performed in order to determine the electrical resistivity properties like the energy band gaps for some of the samples.

1.7   Dissertation setup

The dissertation consists of seven chapters. Chapter 1 is the introduction where we have briefly outlined the properties of interest in ferrites and the approach to this current work. In chapter 2 we discuss some of the common magnetic properties in ferrites. The experimental approach and techniques are discussed in chapter 3. The results are reported and discussed in chapters 4, 5 and 6. The dissertation ends with the main concluding remarks in chapter 7.

Chapter 2

Magnetism and magnetic order in solids

2.1   Introduction

A discussion of magnetic order in solids requires an understanding of how magnetism originates in materials. To do this we study the origins of the magnetic moments and their relation to the quantization of angular momentum to which the magnetism of elementary particles is based. The magnetic moments are mainly associated with electrons. Those associated with the nuclei are relatively too small and can be ignored. So in this chapter we briefly discuss the electronic magnetic moments which give rise to magnetism in materials and then the different types of magnetic order in solids which are based on the arrangements of the magnetic moments.

2.2   The magnetic moment

The electronic orbital and spin angular momenta form the basis of the microscopic theory of magnetism [26]. Figure 2.1 shows an electron of mass m_e orbiting around a nucleus in an anticlockwise direction, creating a closed loop of radius r [27]. The current I, which flows in the opposite direction is given by

$$I = -\frac{ev}{2\pi r} \tag{2.2.1}$$
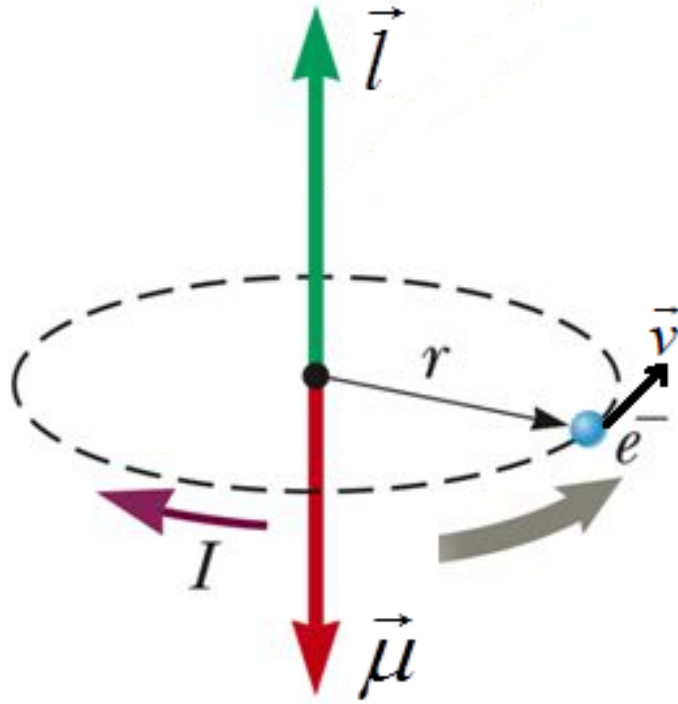
Figure 2.1: The electron orbitting a circular loop in an anticlockwise direction [27].

where e and v are the charge and speed of the electron respectively [26]. The magnetic moment $\boldsymbol{\mu}$ is given by

$$\boldsymbol{\mu} = I\boldsymbol{A} = -\frac{1}{2}e\boldsymbol{r}\times\boldsymbol{v} \tag{2.2.2}$$

where $\boldsymbol{A}$ is the area vector with a magnitude πr^2 [26]. Since the angular momentum $\boldsymbol{l}$ is defined as

$$\boldsymbol{l} = m_e \boldsymbol{r}\times\boldsymbol{v} \tag{2.2.3}$$

where m_e is the electron mass, the equation

$$\boldsymbol{\mu}_l = -\frac{e}{2m_e}\boldsymbol{l} = \gamma\boldsymbol{l}, \tag{2.2.4}$$

relates the orbital moment $\boldsymbol{\mu}_l$ to the angular momentum through the gyromagnetic ratio γ which is $-(e/2m_e)$ for electron orbit. The quantization of angular momentum in units of $\hbar$ (i.e., $l_z = m_l\hbar$) leads to the quantization of the magnetic moment such that a z-component of μ_l is given by

$$\mu_{l_z} = -\frac{e}{2m_e}m_l\hbar \tag{2.2.5}$$

8

where $m_l = 0, \pm 1, \pm 2, ...$ is the orbital magnetic quantum number [26]. Equation (2.2.5) may be written in terms of the Bohr magneton $\mu_B = 9.274 \times 10^{-24}$ A m^2 and the Landé g-factor as

$$\mu_{l_z} = -\mu_B g m_l. \qquad (2.2.6)$$

Here μ_B is defined by

$$\mu_B = \frac{e\hbar}{2m_e} \qquad (2.2.7)$$

and g has a value of 1 since this is a purely orbital moment.

The electron also possesses an intrinsic spin angular momentum with quantum number $s = \frac{1}{2}$ [26]. There exist a spin magnetic moment that is only associated with the spin of the electron. The gyromagnetic ratio for electron spin ($\gamma = -e/m_e$) is twice that of the orbital magnetic moment. The spin magnetic moment $\boldsymbol{\mu}_s$ is given by

$$\boldsymbol{\mu}_s = -\frac{e}{m_e}\boldsymbol{s} = \gamma\boldsymbol{s} \qquad (2.2.8)$$

where $\boldsymbol{s}$ is the spin angular momentum. Along any axis the component of $\boldsymbol{\mu}_s$ is $\pm\frac{1}{2}\hbar$. The z-component (which is equal to the other components) of spin magnetic moment is given by

$$\mu_{s_z} = -\frac{e}{m_e}m_s\hbar = -\mu_B g m_s \qquad (2.2.9)$$

where $m_s = \pm\frac{1}{2}$ is the spin magnetic quantum number and g has a value of 2.0023 for a purely spin moment [28]. In general an electron possesses both the orbital and spin moments and the total magnetic moment $\boldsymbol{\mu}$ is proportional to the total angular momentum $\boldsymbol{j}$ for a single electron,

$$\boldsymbol{\mu} = \gamma(\boldsymbol{l} + \boldsymbol{s}) = \gamma\boldsymbol{j} \qquad (2.2.10)$$

For a many-electron atom the total magnetic moment $\boldsymbol{\mu}_J$ is proportional to the total angular $\boldsymbol{J}$ momentum of an atom, which is the spin-orbit coupling of $\boldsymbol{L} = \sum_{i=1}^{n} \boldsymbol{l}_i$ and $\boldsymbol{S} = \sum_{i=1}^{n} \boldsymbol{s}_i$. The total magnetic moment in the direction of $\boldsymbol{J}$ is given by

$$\boldsymbol{\mu}_J = \gamma\hbar\boldsymbol{J} = -\mu_B g \boldsymbol{J} \qquad (2.2.11)$$

where g is the Landé equation [28]

$$g = 1 + \frac{J(J+1) + S(S+1) - L(L+1)}{2J(J+1)}. \qquad (2.2.12)$$

9

The magnitude of the magnetic moment μ_J may be calculated by

$$\mu_J = \mu_B g \sqrt{J(J+1)}. \tag{2.2.13}$$

2.3 Paramagnetism

In free atoms, the paramagnetic contribution to the magnetization results from the intrinsic spin and orbital angular momentum of the electrons. Magnetization $\boldsymbol{M}$ is defined as the sum of the magnetic moments per unit volume. However, due to the instability of volume with varying temperatures, $\boldsymbol{M}$ (written as $\boldsymbol{\sigma}$) is often expressed in terms of mass m of the sample as

$$\boldsymbol{\sigma} = \frac{1}{m} \sum_{i=1}^{n} \boldsymbol{\mu}_i. \tag{2.3.1}$$

The magnetization response of a material to an externally applied field $B = \mu_0 H$ is known as susceptibility χ which is given by

$$\chi = \frac{M}{H} \tag{2.3.2}$$

where H is the internal field of the macroscopic magnetic field intensity B and μ_0 is the permeability of free space. Materials with $\chi < 0$ are diamagnetic whereas those with $\chi > 0$ are paramagnetic [28]. Diamagnetism in free atoms results from field-induced magnetic moments.

Paramagnetism occurs in materials which possess a permanent magnetic moment. These include materials that have atoms or molecules with non-zero total spin (i.e., $S \neq 0$), transition and rare-earth elements as they have partially filled inner shells. Figure 2.2 shows a typical random arrangement of magnetic moments which is characteristic of paramagnetism in the absence of an externally applied field [29]. In the presence of an externally applied magnetic field the magnetic moments align themselves along the applied field.

2.3.1 Curie law

The applied magnetic field $\boldsymbol{B}$ splits the energy levels into

$$E_J = -\boldsymbol{\mu}_J \cdot \boldsymbol{B} = m_J g \mu_B B \tag{2.3.3}$$

10
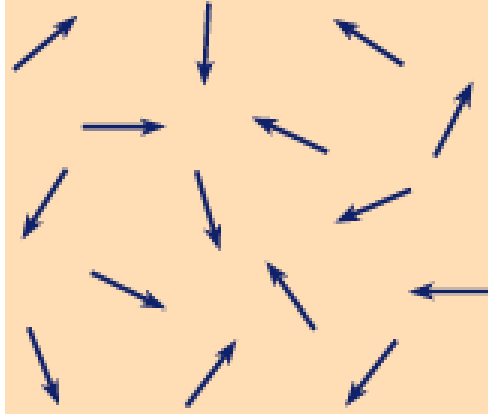
Figure 2.2: A random arrangement of magnetic moments in paramagnetism [29].

where $m_J = J, J - 1, ..., -J$ is the azimuthal quantum number. By Boltzmann's statistics the average magnetic moment over J energy states can be determined by

$$< \mu_J >= \frac{\sum_J \mu_J \exp(-E_J/k_B T)}{\sum_J \exp(-E_J/k_B T)} \quad (2.3.4)$$

where $k_B T$ is the thermal energy with k_B being the Boltzmann's constant and T the temperature [26]. A quantum extreme case which occurs when $S = \frac{1}{2}$ and $L = 0$ has $J = \frac{1}{2}$, $m_J = \pm\frac{1}{2}$ and $g = 2$. In this case the energy states have energies $E_J = \pm\mu_B B$ and the average magnetic moment becomes

$$< \mu_J >= g\mu_B J \tanh x \quad (2.3.5)$$

where $x = (\mu_B \mu_0 H)/(k_B T)$ is the ratio of the Zeeman energy to the thermal energy. For $x \ll 1$ and $\tanh x \approx x$, the magnetization M of n atoms per unit volume can be determined by

$$M = \frac{n\mu_B^2 \mu_0 H}{k_B T}. \quad (2.3.6)$$

Equation (2.3.6) gives the magnetization for a special case described above. However, in general there are $2J + 1$ energy levels for an angular momentum quantum number J and the magnetization is given by

$$M = ng\mu_B B_J(x) \quad (2.3.7)$$

where $B_J(x)$ is the Brillouin function given by

$$B_J(x) = \frac{2J + 1}{2J} \coth\left(\frac{(2J + 1)x}{2J}\right) - \frac{1}{2J} \coth\left(\frac{x}{2J}\right) \quad (2.3.8)$$

11

with $x = (gJ\mu_B\mu_0 H)/(k_B T)$. The magnetic susceptibility is then given by the Curie law as

$$\chi = \frac{M}{H} = \frac{\mu_0 g^2 \mu_B^2 n J(J+1)}{k_B T} = \frac{C}{T} \tag{2.3.9}$$

where $C = \mu_0 g^2 \mu_B^2 n J(J+1)/k_B$ is the Curie constant. In many experimental analysis an inverse of susceptibility is usually plotted against temperature (i.e., χ^{-1} versus T). This plot is a straight line through the origin for materials that obey Curie law. However, observations of experimental data of paramagnetic metals showed non-zero temperature intercept as shown in Figure 2.3 where (a) χ versus T and (b) χ^{-1} versus T is the fitted straight line of the actual data. This behaviour was explained
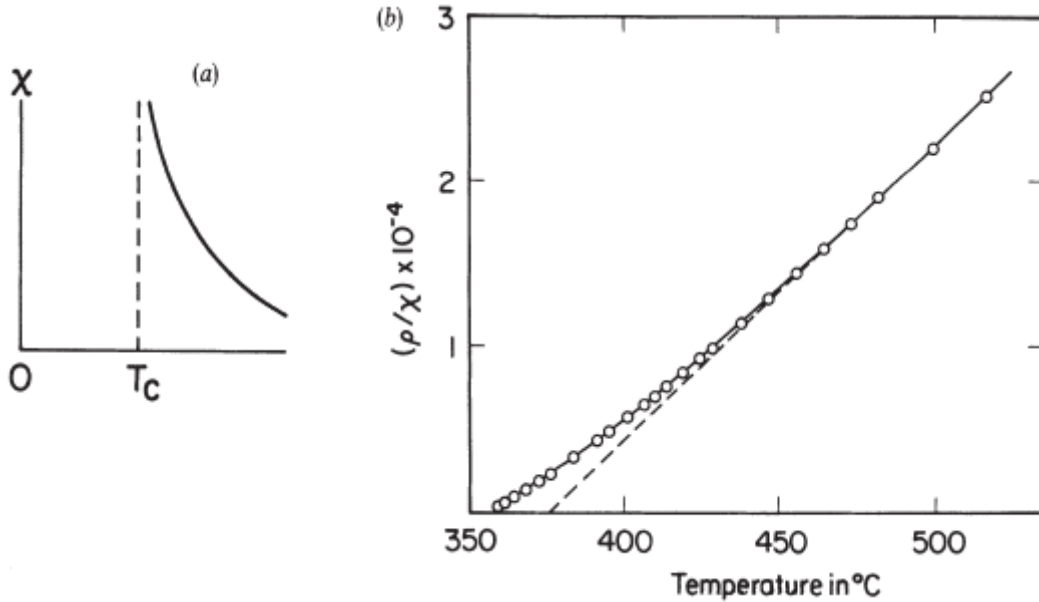
Figure 2.3: (a) Susceptibility against temperature and (b) inverse susceptibility against temperature. The material obeys Curie-Weiss law with the raw data fitted with a straight line [30].

by Weiss as due to the interaction between the magnetic moments which create a spontaneous magnetization within the material. His theory then lead to a more general susceptibility dependence on temperature which is known as the Curie-Weiss law

$$\chi = \frac{C}{T - \theta_p} \tag{2.3.10}$$

12

where θ_p is the critical temperature called paramagnetic Curie temperature [30]. When $\theta_p = 0$, the Curie-Weiss law becomes the Curie law in Equation (2.3.9). Curie-Weiss law will be revisited in the next section when the magnetic phase transitions are discussed.

2.4   Magnetic order in solids

In the previous section paramagnetism which displayed a random arrangement of the magnetic moments was discussed. In the following subsections, we pay attention to magnetic order where the magnetic moments are orderly arranged. The common magnetic states include ferromagnetism, antiferromagnetism, ferrimagnetism and superparamagnetism. Some materials can exist in more than one magnetic phase depending on the temperature. A ferromagnet and an antiferromagnet become paramagnetic above the the critical temperature known as the Curie point T_C and the Néel temperature T_N respectively.

2.4.1   Ferromagnetism

A ferromagnet has a spontaneous magnetization. This is because of the alignment of the magnetic moments even in the absence of an externally applied magnetic field as shown in Figure 2.4 [29]. The magnetic moments tend to align themselves in easy directions which depend on their location in the crystal structure. A ferromagnet exists in its magnetic phase below the Curie point and undergoes a magnetic phase transition to become paramagnetic above the Curie point. Examples of ferromagnets include transition metals like nickel (T_C = 358 °C), iron (T_C = 770 °C), cobalt (T_C = 1131 °C) and rare earth metals like gadolinium (T_C = 293 K), disprosium (T_C = 85 K) and erbium (T_C = 19.5 K) [30]. The theory of ferromagnetism, which was proposed by Weiss in 1906, considered that there was an enormous internal molecular field proportional to the ferromagnet's magnetization (i.e., $\lambda\boldsymbol{M}$ where λ is a proportionality constant) [26]. In this theory, the total internal field $\boldsymbol{H}^i$ is expressed as

$$\boldsymbol{H}^i = \lambda\boldsymbol{M} + \boldsymbol{H}. \qquad (2.4.1)$$

13
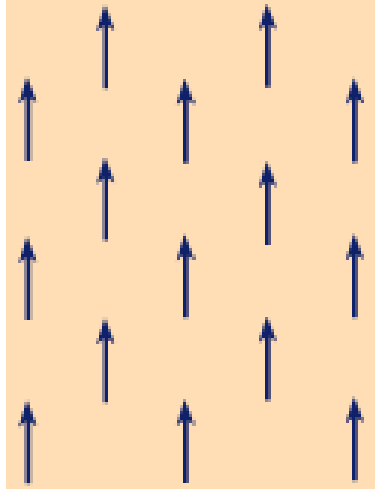
Figure 2.4: An ordered arrangement of magnetic moments in a ferromagnet [29].

where $\boldsymbol{H}$ is the applied field. The origin of λM is now known to be due to Coulomb interaction and the exclusion principle. The interaction between atoms is expressed by the Hamiltonian $\mathcal{H}$ given by

$$\mathcal{H} = -2\mathcal{J}\boldsymbol{S_1}.\boldsymbol{S_2} \tag{2.4.2}$$

where $\mathcal{J}$ is the exchange integral, $\boldsymbol{S_1}$ and $\boldsymbol{S_2}$ are operators describing the localized spins on two adjacent atoms. $\mathcal{J}$ is positive for ferromagnetic interaction and negative for antiferromagnetic interaction. Following a similar approach as in the case for paramagnetism, the magnetization of a ferromagnet can be expressed in terms of the Brillouin function

$$M = M_0 B_J(x) \tag{2.4.3}$$

where $M_0 = ng\mu_B J$ and $x = \mu_0\mu(\lambda M + H)/(k_B T)$. When the applied field is zero then M is made up of only the spontaneous magnetization M_s such that Equation (2.4.3) becomes

$$\frac{M_s}{M_0} = B_J(x_0) \tag{2.4.4}$$

where $x_0 = (\mu_0\mu\lambda M)/(k_B T)$. Using the $M_0 = ng\mu_B J$ defined above, the ratio M_s/M_0 can also be expressed as

$$\frac{M_s}{M_0} = \left(\frac{nk_B T}{\mu_0\lambda M_0^2}\right)x_0, \tag{2.4.5}$$

or for convenience as

$$\frac{M_s}{M_0} = \left(\frac{T(J+1)}{3JC\lambda}\right) x_0 \qquad (2.4.6)$$

where C is the Curie constant defined in Equation (2.3.9). To solve Equations (2.4.4) and (2.4.6) requires a numerical or a graphical solution. The graphical solution is the intersection of the graphs (noted as red circles) in Figure 2.5 for the case of $J = \frac{1}{2}$. Equation (2.4.6) is represented by the straight lines for temperatures $T > T_C$, $T = T_C$ and $T < T_C$. The dotted line intercept the M_s/M_0 axis at $H/\lambda M_0$ when
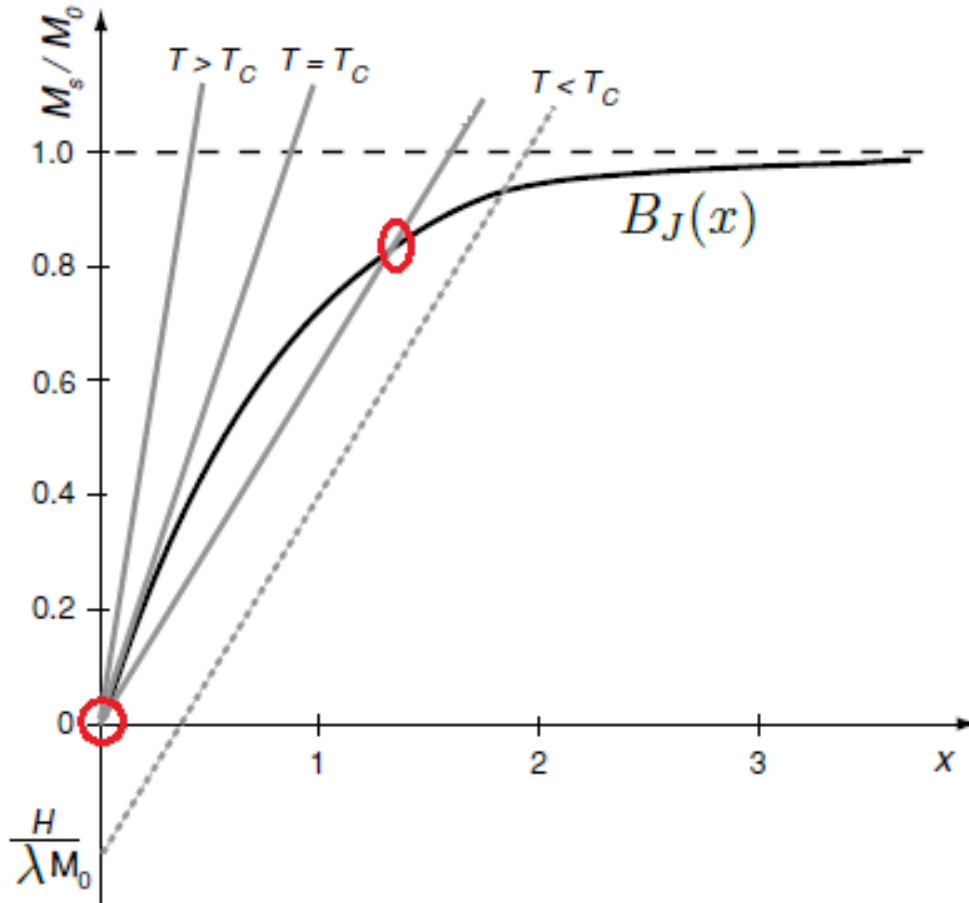
Figure 2.5: A graphical solution of Equations (2.4.4) and (2.4.6) [26].

$H \neq 0$, which demonstrate the offset created by the externally applied field. At and around the origin, the slope of Equation (2.4.6) for the graph $T = T_C$ equals that of $B_J(x) \approx (J+1)/3J$ for small x. Equating the two slopes gives a relationship between the Curie constant and Curie point temperature as $T_C = \lambda C$. At temperatures above T_C when a ferromagnet has become paramagnetic, the susceptibility is given

15

by the Curie-Weiss law in Equation (2.3.10) with $\theta_p = T_C$. This is in line with the experimental observations as temperature decreases to just above T_C where the susceptibility varies as $\chi = (T - T_C)^{-\gamma}$. The magnetization as the temperature increases to just below T_C varies as $M_s = (T_C - T)^\beta$. In the mean field theory $\gamma = 1$ and $\beta = \frac{1}{2}$ [26].

2.4.2 Antiferromagnetism

Antiferromagnetism occurs in structures that have at least two sublattices that are oppositely aligned. The sublattices align themselves such that the resultant magnetization is zero. The exchange integral $\mathcal{J}$ for this type of magnetism is negative. Figure 2.6 shows the arrangement of magnetic moments in an antiferromagnet [29]. The theory of antiferromagnetism was discussed by Louis Néel (in 1936) who introduced the magnetic phase transition temperature called the Néel point T_N. Above T_N an antiferromagnet becomes paramagnetic. The molecular field theory of anti-
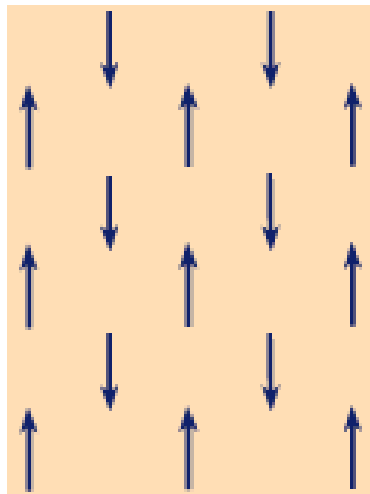
Figure 2.6: An ordered arrangement of oppositely aligned magnetic moments in an antiferromagnet [29].

ferromagetism considers two sublattices called A and B. The molecular fields $\boldsymbol{H}_A^i$ and $\boldsymbol{H}_B^i$ acting on sublattices A and B with magnetizations M_A and M_B respectively are given by

$$\boldsymbol{H}_A^i = \lambda_{AA}\boldsymbol{M}_A + \lambda_{AB}\boldsymbol{M}_B + \boldsymbol{H} \tag{2.4.7}$$

and

$$\boldsymbol{H}_B^i = \lambda_{BA}\boldsymbol{M}_A + \lambda_{BB}\boldsymbol{M}_B + \boldsymbol{H} \qquad (2.4.8)$$

where $\lambda_{AB} = \lambda_{BA}$ is the intersublattice coupling, $\lambda_{AA} = \lambda_{BB}$ is the intrasublattice coupling and $\boldsymbol{M}_A = -\boldsymbol{M}_B$ [26]. At T_N, M_A and M_B become zero and the spontaneous magnetization M_α ($\alpha = A, B$) of each sublattice is given in terms of the Brillouin function by

$$M_\alpha = M_{\alpha 0}B_J(x_\alpha) \qquad (2.4.9)$$

where $x_\alpha = \mu_0\mu|H_\alpha^i|/(k_B T)$. Above the Néel point T_N an antiferromagnet becomes paramagnetic and the susceptibility of a sublattice is given by

$$\chi = \frac{M_\alpha}{H_\alpha^i} = \frac{C'}{T} \qquad (2.4.10)$$

where $C' = \mu_0(n/2)g^2\mu_B^2 J(J+1)/(3k_B)$. Therefore M_A and M_B are given by

$$\boldsymbol{M}_A = (C'/T)(\lambda_{AA}\boldsymbol{M}_A + \lambda_{AB}\boldsymbol{M}_B + \boldsymbol{H}) \qquad (2.4.11)$$

and

$$\boldsymbol{M}_B = (C'/T)(\lambda_{BA}\boldsymbol{M}_A + \lambda_{BB}\boldsymbol{M}_B + \boldsymbol{H}). \qquad (2.4.12)$$

To ensure a non-zero solution in the absence of the applied field the coefficients of M_A and M_B are set to zero which leads to the determination of the Néel point temperature as

$$T_N = C'(\lambda_{AA} - \lambda_{AB}). \qquad (2.4.13)$$

It can be shown that the paramagnetic susceptibility above T_N is given by the Curie-Weiss law

$$\chi = \frac{2C'}{T - \theta_p} \qquad (2.4.14)$$

where $\theta_p = C'(\lambda_{AA} + \lambda_{AB})$. Hence T_N can be related to θ_p by

$$T_N = \frac{\lambda_{AA} - \lambda_{AB}}{\lambda_{AA} + \lambda_{AB}}\theta_p. \qquad (2.4.15)$$

The magnetic response of an antiferromagnet below T_N is dependent on the direction of the applied field $\boldsymbol{H}$ with respect to the axis of the A and B sublattices. The antiferromagnetic susceptibility can be determined in terms of parallel and perpendicular components. Figure 2.7 shows the antiferromagnetic susceptibility as a

17
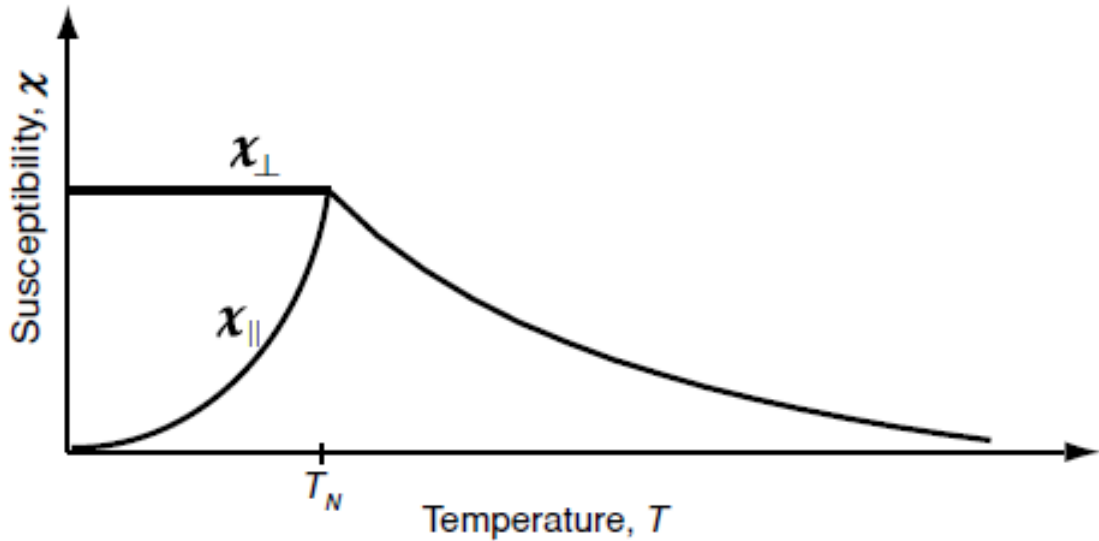
Figure 2.7: Antiferromagnetic susceptibility against temperature [26].

function of temperature. Above T_N, χ follows the paramagnetic Curie-Weiss law and below T_N, χ has the parallel $\chi_\parallel$ and perpendicular $\chi_\perp$ components. For powdered samples it can be shown that below T_N the average susceptibility is given by [26]

$$\chi = \frac{1}{3}\chi_\parallel + \frac{2}{3}\chi_\perp. \tag{2.4.16}$$

2.4.3 Ferrimagnetism

Ferrimagnetism is like both antiferromagnetism and ferromagnetism. It is described by both negative and positive interactions $\mathcal{J}$. However, a ferrimagnet has unequal sublattices A and B with different magnetizations M_A and M_B respectively. This is characterised by the antiparallel alignment of unequal moments as shown in Figure 2.8 [29]. The term ferrimagnet originates from the "ferrite-type ferromagnet". This is the type of magnetic order that is found in ferrite materials of the form $M\mathrm{Fe_2O_4}$, where M is a divalent element usually Zn, Fe, Ni, Co and so on. Ferrites have a spinel structure with the tetrahedral (A) and octahedral (B) crystallographic sites. Since the sublattices are not equal, the total magnetization $\boldsymbol{M} = \boldsymbol{M_A} + \boldsymbol{M_B} \neq \boldsymbol{0}$. The molecular field theory gives the same internal field equations as in Equations
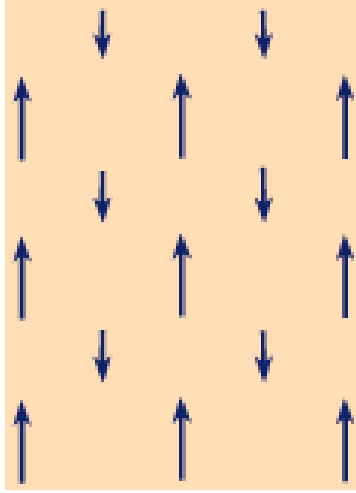
Figure 2.8: Antiparallel alignment of unequal magnetic moments in a ferrimagnet [29].

(2.4.7) and (2.4.8) with $M_A \neq M_B$ and $\lambda_{AA} \neq \lambda_{BB}$

$$\boldsymbol{H}_A^i = \lambda_{AA}\boldsymbol{M}_A + \lambda_{AB}\boldsymbol{M}_B + \boldsymbol{H} \tag{2.4.17}$$

and

$$\boldsymbol{H}_B^i = \lambda_{BA}\boldsymbol{M}_A + \lambda_{BB}\boldsymbol{M}_B + \boldsymbol{H}. \tag{2.4.18}$$

Proceeding as in the antiferromagnetism subsection, the magnetization of the sublattices is represented by the Brillouin function with $x_\alpha = \mu_0\mu H_\alpha^i/(k_B T)$ where $\alpha = A, B$. Figure 2.9 shows a graphical representation of the net magnetization which results from the magnetizations of the sublattices A and B [26]. In some cases a ferrimagnet might behave like an antiferromagnet and have $M_A = -M_B$. This is the case at a temperature known as the compensation temperature T_{comp}. The magnetizations become zero at the Curie temperature T_C.

Above the critical temperature, M_A and M_B are given by

$$\boldsymbol{M}_A = (C/T)(\lambda_{AA}\boldsymbol{M}_A + \lambda_{AB}\boldsymbol{M}_B + \boldsymbol{H}) \tag{2.4.19}$$

and

$$\boldsymbol{M}_B = (C/T)(\lambda_{BA}\boldsymbol{M}_A + \lambda_{BB}\boldsymbol{M}_B + \boldsymbol{H}). \tag{2.4.20}$$

where $C_\alpha = \mu_0 n_\alpha g^2 \mu_B^2 J(J+1)/(3k_B)$. Solving these equations in the absence of an
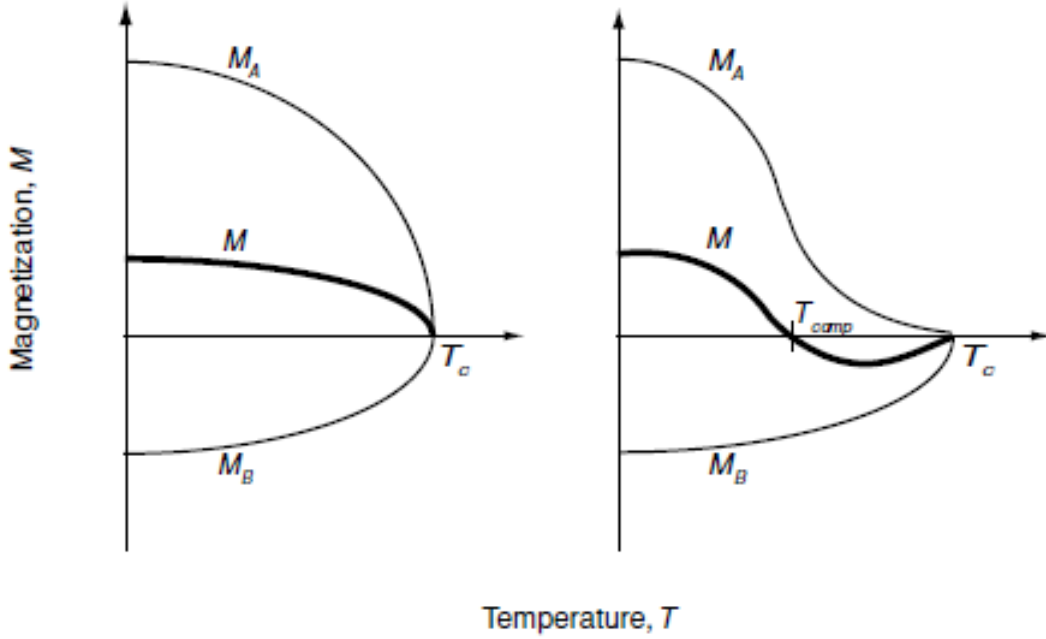
Figure 2.9: The magnetizations of the sublattices A and B with their net magnetization in a ferrimagnet [26].

applied field gives the critical temperature T_C as

$$T_C = \frac{1}{2}\left((C_A + C_B) + \sqrt{(C_A\lambda_{AA} - C_B\lambda_{BB})^2 + 4C_A C_B \lambda_{AB}^2}\right). \qquad (2.4.21)$$

The inverse susceptibility is given by

$$\frac{1}{\chi} = \frac{T - \theta}{C_A + C_B} - \frac{C"}{T - \theta'} \qquad (2.4.22)$$

where $C"$, θ and θ' are constants of the material. The graphical representation of Equation (2.4.22) is shown in Figure 2.10 [26].

2.4.4 Superparamagnetism

Paramagnetism in ferromagnets and ferrimagnets at and above the Curie and Néel temperatures respectively has been discussed in the previous subsections. However, superparamagnetism is known to occur below the Curie or Néel point temperature in single domain ferromagnetic or ferrimagnetic nanoparticles. Nanoparticles that have their magnetization favouring a one direction alignment are said to have uniaxial anisotropy. These types of nanoparticles flip their magnetization due to thermal
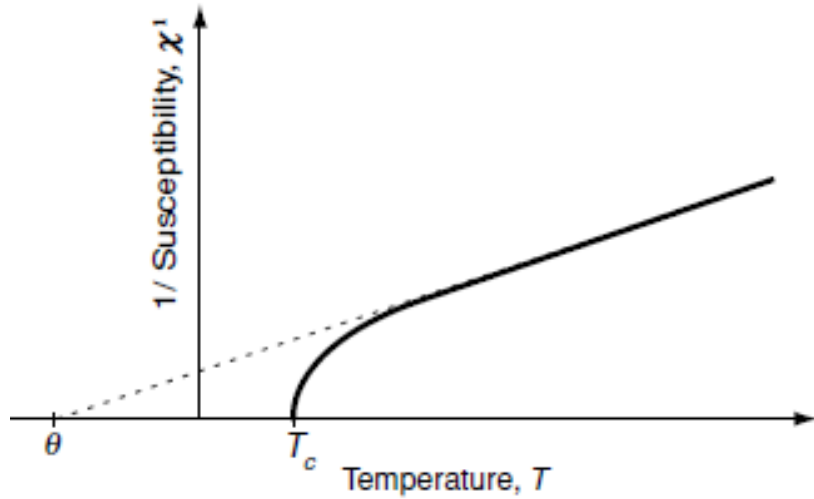
Figure 2.10: The inverse susceptibility in a ferrimagnet [26].

energy ($k_B T$) fluctuations. The average time τ between successive flips is given by the Néel relaxation time

$$\tau = \tau_0 \exp\left(\frac{\Delta E}{k_B T}\right) \tag{2.4.23}$$

where τ_0 is the time characteristic of the material [31]. ΔE is the energy barrier which has to be overcome by the thermal energy for a magnetization flip to occur and is given by

$$\Delta E = KV \sin^2 \theta \tag{2.4.24}$$

where K is the anisotropy constant, V is the volume of the nanoparticles and θ is the angle between the moments and the easy axis.

There are two magnetic states that may occur depending on the relative magnitudes of measurement time (τ_m) and τ in Equation (2.4.23). When $\tau \gg \tau_m$ the magnetization maintains one direction during measurement and therefore the magnetic moments are in an ordered state. This is known as a blocked state. The state of superparamagnetism occurs when $\tau \ll \tau_m$. In this case the magnetization keeps on fluctuating during the measurement and resulting in a zero net magnetization. When $\tau = \tau_m$ the transition between the blocked and superparamagnetic states occurs. The transition occurs at a temperature known as the blocking temperature

T_B which is given by

$$T_B = \frac{KV}{k_B \ln\left(\frac{\tau_m}{\tau_0}\right)}. \tag{2.4.25}$$

For the temperature region $T < T_B$ the nanoparticles are ferromagnetic or ferrimagnetic, for $T_B < T < T_C$ a superparamagnetic state occurs and for $T > T_C$ a paramagnetic state occurs. When an external field $\boldsymbol{H}$ is applied in the superparamagnetic region, the magnetic moments align themselves along $\boldsymbol{H}$ and therefore produce a nonzero magnetization. The superparamagnetic magnetization $\boldsymbol{M}$ is given by

$$\boldsymbol{M} = n\mu \tanh\left(\frac{\mu_0 \boldsymbol{H} \mu}{k_B T}\right) \tag{2.4.26}$$

where n is the nanoparticle density in a sample and μ is the magnetic moment of a single domain particle [31]. Experimental results have shown very little or no hysteresis loop for supeparamagnetic materials [32]. The superparamagnetic susceptibility is given by

$$\chi = \frac{n\mu_0 \mu}{k_B T} \tag{2.4.27}$$

which is related to Curie law.

2.5 Magnetization

The magnetization process heavily depends on the ferromagnet's domain structure and nucleation. The existence of domains results in the minimization of self energy of a ferromagnet. The process of magnetization is best described by the Stoner-Wohlfarth model. In this simplified model the ferromagnetic system is considered to have a single domain and therefore treated as a single spin. The ellipsoidal particle with a uniaxial anisotropy, shown in Figure 2.11, is assumed to be uniformly magnetized. The field $\boldsymbol{H}$ is applied at an angle α to the uniaxial anisotropy easy axis and the sample magnetization is rotated by angle θ. The energy density of the system is given by

$$E = K \sin^2\theta - \mu_0 MH \cos(\alpha - \theta) \tag{2.5.1}$$

where K is the magnetic uniaxial anisotropy constant [26]. Hysteresis occurs when Equation (2.5.1) has two minima with respect to θ. Hysteresis is a result of energy
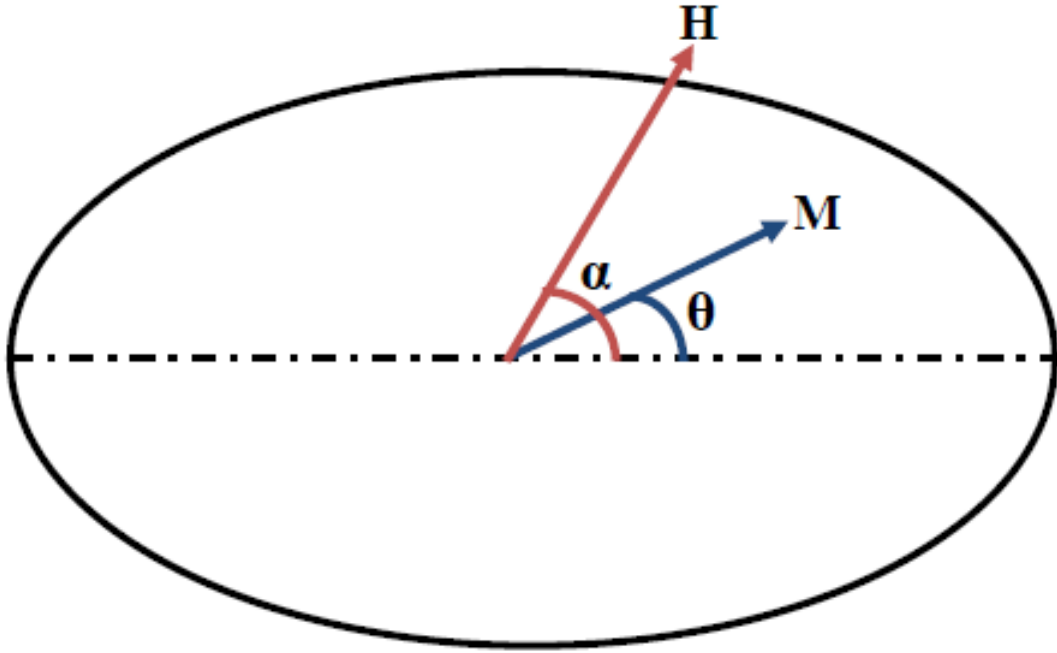
Figure 2.11: The magnetization of an ellipsoidal particle in an applied field.

loss in a ferromagnet and hence the area under the hysteresis curve represents the energy loss. Figure 2.12 shows a schematic representation of a M-H hysteresis loop [33]. The loop begins at zero with the initial or virgin curve upon the application of $\boldsymbol{H}$. The magnetization in the initial curve is given by

$$M = \chi_i H + \nu H^2 \qquad (2.5.2)$$

where χ_i is the reversible initial susceptibility and ν is the irreversible response to H. As the applied field increases, the initial curve increases to saturation magnetization M_s where the domains have their magnetizations pointing in the same direction. The saturation magnetization is usually expressed by the empirical relation

$$M = M_s \left(1 - \frac{a}{H} - \frac{b}{H^2} - \ldots \right) + \chi_0 H \qquad (2.5.3)$$

where a is a parameter due to defects, b is due to the reorientation of the magnetization and χ_0 is the high-field susceptibility [26]. At the zero field after magnetizing the material, the remanence magnetization M_R is still present. To get the magnetization back to zero requires a coercive force (coercivity) H_c. The bigger the coercive force, the harder the magnet and the greater the energy loss per cycle. Soft magnets have smaller H_c values.

23
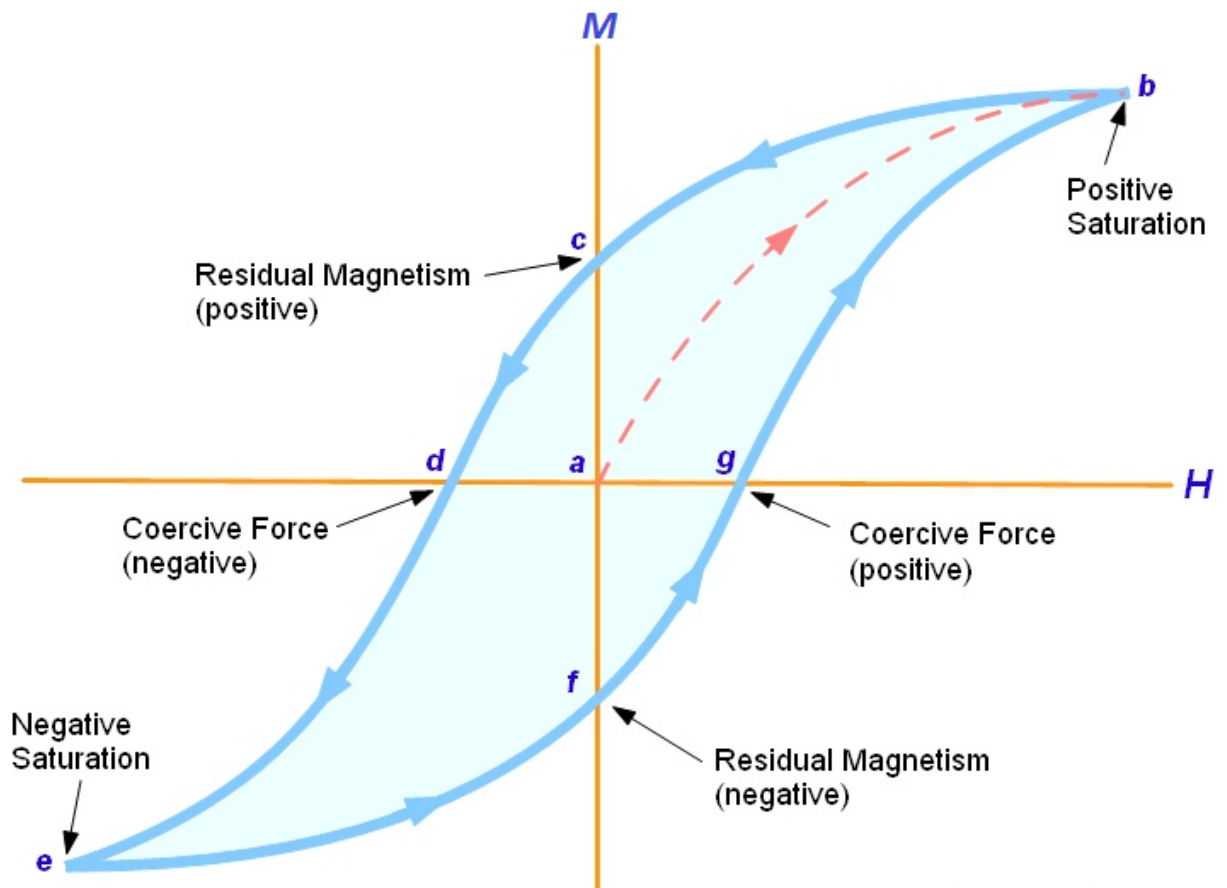
Figure 2.12: The magnetic hysteresis loop [33].

Chapter 3

Experimental techniques

3.1 Introduction

Nanoparticles are materials with particle sizes in the range 1 - 100 nm. Materials with particle sizes that are greater than 100 nm are referred to as bulk particles. Different behaviour between bulk and nanoparticles of the similar materials has been observed [34]. The interesting magnetic and electrical properties of the nanoparticles have attracted a lot of scientific research to the field of nanotechnology. This has led to the different ways in which the particle sizes can be controlled in order to stimulate the desired properties [1, 9, 24]. This size manipulation ranges from preparation techniques, sintering temperatures, starting materials that are used and so on. In this chapter we discuss the experimental techniques that were used in the current work which include the sample preparation technique that produces single phase nanoparticles at a relatively low temperature of 200 ℃. The equipment used and experimental approaches in testing the structural, magnetic and electrical properties are also discussed.

3.2 Glycol-thermal technique

The glycol-thermal technique is a low temperature synthesis technique in which the reaction is carried out at a temperature of 200 ℃. Single phase nanoparticles are produced directly without the need for any further heat treatment [17]. Chlorides

or nitrates which are used as the starting materials (reactants) and a base are used to precipitate the mixture. Chloride ions can be removed by rinsing with deionized water and filtering or by sedimentation using a centrifuge [2]. Ethylene glycol is used as a medium for the reaction in a heated and stirred pressure reactor.

In the current study we synthesized $Ni_xCo_{1-x}Fe_2O_4$ ($x = 0.0$ to 1.0 in steps of 0.1) and $Co(RE)_{0.1}Fe_{1.9}O_4$ (RE = Ce, Nd, Sm, Gd, Dy, Er and Yb) nanoferrites using the glycol-thermal technique. Stoichiometric amounts of starting materials of $Ni(NO_3)_2.6H_2O$ (purity of 99.999%), $Co(NO_3)_2.6H_2O$ (purity of 99.999%) and $FeCl_3.6H_2O$ (purity > 98%) were used to produce the $Ni_xCo_{1-x}Fe_2O_4$ series. $Co(RE)_{0.1}Fe_{1.9}O_4$ samples were produced from the stoichiometric amounts of $CoCl_2.6H_2O$ (purity > 98%), $FeCl_3.6H_2O$ (purity > 98%) and rare-earth (RE) chloride salts (purity of 99.999%). The electronic balance, Precisa 205 A SCS, was used to weigh the predetermined amounts of the reactants.

The reactants were mixed together in deionized water and the mixture was stirred with a magnetic stirrer for about 20 minutes [17]. While stirring, NaOH was carefully added until a pH of 9 was achieved. The precipitate that formed was transferred into a Büchner funnel, lined with a Whatman glass microfiber filter (GF/F), to be washed with deionized water and filtered under suction until all the chloride ions were removed. This was tested by adding a few drops of a standard solution of silver nitrate to the filtered water contents. A clear solution confirmed the removal of all chloride ions. The chloride-free precipitate was then dispersed in about 250 ml of ethylene glycol using a magnetic stirrer.

The wet precursor was then transferred into a glass lining of a stainless steel stirred pressure reactor vessel of a watlow series model PARR 4843 reactor [17]. This pressure reactor is shown in Figure 3.1. The reaction process involved raising the temperature for one hour from room temperature to 200 °C which is close to the boiling point (197.3 °C) of ethylene glycol [9]. This temperature was maintained for the next six hours before finally cooling down the reaction for another one hour. Figure 3.2 shows the operation schedule for the stirred pressure reactor. On reaction completion, the product was filtered over another Whatman glass microfiber filter and rinsed with deionized water and then finally with ethanol. The product was left

Figure 3.1: The stirred pressure reactor, watlow series model PARR 4843.

to dry under suction and an infrared lamp. The dry product was finally homogenized using an argate mortar and pestle.
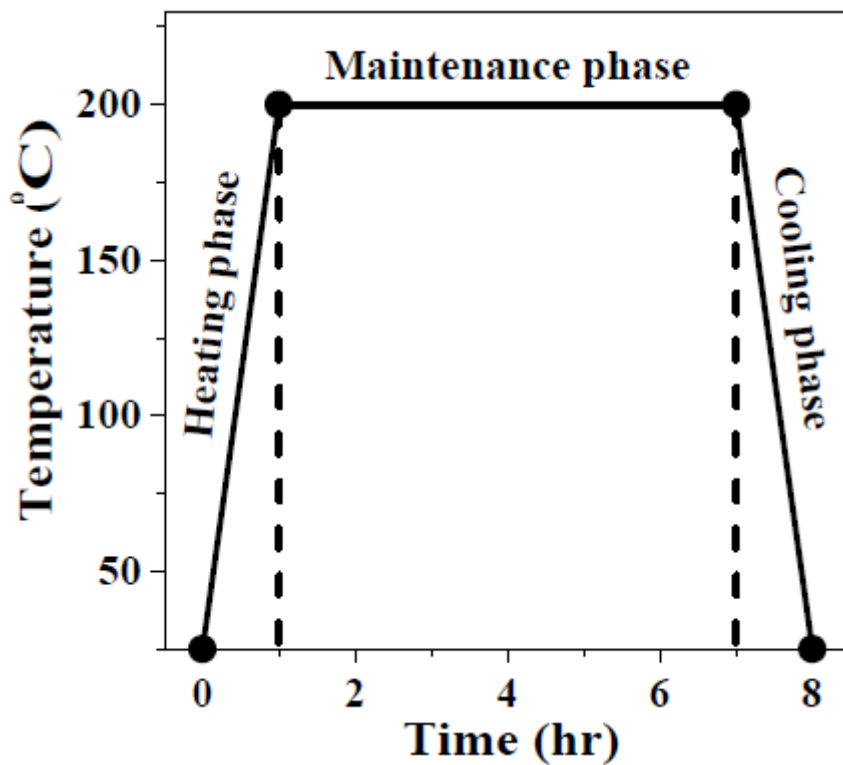
Figure 3.2: The operation schedule of the stirred pressure reactor, model PARR 4843.

3.3 X-ray diffraction

X-ray diffraction (XRD) is a technique used to characterize crystalline materials. It is based on the scattering of X-rays from the atoms of a crystalline material. This forms a diffraction pattern which can be used as a fingerprint for that material [35]. Bragg's law provides the conditions for XRD to occur. This law is given by

$$n\lambda = 2d \sin \theta \tag{3.3.1}$$

where n is the integer representing the diffraction order, λ is the incident ray wavelength, d is the distance between the lattice planes (d-spacing) and θ is the angle

between the incident ray and a lattice plane. Figure 3.3 shows the graphical representation of Bragg scattering [36]. In the current work the PANalytic EMPYREAN,
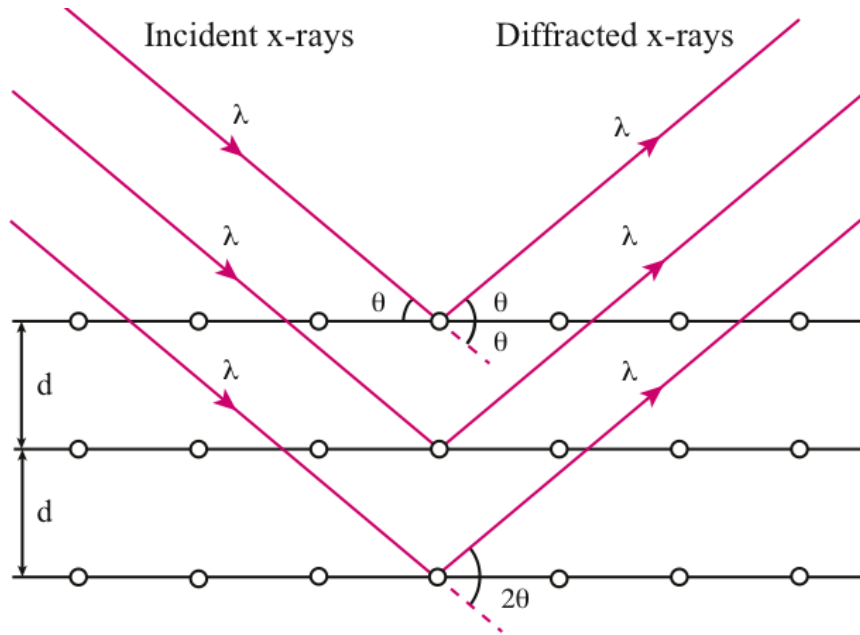
Figure 3.3: The graphical representation of Bragg scattering [36].

shown in Figure 3.4, was used for the XRD measurements on the powder samples. The XRD pattern is generated from these measurements. The XRD pattern is a graphical representation of absolute intensity versus diffraction angle 2θ or relative intensity versus d-spacing [35]. Useful information can be derived from an XRD pattern. For a cubic crystalline material, the lattice parameter a is equal to the dimensions of a unit cell and is given by

$$a = d\sqrt{h^2 + k^2 + l^2} \qquad (3.3.2)$$

where h, k and l are the Miller indices for the lattice planes. Although the PANalytic EMPYREAN gives a value for d together with the XRD pattern, this may easily be eliminated by combining Equations (3.3.1) and (3.3.2) to give the lattice parameter a as

$$a = \frac{n\lambda\sqrt{h^2 + k^2 + l^2}}{2\sin\theta}. \qquad (3.3.3)$$

Figure 3.4: The PANalytic EMPYREAN for XRD measurements.

The crystallite (particle) size D can also be determined from the XRD pattern using the Scherrer formula

$$D = \frac{K\lambda}{\beta \cos \theta} \qquad (3.3.4)$$

where K is the shape factor (≈ 0.9 for a cubic spinel structure) and β is the full width at half maximum of the most intense XRD peak (311 for a spinel structure) [37]. The lattice strain ϵ can also be determined from XRD which is given by

$$\epsilon = \frac{\beta}{4 \tan \theta} \qquad (3.3.5)$$

where the variables are defined as before [37]. XRD density ρ_{XRD} refers to the atomic packing of a unit cell and is given by

$$\rho_{XRD} = \frac{8M_o}{N_A a^3} \qquad (3.3.6)$$

where M_o is the molar weight and N_A is the Avogadro's number [17]. If the bulk density ρ_{Bulk} ($= \frac{Mass}{Volume}$) is known, then the porosity P of the material can be determined [17]. The porosity is defined as the measure of the "empty" space within the crystalline material, defined as

$$P = 1 - \frac{\rho_{Bulk}}{\rho_{XRD}}. \qquad (3.3.7)$$

3.4 Mössbauer spectroscopy

The Mössbauer spectroscopy is a technique that can be used to study nuclear interactions in atoms. This gives information about the structural, chemical and magnetic characteristics of the material. The technique has been widely used in the physical and chemical sciences since the 1960s. The Mössbauer spectroscopy is based on the Mössbauer effect discovered by Rudolf L Mössbauer in 1957. He discovered non-recoiling emission and absorption of nuclear gamma rays while working on his PhD thesis in Heidelberg [38]. This effect and the spectroscopy technique have since been named after him.

3.4.1 The Mössbauer effect

The Mössbauer effect is the recoil-free emission and absorption of a γ-ray by a nucleus without thermal broadening [39]. Identical nuclei have equal transition energy between the excited and ground states [38]. Figure 3.5 shows a graphical representation of the γ-ray source and absorber which have isotopes that are in the same cubical environments leading to an unshifted Mössbauer spectrum about the zero velocity [40]. The transition energy E_T is given by

$$E_T = E_{es} - E_{gs} \qquad (3.4.1)$$

where E_{es} and E_{gs} are the energy levels of the excited and ground states nuclei respectively. For the Mössbauer effect to occur, the emitted γ-ray energy E_γ must
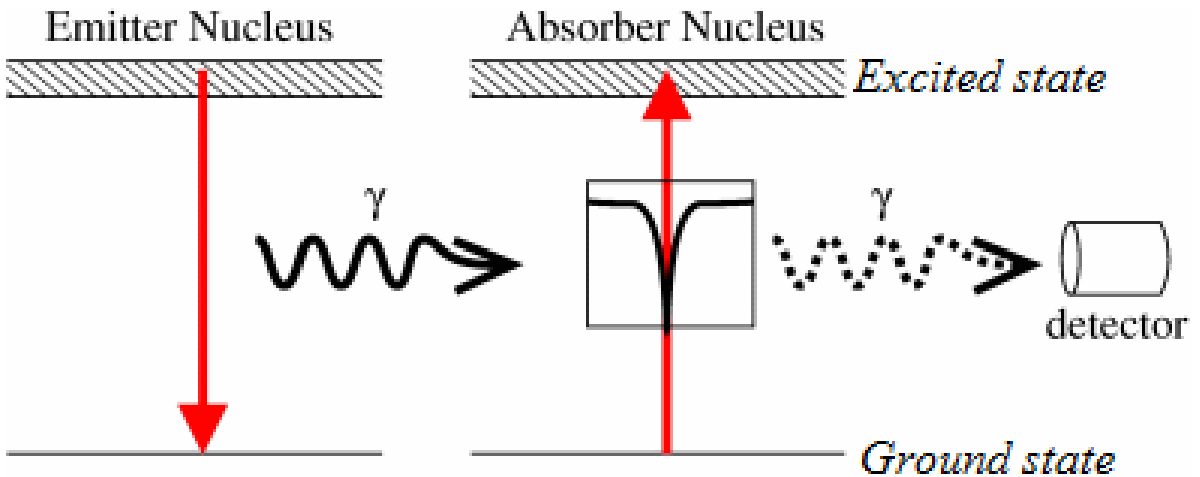
Figure 3.5: A gamma ray that is emitted by an excited nucleus is absorbed by an identical ground state necleus [40].

be equal to the nuclear transition energy E_T. The Equation

$$E_T = E_\gamma \qquad (3.4.2)$$

can only be satisfied if the emitting and absorbing nuclei do not recoil upon emission and absorption. This means that the energy distributions for emission and absorption have to overlap quite reasonably for resonance to occur [38]. Figure 3.6 shows the free emitter and absorber nuclei recoiling upon emission and absorption

of a γ-ray photon [41]. The recoiling is due to the principle of conservation of linear momentum. This is typical of gas and liquid materials and is the reason why the Mössbauer effect cannot be observed for materials in these phases [38]. The energy

Figure 3.6: The emission and absorption of a photon by a free atom resulting in recoil [41].

E_R associated with nuclear recoil upon emission and absorption of a γ-ray photon by a nucleus of mass M is given by

$$E_R = \frac{E_\gamma{}^2}{2Mc^2} \tag{3.4.3}$$

where c is the speed of light [38]. However, for solid materials where the atoms are fixed in a crystal lattice, the effect of recoil can effectively be almost zero. This is because in a solid molecule, the recoil energy is distributed through the whole crystal which means the mass M in Equation (3.4.3) is much bigger (i.e., for the whole crystal) and therefore leading to a much smaller E_R. The natural line width Γ corresponds to the uncertainty of the energy distribution of the emitted photons [42]. The Heisenberg uncertainty principle relates the mean lifetime τ of the excited state to the line width

$$\Gamma = \frac{\hbar}{\tau} \tag{3.4.4}$$

where $\hbar = \frac{h}{2\pi}$ with h being Planck's constant [38]. When E_R is greater than Γ, the energy distributions for the emitter and absorber do not overlap and therefore no resonance absorption takes place.

In the Mössbauer set-up used in the current work, ^{57}Co sealed in Rh matrix is used as a source of γ-rays. The source is vibrated at constant acceleration to create a Doppler shift in the emitted γ-ray energy. This compensates for the energy loss through recoil upon emission and absorption and hence leads to the resonance

absorption [42]. The γ-ray energy Doppler-shifts by an amount ΔE that is given by

$$\Delta E = \frac{v}{c} E_\gamma \qquad (3.4.5)$$

where v is the velocity at which the source moves and c is the speed of light. Figure 3.7 shows a decay representation of ^{57}Co to ^{57}Fe by electron capture (EC) [43]. The excited state of 136 keV, with a nuclear spin quantum number $I = \frac{5}{2}$ and a half-life of 10 ns, is the initial nuclear energy level of ^{57}Fe that is occupied. There are two decay routes from the 136 keV state. One is directly to the ground state where $I = \frac{1}{2}$ with a 15% probability. The other is to the 14.4 keV state, which has a halflife of about 100 ns and $I = \frac{3}{2}$, with a probability of 85%. Both the energy and half-life of the 14.4 keV state are suitable for the ^{57}Fe Mössbauer spectroscopy [38].

In the current work all the samples contain ^{57}Fe isotopes with a natural abundance of 2.12% [26]. The ^{57}Fe isotopes are the identical emitter and absorber nuclei. The Mössbauer spectra which represent the relative transmission of γ-rays against velocity were analysed using the Recoil software for Mössbauer analysis. To record a Mössbauer spectrum, the Mössbauer peak has to be selected for a particular source. A typical spectrum that is produced by the ^{57}Co source and recorded directly by a detector is shown in Figure 3.8. By indexing the dominant peaks with the known energy values of a ^{57}Co source and comparing the ratios of these energies to the measured voltage ratios of the peaks, the Mössbauer peak (14.4 keV peak) was determined and selected. This ensures that only the γ-rays with the energy of 14.4 keV are recorded by the detector.

After selecting the Mössbauer peak, the α-iron foil (containing 2.12% ^{57}Fe) was used as an absorber in order to deduce the velocity calibrations for a particular maximum velocity setting. The formation of a six-absorption-line spectrum indicates that a correct Mössbauer peak had been selected. About 0.1 g of a sample (absorber) was then spread evenly across the sample holder to be measured. Depending on the sample, the Doppler maximum velocity was adjusted such that the the spectrum fits across the velocity range and the calibration is obtained at that set velocity using the known values of α-iron foil. In the following section we discuss the relevant hyperfine interactions and parameters.
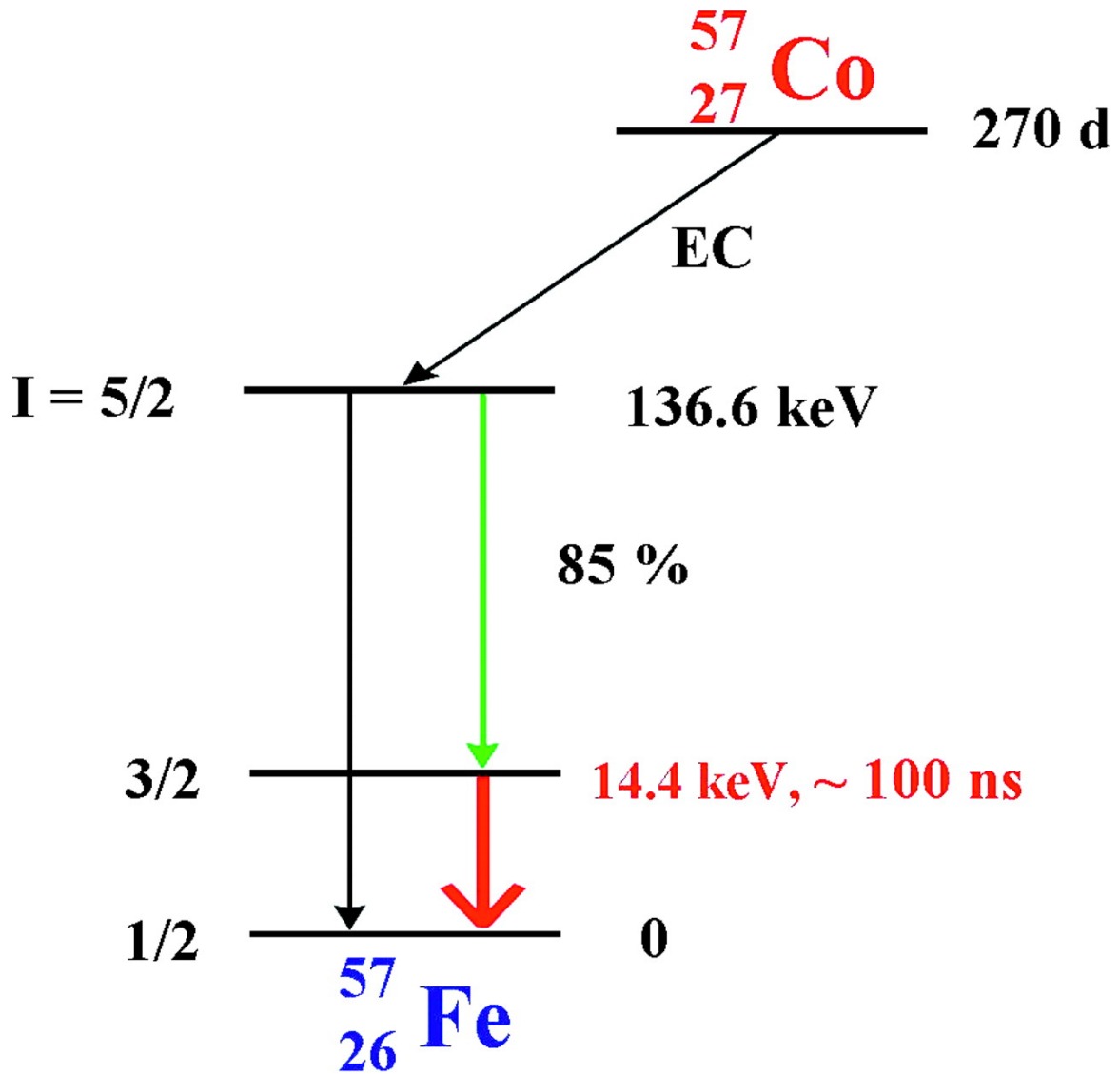
Figure 3.7: The decay representation of ^{57}Co to ^{57}Fe by electron capture [43].

3.4.2 Hyperfine interactions

The Mössbauer spectrum is characterized by the number, position, relative intensity and shape of the absorption lines [45]. These characteristics depend mainly on the types of interactions the nuclei experience in their surrounding environments. Being positively charged, the nuclei may experience both electrical and magnetic interactions in their environments. These are called the hyperfine interactions. There are three kinds of hyperfine interactions of interest for the Mössbauer spectrum. The
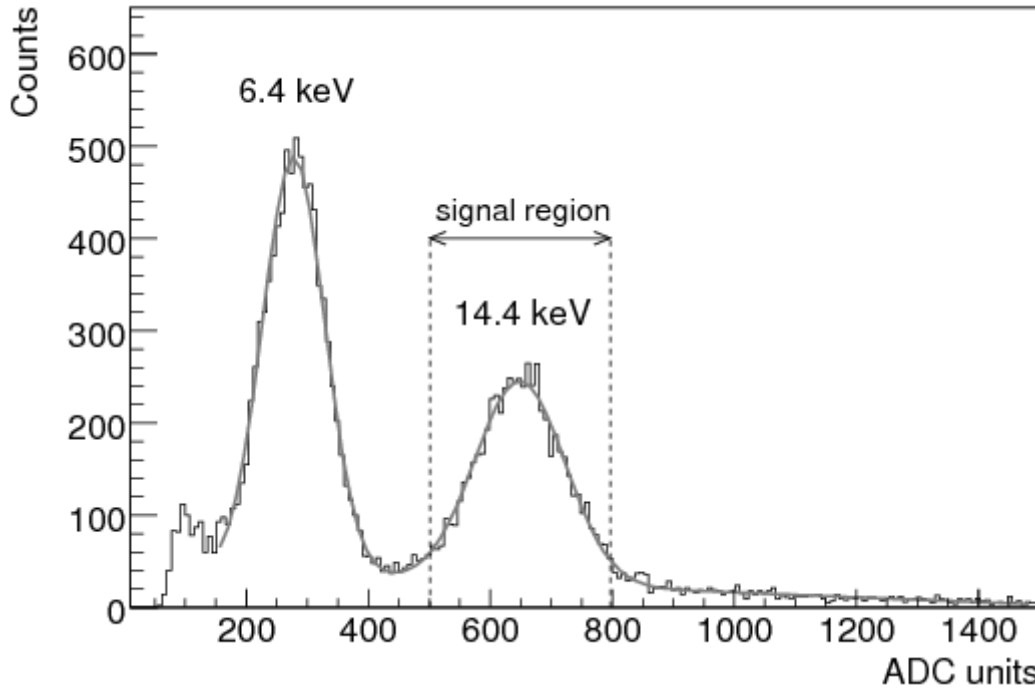
Figure 3.8: A typical ^{57}Co source spectrum where the Mössbauer peak is selected [44].

governing Hamiltonian $\mathcal{H}$ for these interactions is given by

$$\mathcal{H} = \mathcal{H}(e0) + \mathcal{H}(m1) + \mathcal{H}(e2) \tag{3.4.6}$$

where $\mathcal{H}(e0)$ refers to the Coulombic interactions between the nucleus and its surrounding electrons, $\mathcal{H}(m1)$ refers to the coupling between the nuclear magnetic dipole moment and the magnetic field at the nucleus and $\mathcal{H}(e2)$ refers to the electric quadrupole interactions [46]. The measurable Mössbauer parameters which are the chemical isomer shift δ, electric quadrupole splitting Δ and the magnetic hyperfine splitting H give information about $\mathcal{H}(e0)$, $\mathcal{H}(e2)$ and $\mathcal{H}(m1)$ respectively. Figure 3.9 shows a graphical representation of the observable parameters of a Mössbauer spectrum. The figure also shows the relationship between the energy levels and the absorption lines of a spectrum. The Mössbauer parameters are briefly discussed in turn in the following subsections.
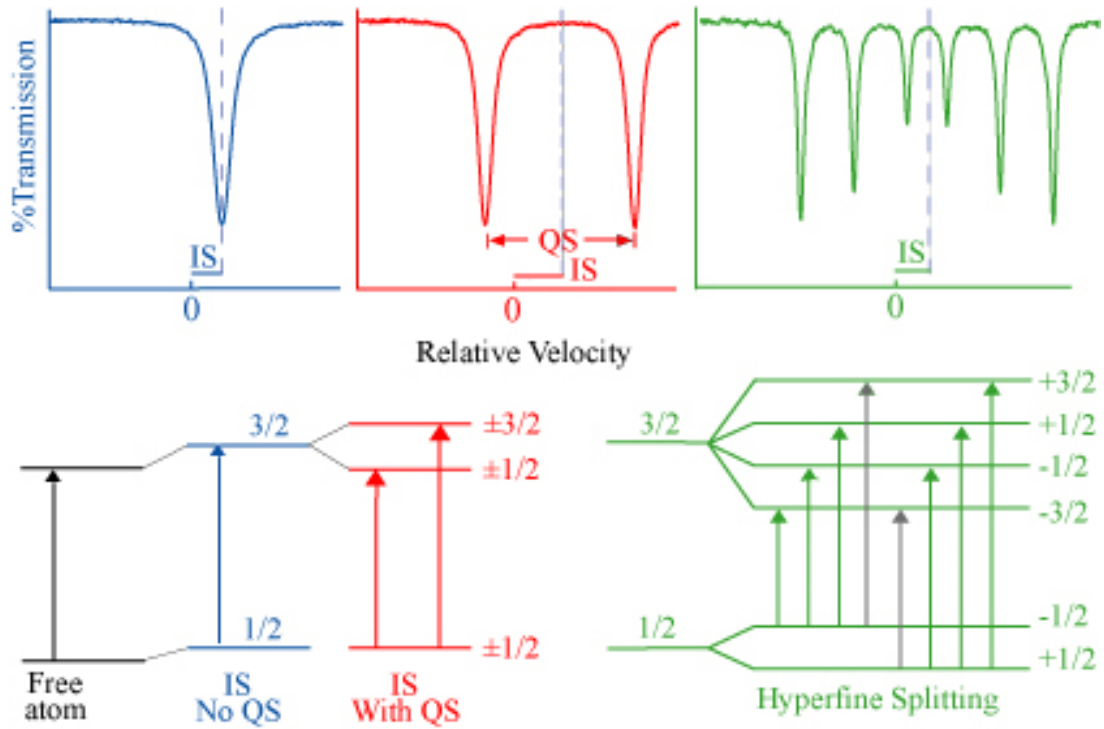
Figure 3.9: A graphical representation of the observable Mössbauer variables due to the hyperfine interactions. The effect of the isomer shift (IS), quadrupole splitting (QS) and hyperfine splitting of the energy levels on the Mössbauer spectrum [47].

3.4.2.1 Chemical isomer shift

The chemical isomer shift is due to the Coulombic interactions between the nuclear protons and the s-electrons that penetrate the nuclear environment [46]. The nuclear radii of the ground R_g and excited R_e states are not equal. When the source and the absorber are chemically different then the s-electron densities in the source ρ_S and absorber ρ_A nuclei are different. This means that the electrostatic interactions are different for the excited and ground states and hence the energy levels of the source and the absorber shift by different amounts. This gives rise to the isomer shift δ given by

$$\delta = \frac{2}{3}\pi Z e^2 (\rho_A - \rho_S)(R_e{}^2 - R_g{}^2) \tag{3.4.7}$$

where Z is the atomic number and e is the electronic charge [38]. The isomer shift, as seen in Figure 3.9, is a shift from the zero velocity line of the Mössbauer spectrum. It is influenced by the s-orbital electrons directly and also by the p-, d- and f-orbital

electrons indirectly by shielding the s-electrons [46]. The information about the valency and oxidation state of the Mössbauer atom can be deduced from the isomer shift.

3.4.2.2 Quadrupole splitting

Electric quadrupole interaction occurs when at least one of the nuclear states possesses a quadrupole moment eQ. This is a measure of spherical distortion of the nucleus with $-Q$ and $+Q$ indicating a flattened and elongated nucleus respectively. Nuclear states with spin $I \leqslant \frac{1}{2}$ do not possess a quadrupole moment. However, states of spin $I > \frac{1}{2}$ do possess a quadrupole moment ($Q \neq 0$) and can therefore interact with the non-homogeneous electric field represented by the electric field gradient (EFG) [46]. The energy of the substates $E_Q(I, m_I)$ are the eigenvalues of the Hamiltonian that describe the quadrupole interactions expressed by

$$E_Q(I, m_I) = \frac{eQV_{zz}}{4I(2I-1)}[3m_I^2 - I(I+1)](1 + \frac{\eta^2}{3})^{\frac{1}{2}} \qquad (3.4.8)$$

where $m_I = I, I-1, ..., -I$ is the nuclear magnetic spin quantum number, V_{zz} is the tensor component of the EFG and η is the asymmetry parameter with respect to the principal axis of the EFG [46]. The selection rules for the γ-ray transitions are $\Delta I = \pm 1$ and $\Delta m_I = 0, \pm 1$ [39]. For ^{57}Fe the ground state with $I = \frac{1}{2}$ forms substates $m_I = \pm\frac{1}{2}$ that do not split. These substates are said to be two-fold degenerate. This degeneracy is due to the fact that by Equation (3.4.8) both $m_I = \frac{1}{2}, -\frac{1}{2}$ result in equal E_Q values. The excited state with $I = \frac{3}{2}$ splits into two states, $m_I = \pm\frac{1}{2}, \pm\frac{3}{2}$, that are two-fold degenerate as can be seen on Figure 3.9. For axially symmetric EFG ($\eta = 0$), the energy difference ΔE_Q between the two substates is given by

$$\Delta E_Q = \frac{eQV_{zz}}{2} \qquad (3.4.9)$$

$\Delta E_Q = \Delta$ is the quadrupole splitting which is the observable Mössbauer parameter. On the Mössbauer spectrum (Figure 3.9) this is the separation between the two absorption lines (each absorption line for each of the two substates). Quadrupole splitting results into the formation of a doublet on the spectrum. The degeneracy of the substates can be lifted by a magnetic field.

3.4.2.3 Magnetic hyperfine splitting

Magnetic hyperfine interaction occurs when a nucleus possesses a magnetic dipole moment $\boldsymbol{\mu}$. A nucleus must have a nuclear spin $I > 0$ to possess $\boldsymbol{\mu}$ which then interacts with the magnetic field $\boldsymbol{H}$ at the nucleus [46]. The eigenvalues $E_M(m_I)$ of the Hamiltonian that governs the magnetic hyperfine interaction are given by

$$E_M(m_I) = -\frac{\mu H m_I}{I} = -g_N \beta_N H m_I \qquad (3.4.10)$$

where g_N is the nuclear Landé splitting factor and $\beta_N = \frac{e\hbar}{2Mc}$ is the Bohr magneton [46] with a value of 5.04929×10^{-27} J.T^{-1} [39]. Both the excited ($I = \frac{3}{2}$) and ground ($I = \frac{1}{2}$) states of ^{57}Fe possess a magnetic dipole moment. Since $m_I = I, I-1, ..., -I$ and the state of spin I splits into $(2I+1)$ substates, the ground and excited states will split into two ($m_I = -\frac{1}{2}, +\frac{1}{2}$) and four ($m_I = +\frac{3}{2}, +\frac{1}{2}, -\frac{1}{2}, -\frac{3}{2}$) substates respectively. According to Equation (3.4.10) both these states form non-degenerate substates. Once again the allowable Mössbauer transitions are governed by the selection rules, $\Delta I = \pm 1$ and $\Delta m_I = 0, \pm 1$. The six energy transition lines and the corresponding sextet Mössbauer spectrum are shown in Figure 3.9. The difference in the order of negative and positive substates of the excited and ground states is attributed to the opposite signs of $\boldsymbol{\mu}$ for these substates [38]. It should be noted that the isomer shift is also present in both the electric quadrupole splitting and the magnetic hyperfine splitting.

3.4.3 Experimental set-up

The Mössbauer spectrometer system that was used for this work is shown in Figure 3.10. The system consists of measurement instruments, a cryostat and a sample rod that holds the sample. The sample chamber and cryostat (vacuum jacket) were connected to a vacuum pump and helium gas cylinder. The LakeShore 331 temperature controller was connected to the sample rod for temperature-controlled measurements. Liquid nitrogen was poured into the reservoir in the cryostat and helium gas was pumped into the sample chamber after sucking out the air for low temperature (as low as 80 K) measurements. On the operation side, the HALDER

MR-351 Mössbauer drive unit (MDU) drives the HALDER D 8110 transducer to oscillate at constant acceleration. A FAST ComTec pre-amplifier powers and collects the data from an LND 45431 detector. The signal is amplified by the CANBERRA 2011 linear amplifier and goes through a Single Channel Analyzer (SCA) and an ORTEC model MCSPCI card (Multi-Channel Analyzer, MCA) before being displayed on a computer. An oscilloscope, which monitors and displays the Doppler shift velocity/time (constant acceleration) graph, is connected to the MDU. The system is powered by the TUNNELEC TC 950 HV power supply. A concrete wall separates the operation and the measurement sides to minimise radiation exposure while operating the system. The Mössbauer furnace, which is not shown here, was used for the high temperature measurements. Figure 3.11 is a block diagram rep-
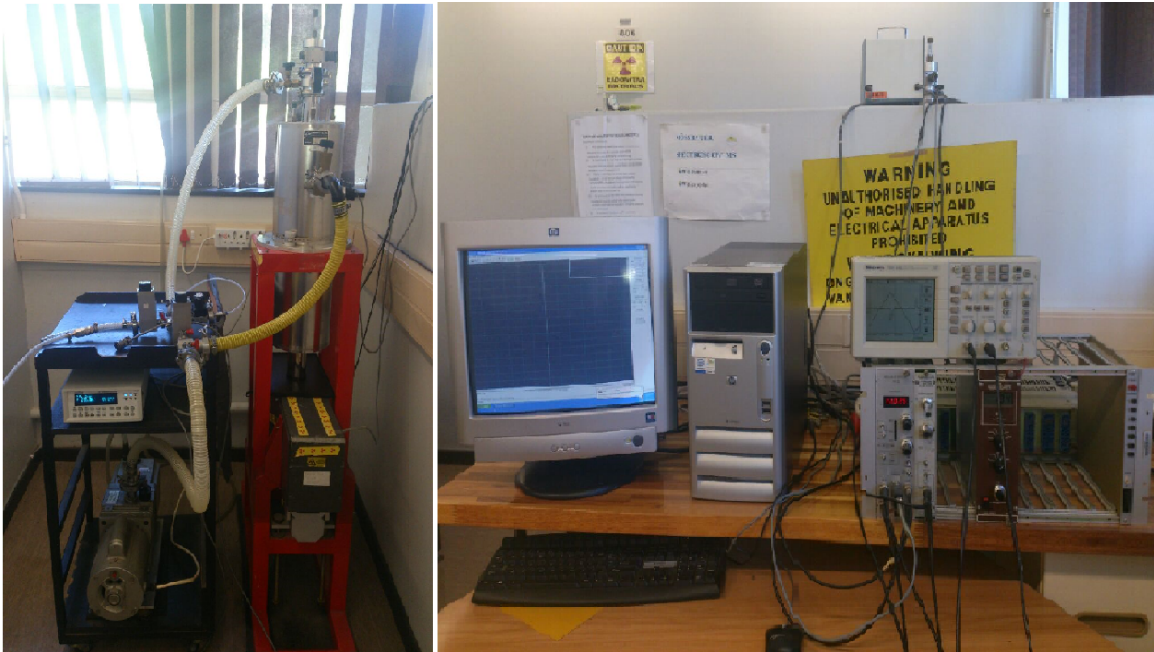
Figure 3.10: The Mössbauer spectrometer which includes a cryostat, temperature controller, pump, sample chamber, computer, Mössbauer unit and an oscilloscope.

resentation of the experimental set-up of the Mössbauer spectromer. It shows the connections of the components to each other and the flow of the signals.
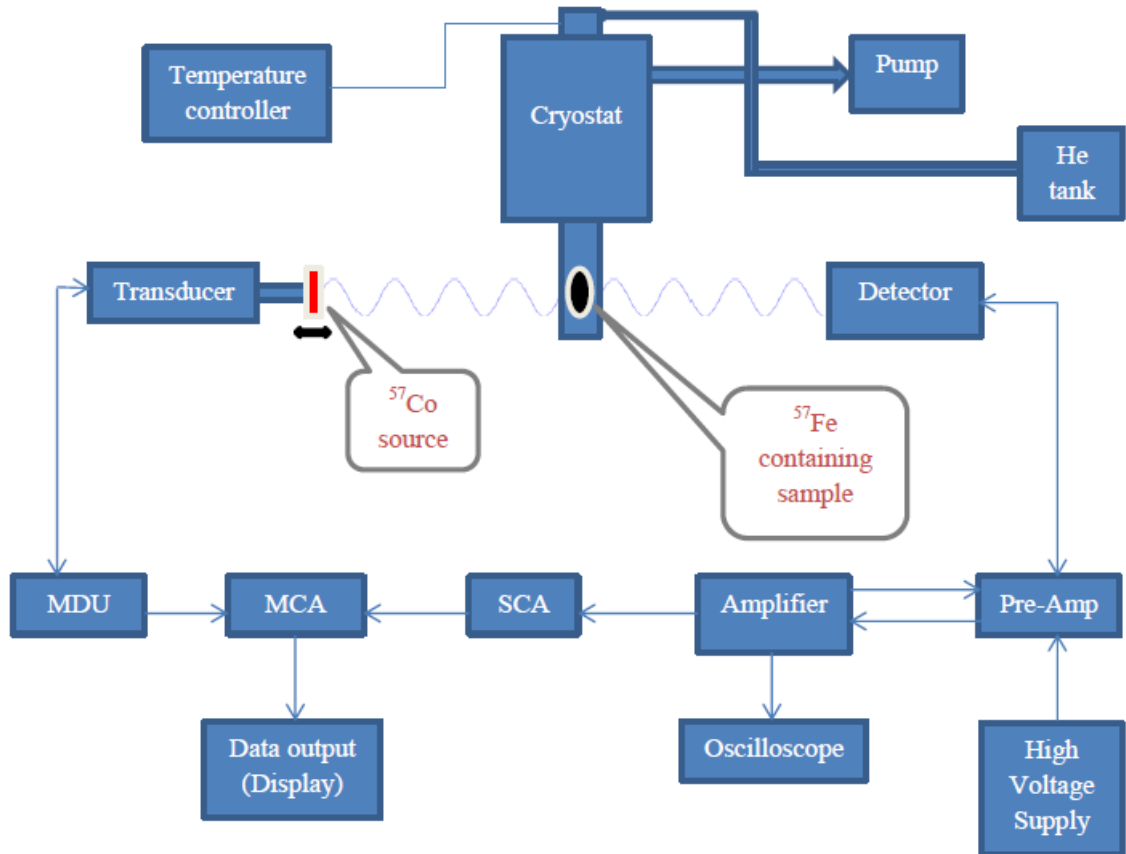
Figure 3.11: The block diagram representation of the Mössbauer spectrometer set-up.

3.5　Magnetization

The magnetization $\boldsymbol{M}$ of a material is defined as the magnetic dipole moment per unit area of the material [26]. Ferromagnetic materials may undergo spontaneous magnetization. The interesting phenomenon in ferromagnets is the response of the magnetization to the applied external field $\boldsymbol{H}$. This response is depicted by a hysteresis loop shown in Figure 2.12. The hysteresis loop shows the irreversible nature of the magnetization curve. We used a LakeShore model 735 vibrating sample magnetometer (VSM) to do the magnetization measurements for our samples. The VSM set-up is shown in Figure 3.12. A sample size of about 0.025 g was subjected to a magnetic field strength up to 15 kOe. The set-up consists of an electromagnet which creates the external magnetic field to which the sample is subjected. A NESLAB ThermoFlex 2500 chiller maintained a constant temperature of the electromagnet

Figure 3.12: The LakeShore Vibrating Sample Magnetometer (VSM) set-up.

by circulating cold water through the system. The electromagnet was powered by a LakeShore 642 bipolar electromagnet power supplier while a Gaussmeter model 450 was used for measuring the magnetic field strength. For temperature controlled measurements, a temperature controller model 340 may be used. The data were recorded via a National Instruments IEEE-488 interface card on a computer. Power to the VSM system is provided through an Eaton 9355 Uninterrupted Power Supply (UPS). Figure 3.13 shows a schematic representation of the VSM system.

3.6   Resistivity measurements

The semiconducting properties of the samples were studied through electrical resistivity measurements using the four-probe method. Figure 3.14 shows the experimental set-up for the electrical resistivity measurements against temperature.
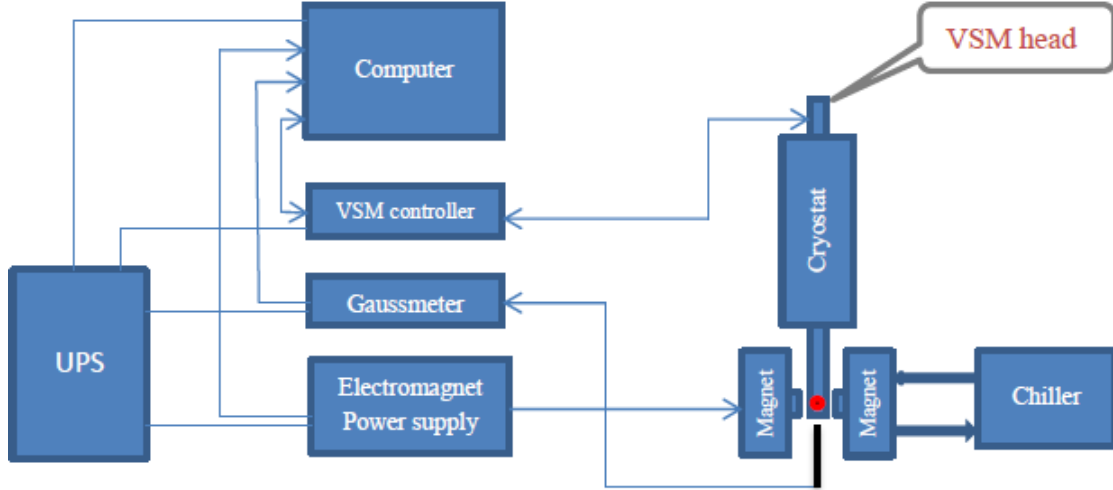
Figure 3.13: The schematic representation of the VSM set-up.

The set-up consists of the LCS-02 Low Current Source, DMV-001 Digital Micro-voltmeter, PID controlled oven model PID-200, oven and the four probe unit. The arrangement of the four probes and how they connect to the sample for measurement is shown in Figure 3.15 [48]. The two inner probes measure the voltage drop ΔV and the outer probes measure the current I. For the pellet samples the thickness h of the samples was always less than the distance a between the inner voltage probes. In this particular case the resistivity ρ is calculated using the formula

$$\rho = \frac{\pi}{\ln 2} h \frac{\Delta V}{I}. \tag{3.6.1}$$

In our measurements, the temperature was incremented by 5 °C in the region 25 °C to 130 °C. ΔV and I were measured at each point. The resistivity ρ at a temperature T for granular materials can be calculated as

$$\rho(T) = \rho_0 \exp[2(E_1/k_B T)^{1/2}] \tag{3.6.2}$$

where ρ_0 is the resistivity at 0 K, E_1 is the tunneling activation energy between the grains and k_B is the Boltzmann's constant [17]. Here the electrons and holes conduct by moving between the charged and neutral grains. In semiconductors the conducting electrons and holes move between the divalent and trivalent metal cations [17]. In this case the resistivity is determined by Arrhenius equation

$$\rho(T) = \rho_0 \exp(E_2/k_B T) \tag{3.6.3}$$

43
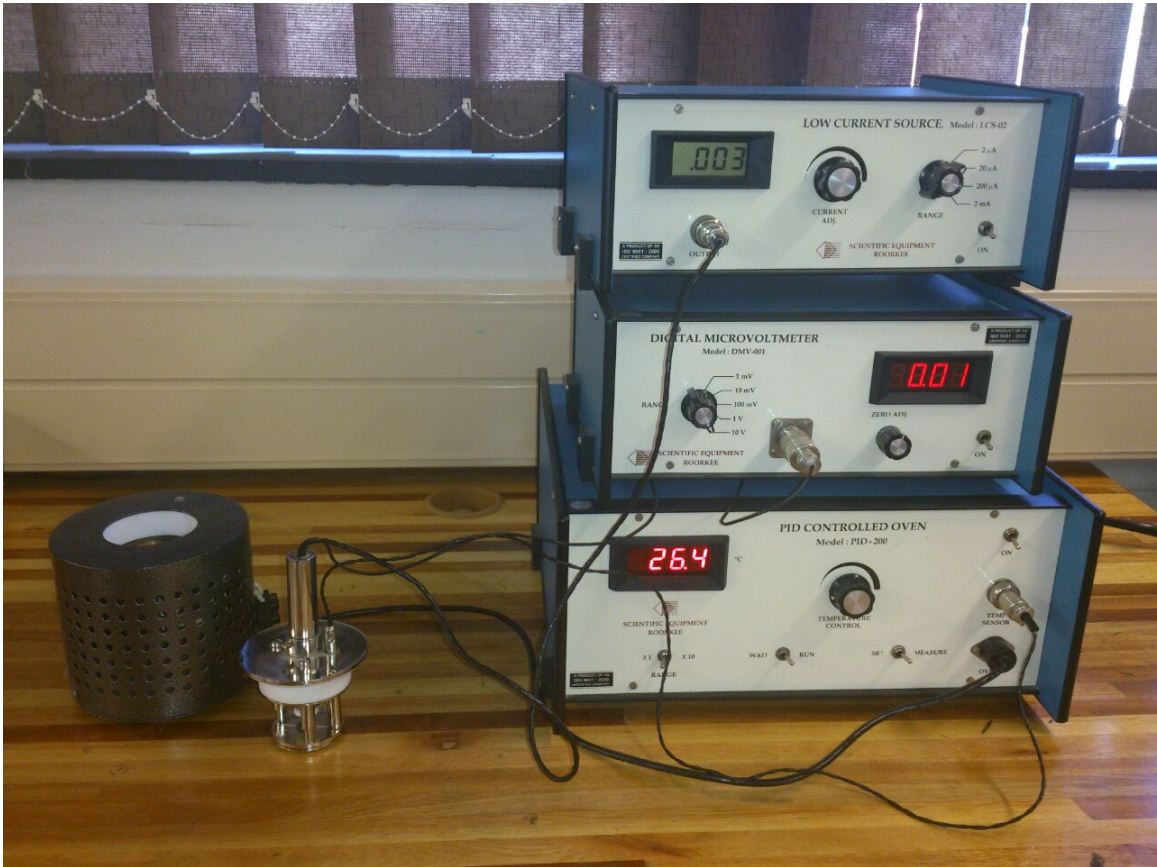
Figure 3.14: The set-up of the four probe experiment for electrical resistivity against temperature.
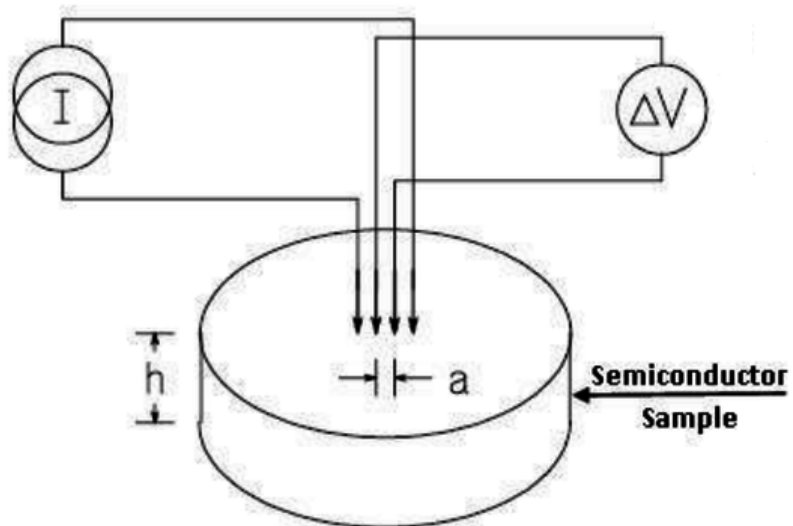
Figure 3.15: The arrangement of the four probes [48].

where E_2 is the activation energy. By plotting the graphs of $\ln \rho$ against $T^{-1/2}$ and $\ln \rho$ against T^{-1}, the energy gaps E_1 and E_2 can be determined from the slopes of the linear fits.

3.7 Other techniques

We also performed measurements using a variety of other techniques and equipment which are not discussed here in detail. These included the estimation of the morphology of our samples by a Jeol-JEM 2100 high-resolution transmission electron microscopy (HRTEM). A Zeiss Evo LS15 scanning electron microscopy (SEM) was used for qualitative measurements of elemental compositions of samples by the energy-dispersive X-ray (EDX) method. A Sentrotech tube furnace was used for the annealing of our pellet samples.

Chapter 4

Properties of $Ni_xCo_{1-x}Fe_2O_4$ nanoferrites

4.1 Introduction

The magnetic properties of nanoferrites are influenced by the cations distribution on both A and B sites. $CoFe_2O_4$ has a partially inverse spinel structure and is known to be a hard magnet with a high coercivity and moderate saturation magnetization. These properties, together with the high magnetocrystalline anisotropy of Co^{2+} ions, make $CoFe_2O_4$ nanoferrite highly suitable for high density information storage systems, drug delivery and biomedical applications [23, 49]. The properties can also be manipulated by doping or substituting Co in $CoFe_2O_4$ with different cations. On the other hand $NiFe_2O_4$ which has also been identified for applications in biomedical science and recording media is a soft magnet with an inverse spinel structure [23, 50]. Systematic substitution of Co^{2+} with Ni^{2+} cations in $CoFe_2O_4$ has been studied previously resulting in different properties due to a variety of synthesis techniques and sintering temperatures [3, 12, 25, 51].

Choi *et al.* [3] have studied the series of $Ni_xCo_{1-x}Fe_2O_4$ prepared by the sol-gel method which were annealed at 600 °C. The particle sizes (25.0 to 16.6 nm) and lattice parameters (0.835 to 0.833 nm) decreased with increasing Ni content. The coercivity (1.48 to 0.37 kOe) and saturation magnetization (85.38 to 35.78 emu/g) were also found to decrease with increasing Ni content which were found to correlate

with the particle sizes. Mössbauer analysis revealed ferrimagnetic behaviour for the nanoparticles. Singhal *et al.* [12] produced $Ni_xCo_{1-x}Fe_2O_4$ nanoparticles by the aerosol route and found particle sizes ranging from 10 to 80 nm after annealing at 1200 °C. Maaz *et al.* [51] produced their nanoparticles using the co-precipitation route and annealed the samples at 600 °C. They found that the blocking temperature decreased with increasing Ni content due to the lower anisotropy of Ni. Kambale *et al.* [25] prepared their samples using the standard ceramic technique. They found electrical resistivity and activation energy (0.30 to 0.22 eV) to decrease with increasing Co content.

In this chapter we investigate the evolution of the structural, magnetic and electrical properties as the Co^{2+} ions are substituted by the Ni^{2+} cations. The nanoparticles of $Ni_xCo_{1-x}Fe_2O_4$ ($x = 0.0$ to 1.0 incremented by 0.1) were synthesized by the low temperature glycol-thermal technique at 200 °C without any further sintering. Characterizations were performed by X-ray diffraction (XRD), ^{57}Fe Mössbauer spectroscopy, vibrating sample magnetometer (VSM) and four probe resistivity measurement method.

4.2 Results and discussion

4.2.1 X-ray diffraction

The XRD patterns for $Ni_xCo_{1-x}Fe_2O_4$ shown in Figure 4.1 confirm the formation of single phase cubic spinel structure as per the PDF cards of pure $CoFe_2O_4$ and $NiFe_2O_4$ [51]. However, the samples $x = 0.7$ to 0.9 do indicate some impurity peaks at $2\theta \approx 52°$ and 62°. As the nickel content x increases, the Ni^{2+} ions experience difficulty to fit into the B sites of the inverse spinel structure which are occupied by the Co^{2+} and Fe^{3+} ions. So some of the Ni^{2+} ions (for samples $x = 0.7$ to 0.9) are pushed out of the spinel structure and combine with Fe ions to form NiFe. The observed extra peaks (at $2\theta \approx 52°$, 62°) have been reported for NiFe as a result of the partial reduction of $NiFe_2O_4$ [52]. Table 4.1 shows the variation of the crystallite size D, lattice parameter a and XRD density ρ_{XRD} with the nickel content x. The sample preparation pressure P is the pressure inside the pressure reactor that was
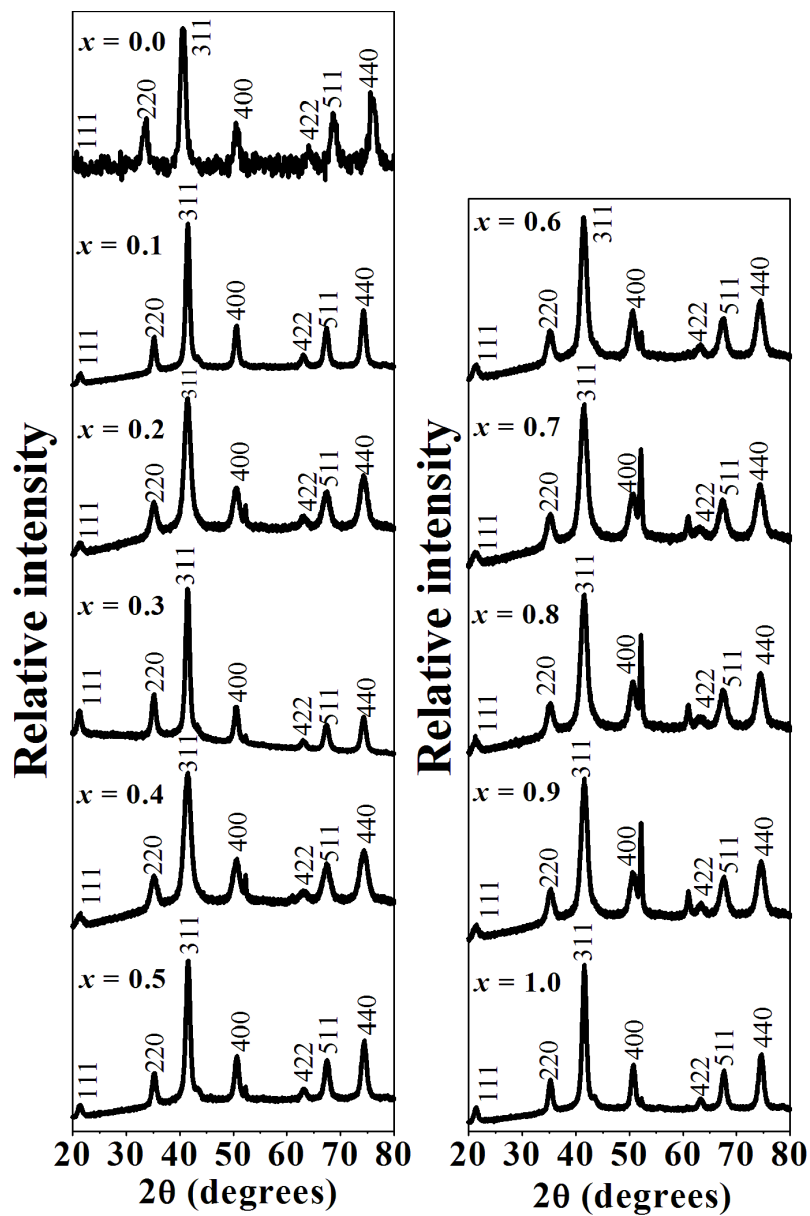
Figure 4.1: X-ray diffraction (XRD) patterns for the as-prepared $Ni_xCo_{1-x}Fe_2O_4$ nanoferrites at room temperature.

recorded during the reaction process at a temperature of 200 °C. The crystallite sizes D, calculated by the Scherrer Equation (3.3.4), range from 7.85 nm to 13.62 nm across the series.

Table 4.1: Sample preparation pressure P, crystallite size D, lattice parameter a and XRD density ρ_{XRD} for the as-prepared $Ni_xCo_{1-x}Fe_2O_4$ nanoferrites.

x	P (psi)	D (nm)	a (Å)	ρ_{XRD} (g/cm^3)
		± 0.06	± 0.006	± 0.01
0.0	70	10.90	8.386	5.28
0.1	140	13.62	8.377	5.30
0.2	50	8.60	8.379	5.30
0.3	110	13.12	8.381	5.29
0.4	40	8.13	8.377	5.30
0.5	110	12.79	8.366	5.32
0.6	60	9.09	8.373	5.31
0.7	40	7.85	8.374	5.30
0.8	50	8.42	8.365	5.32
0.9	40	8.54	8.355	5.34
1.0	120	13.08	8.355	5.34

The particle sizes of the series $Ni_xCo_{1-x}Fe_2O_4$ have previously been reported to decrease with x [3, 12]. However, in the current work, D seems to be highly correlated with the synthesis pressure P as shown in Figure 4.2. Gubicza et al. [53] have reported a direct correlation between the particle size and pressure. This is confirmed by a strong linear correlation between D and P with $\chi^2 = 0.95837$ in the present set of samples as shown in Figure 4.3.

The lattice parameter was calculated by Equation (3.3.3) and is found to decrease with x from 8.386 Å ($x = 0.0$) to 8.355 Å ($x = 1.0$). This is expected since Ni has a smaller ionic radius than Co [3]. These results are close to those previously reported
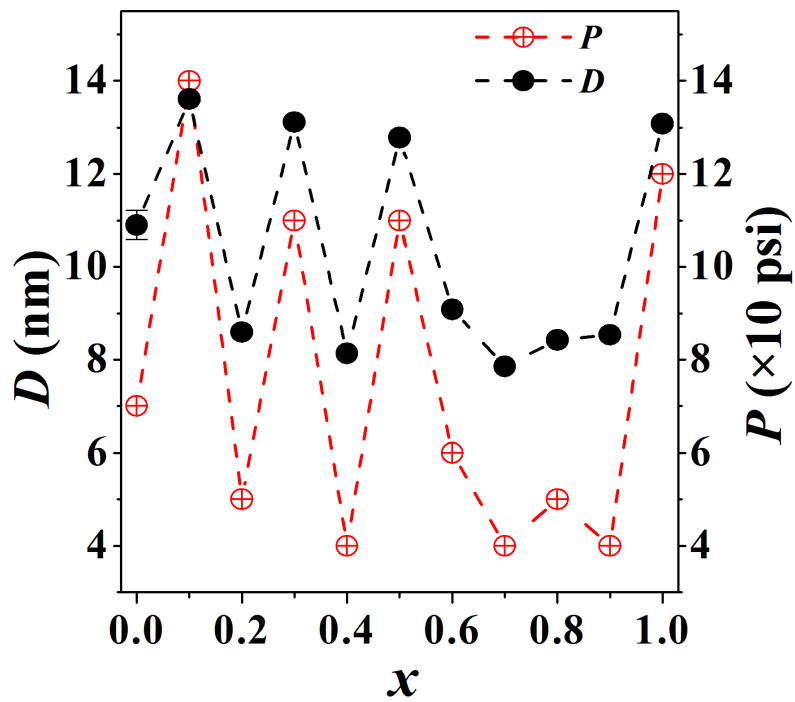
Figure 4.2: Variation of the crystallite size and reaction pressure with x for $Ni_xCo_{1-x}Fe_2O_4$ nanoferrites.
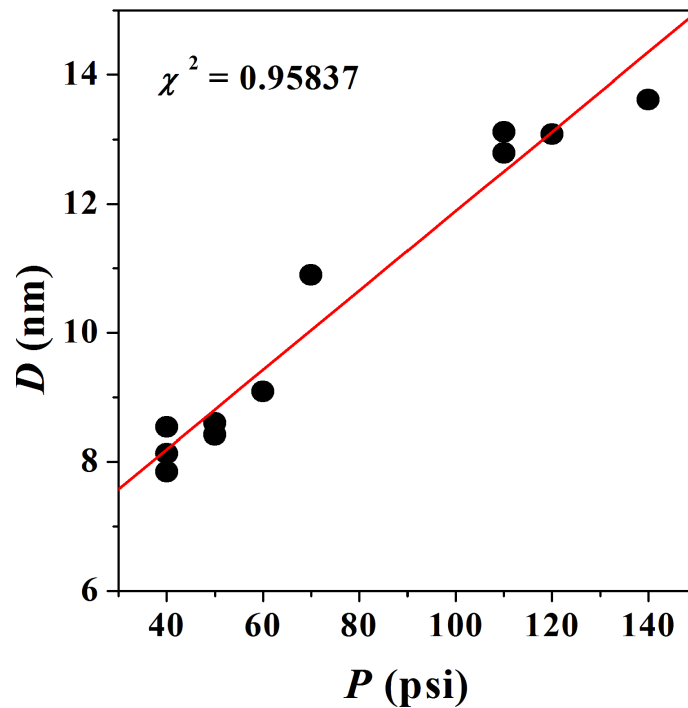
Figure 4.3: The correlation between the crystallite sizes D and synthesis pressure P for $Ni_xCo_{1-x}Fe_2O_4$ nanoferrites.

for $CoFe_2O_4$ and $NiFe_2O_4$ [12]. The lattice parameter as a function of the Ni content is shown in Figure 4.4. The XRD density was calculated from the lattice parameter
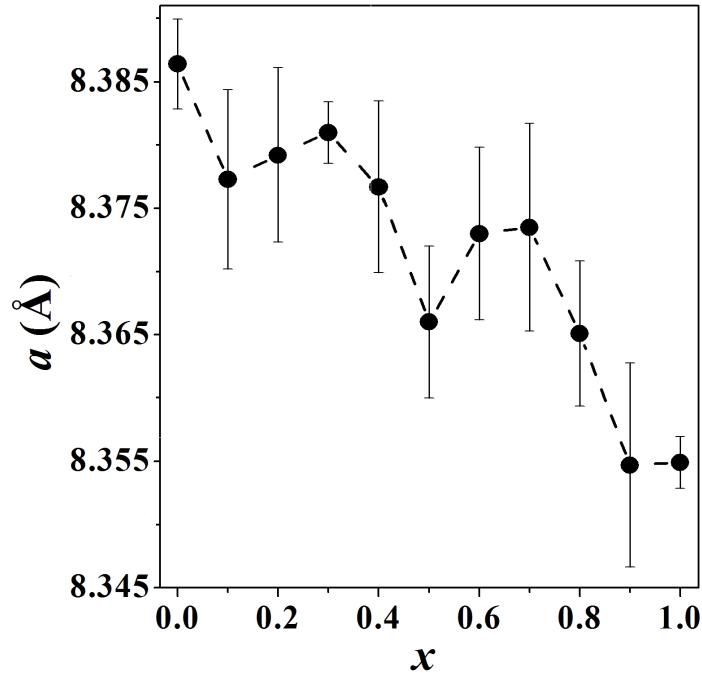
Figure 4.4: Lattice parameter for $Ni_xCo_{1-x}Fe_2O_4$ nanoferrites.

by Equation (3.3.6). ρ_{XRD} increases in this case from 5.28 g/cm^3 ($x = 0.0$) to 5.34 g/cm^3 ($x = 1.0$). Figure 4.5 shows the variation of the XRD density with increasing x which show that the nanoferrites become more compact at higher Ni content.

4.2.2 Mössbauer spectroscopy

Room temperature (about 300 K) ^{57}Fe Mössbauer spectra for the $Ni_xCo_{1-x}Fe_2O_4$ nanoferrites are shown in Figure 4.6. The spectra were fitted with two Zeeman sextets and one doublet. The sextets correspond to the magnetically ordered Fe^{3+} ions on the A and B sites and the doublet accounts for the Fe^{3+} ions in paramagnetic states. The bigger values of the hyperfine fields were allocated to the B site. The symmetry of the A and B sites suggests that the hyperfine fields, together with the isomer shifts, at the B sites should be bigger than those at the A sites [10]. The spectra reveal a ferrimagnetic state for samples $x = 0.0$ to 0.6 and $x = 1.0$ [9, 54]. The line widths are broadened for smaller particle sizes and the doublet areas are
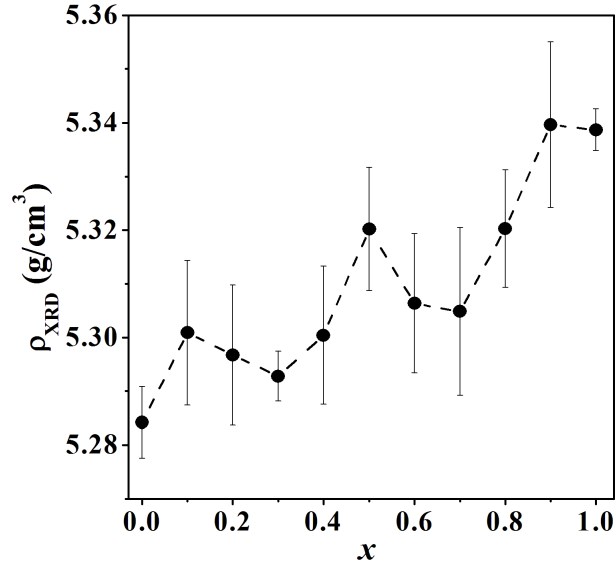
Figure 4.5: Variation of the X-ray density ρ_{XRD} with x for $Ni_xCo_{1-x}Fe_2O_4$ nanoferrites.

increased. The samples $x = 0.7$ to 0.9 have more particles in a paramagnetic state at room temperature which may be due to their smaller particle size as well as the impurities in the structures of these nanoparticles. Table 4.2 shows the variation of the isomer shift σ, hyperfine field H, line width Γ and site population f for $Ni_xCo_{1-x}Fe_2O_4$ nanoferrites at room temperature. The isomer shifts do not change much with x. The σ values are close to previously reported for the same series [3]. The variation of the hyperfine fields at A and B sites is shown in Figure 4.7. The hyperfine fields seem to correlate with the particle sizes for $x = 0.0$ to 0.6. The hyperfine fields for $x = 0.7$ to 0.9 are smaller due to the smaller particle sizes and significant paramagnetic behaviour in these samples [54].

The samples $x = 0.1, 0.5, 0.7$ and 0.9 were selected for low temperature (at 80 K) Mössbauer measurements. The selections were made because the sample $x = 0.1$ has the biggest hyperfine fields at room temperature, $x = 0.5$ has equal compositions of Co and Ni and $x = 0.7, 0.9$ samples display a paramagnetic behaviour at room temperature. Figure 4.8 shows the Mössbauer spectra at (a) 80 K and (b) room temperature (RT) for the four samples. As expected, well resolved six line spectra are observed for all the samples at 80 K. The spectra were fitted with two sextets
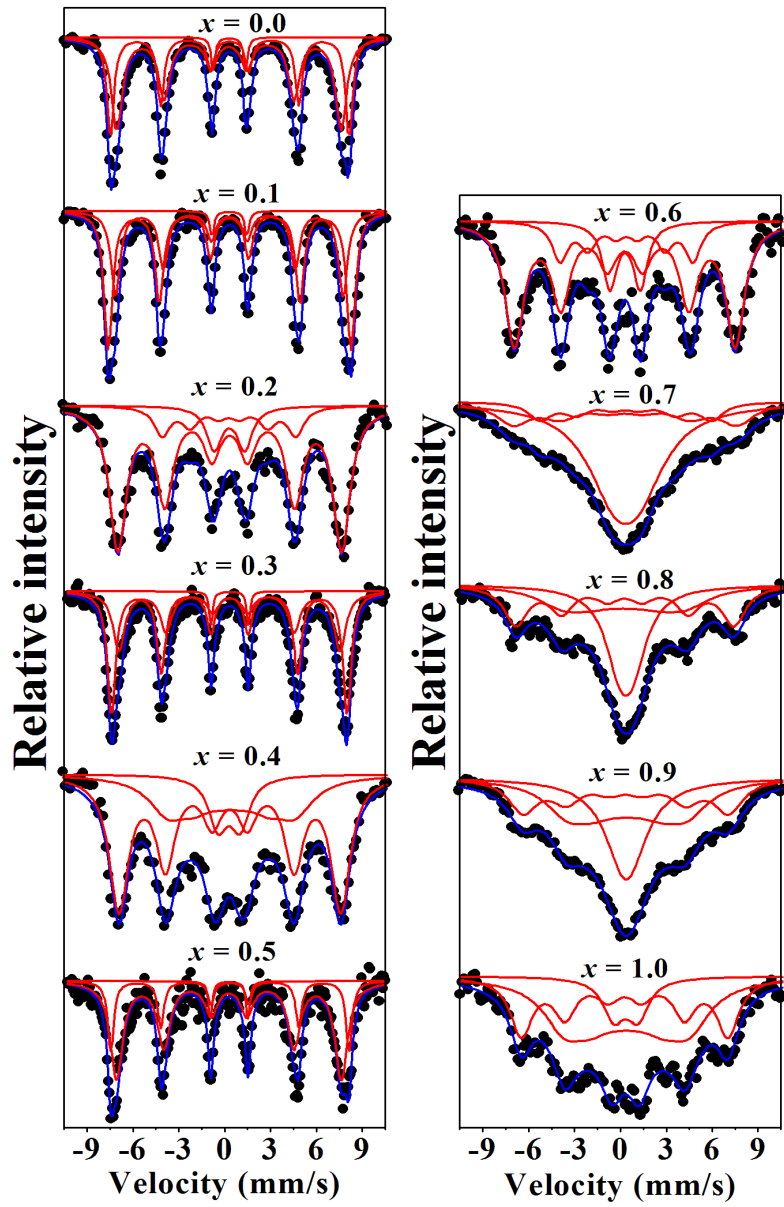
Figure 4.6: Mössbauer spectra for $Ni_xCo_{1-x}Fe_2O_4$ nanoferrites at room temperature.

Table 4.2: Variation of the isomer shift σ, hyperfine field H, line width Γ and site population f for $Ni_xCo_{1-x}Fe_2O_4$ nanoferrites at room temperature.

x	σ_A (mm/s)	σ_B (mm/s)	H_A (kOe)	H_B (kOe)	Γ_A (mm/s)	Γ_B (mm/s)	f_A (%)	f_B (%)
	±0.08	±0.06	±8	±5	±0.09	±0.08	±6	±5
0.0	0.28	0.33	455	484	0.43	0.28	58	40
0.1	0.30	0.32	461	492	0.35	0.33	39	58
0.2	0.28	0.33	271	454	0.63	0.66	15	75
0.3	0.34	0.31	449	478	0.47	0.33	39	58
0.4	0.43	0.33	260	450	1.46	0.75	28	61
0.5	0.28	0.34	456	483	0.49	0.24	71	25
0.6	0.40	0.29	269	448	0.62	0.72	18	68
0.7	0.35	0.31	347	453	0.91	1.35	13	24
0.8	0.21	0.29	251	442	1.90	0.91	30	35
0.9	0.44	0.36	242	417	1.70	1.13	39	30
1.0	0.41	0.28	254	419	1.70	0.88	51	37
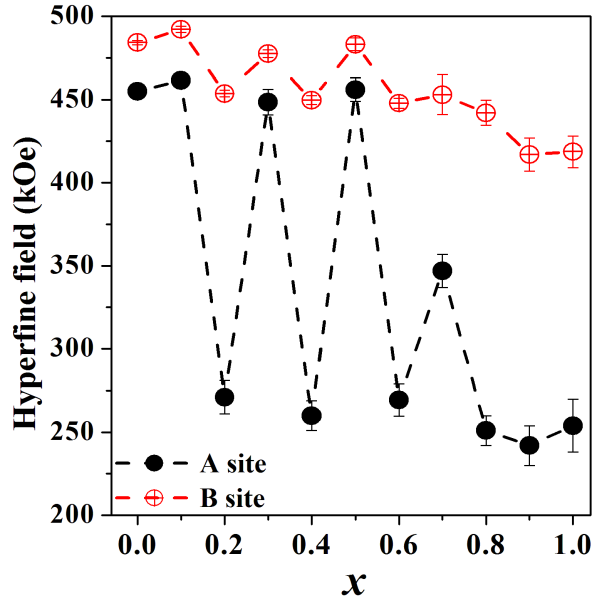
Figure 4.7: Hyperfine fields at A and B sites for $Ni_xCo_{1-x}Fe_2O_4$ nanoferrites at room temperature.

and one doublet. The doublet areas become smaller at 80 K, in comparison with room temperature, which is expected [54]. This means there are fewer nanoparticles in a paramagnetic state [9]. The Mössbauer parameters at 80 K are shown in Table 4.3. A general enhancement of the isomer shifts and hyperfine fields are observed. The line widths are much sharper at 80 K, notably for $x = 0.7$ and 0.9 which have broader widths at room temperature.

The variations of hyperfine fields at 80 K and room temperature for the A and B sites are shown in Figure 4.9. The hyperfine fields at 80 K are clearly more enhanced than those at room temperature. The sample with $x = 0.5$ has the largest hyperfine fields and the least nanoparticles in a paramagnetic state based on site populations.

The sample with $x = 0.1$ was further selected for Mössbauer analysis against temperature. The Mössbauer spectra at $T = 80$ K to 483 K are shown in Figure 4.10. Not much change in the spectra is observed from $T = 80$ K to 273 K. The changes begin to appear at $T = 323$ K and 373 K. At 423 K, a doublet becomes more enhanced which suggests increased disorder of the magnetic moments and therefore leading to magnetic order collapse. A further increase in temperature from
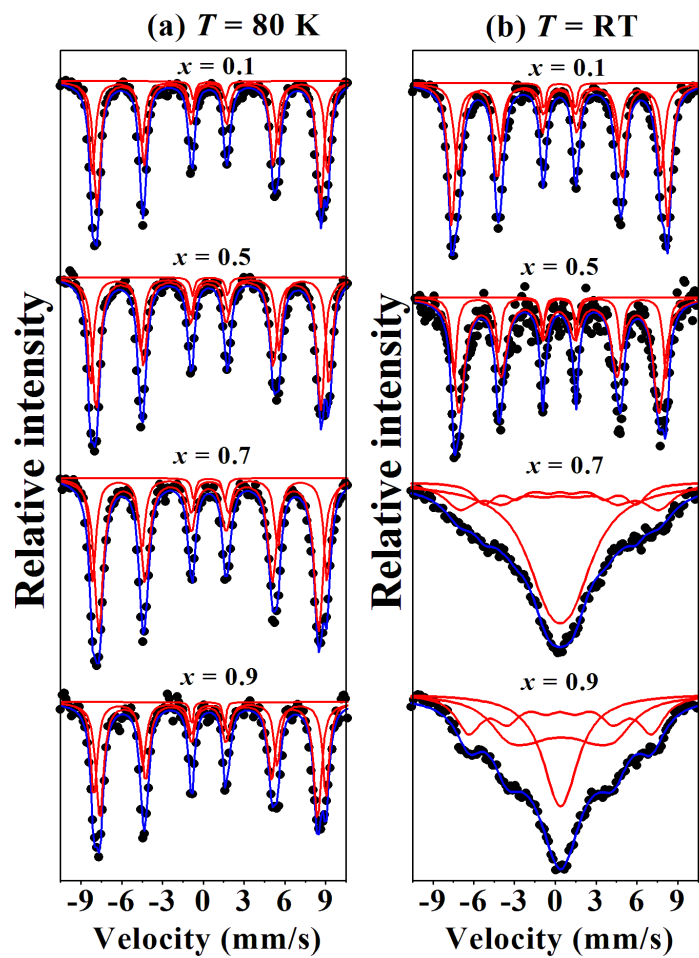
Figure 4.8: Mössbauer spectra for $Ni_xCo_{1-x}Fe_2O_4$ ($x = 0.1$, 0.5, 0.7 and 0.9) at (a) 80 K and (b) room temperature.

Table 4.3: Variation of the isomer shift σ, hyperfine field H, line width Γ and site population f for $Ni_xCo_{1-x}Fe_2O_4$ nanoferrites at 80 K.

x	σ_A (mm/s)	σ_B (mm/s)	H_A (kOe)	H_B (kOe)	Γ_A (mm/s)	Γ_B (mm/s)	f_A (%)	f_B (%)
	±0.01	±0.01	±2	±2	±0.03	±0.04	±4	±4
0.1	0.40	0.49	509	536	0.29	0.27	58	40
0.5	0.37	0.47	512	544	0.33	0.28	58	41
0.7	0.40	0.48	501	535	0.39	0.30	64	33
0.9	0.39	0.49	496	529	0.33	0.29	57	41
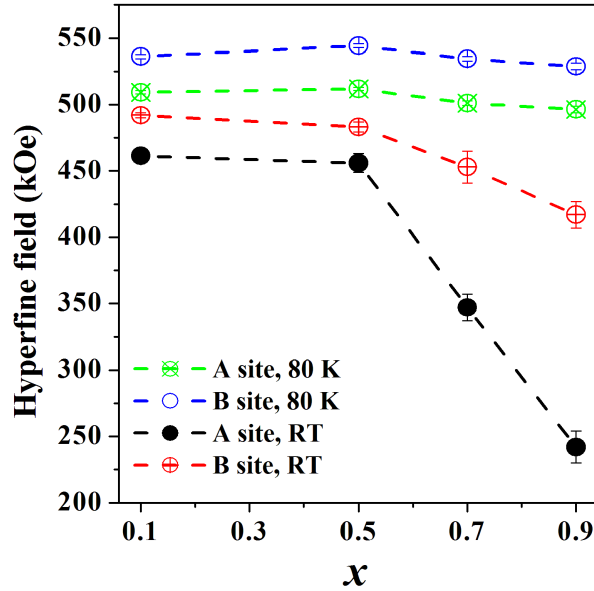
Figure 4.9: Hyperfine fields at A and B sites for $Ni_xCo_{1-x}Fe_2O_4$ ($x = 0.1$, 0.5, 0.7 and 0.9) nanoferrites at 80 K and room temperature (RT).

473 K to 483 K leads to total magnetic order collapse where the spectrum is only fitted by two doublets (at 483 K). The evolution of the isomer shifts σ, hyperfine
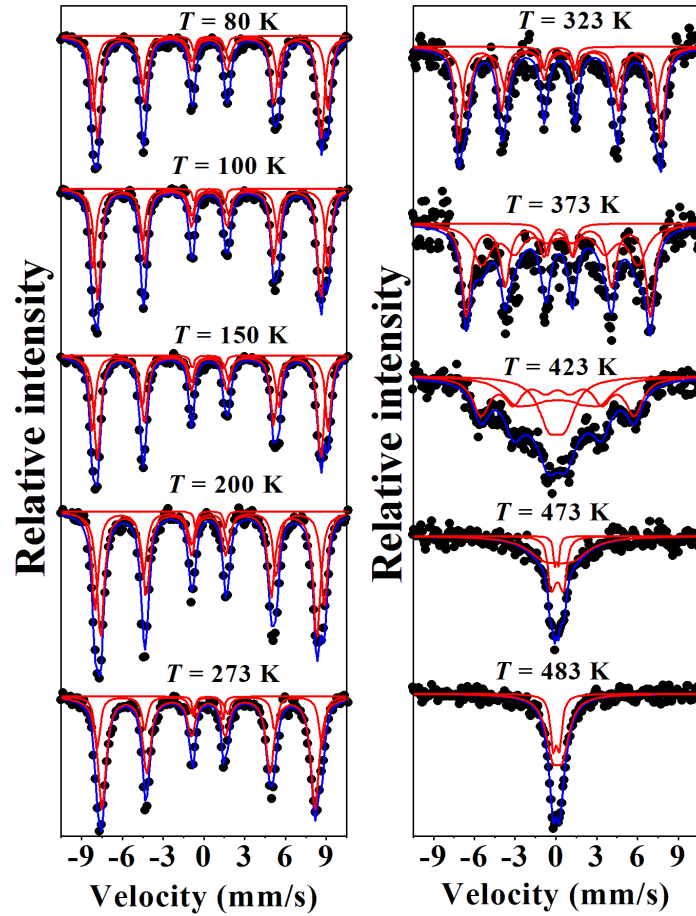
Figure 4.10: Mössbauer spectra for $Ni_{0.1}Co_{0.9}Fe_2O_4$ nanoferrite as a function of temperature.

fields H, line widths Γ and site populations f for $Ni_{0.1}Co_{0.9}Fe_2O_4$ nanoferrites with temperature are shown in Table 4.4. A general increase in the doublet area from 273 K to 483 K is observed, which further suggests a magnetic phase transition in this temperature range. Figure 4.11 shows the variation of the hyperfine fields with temperature. There is a gradual decrease in hyperfine fields at $T \leq 273$ K, after which the decrease becomes more drastic until zero fields are reached at 483 K. We estimate a total magnetic phase transition at about 478 K in the temperature region 473 K$\leq T \leq$483 K. The isomer shifts also show significant temperature dependence as illustrated in Figure 4.12.

Table 4.4: Evolution of the isomer shift σ, hyperfine field H, line width Γ and site population f for $Ni_{0.1}Co_{0.9}Fe_2O_4$ nanoferrites with temperature.

T (K)	σ_A (mm/s)	σ_B (mm/s)	H_A (kOe)	H_B (kOe)	Γ_A (mm/s)	Γ_B (mm/s)	f_A (%)	f_B (%)
	±0.07	±0.06	±8	±5	±0.09	±0.08	±8	±9
80	0.40	0.49	509	536	0.29	0.27	58	40
100	0.39	0.48	508	536	0.27	0.26	58	41
150	0.36	0.47	503	532	0.29	0.25	63	35
200	0.35	0.43	493	522	0.31	0.28	58	41
273	0.33	0.42	486	512	0.35	0.24	75	23
323	0.33	0.30	430	461	0.43	0.32	45	51
373	0.29	0.18	356	420	0.78	0.40	42	51
423	0.14	0.13	194	349	1.10	0.74	33	40
473	0.10	0.22	33	82	0.21	1.34	34	60
483	0.00	0.00	0	0	0.00	0.00	0	0
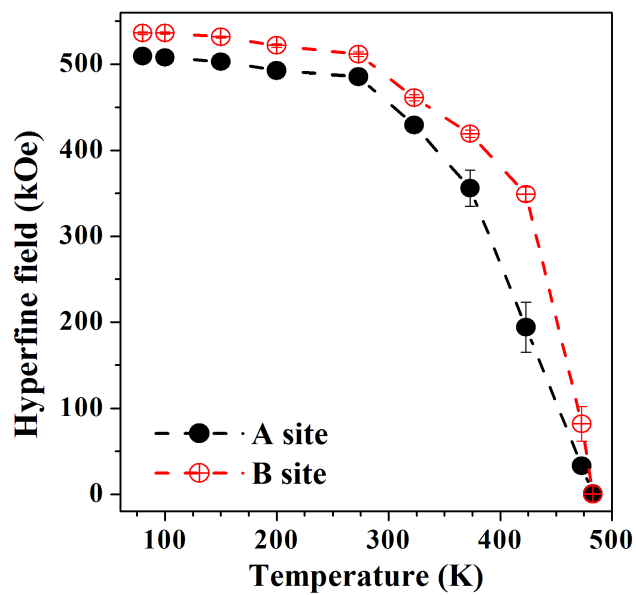
Figure 4.11: Hyperfine fields at A and B sites for $Ni_{0.1}Co_{0.9}Fe_2O_4$ nanoferrite as a function of temperature.
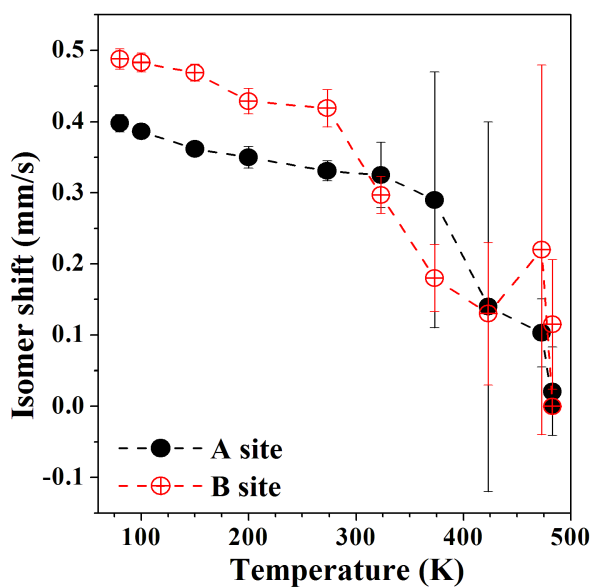
Figure 4.12: Isomer shifts at A and B sites for $Ni_{0.1}Co_{0.9}Fe_2O_4$ nanoferrite as a function of temperature.

4.2.3   Magnetization

The magnetization measurements were investigated on a vibrating sample magnetometer (VSM). The magnetic hysteresis loops for $Ni_xCo_{1-x}Fe_2O_4$ nanoferrites at room temperature are shown in Figure 4.13 for the applied field in the range -14 kOe$\leq H \leq$14 kOe. At the highest applied field $H = 14$ kOe, the magnetization M is not saturated. The samples do not show much coercivity except for $x = 0.1$.
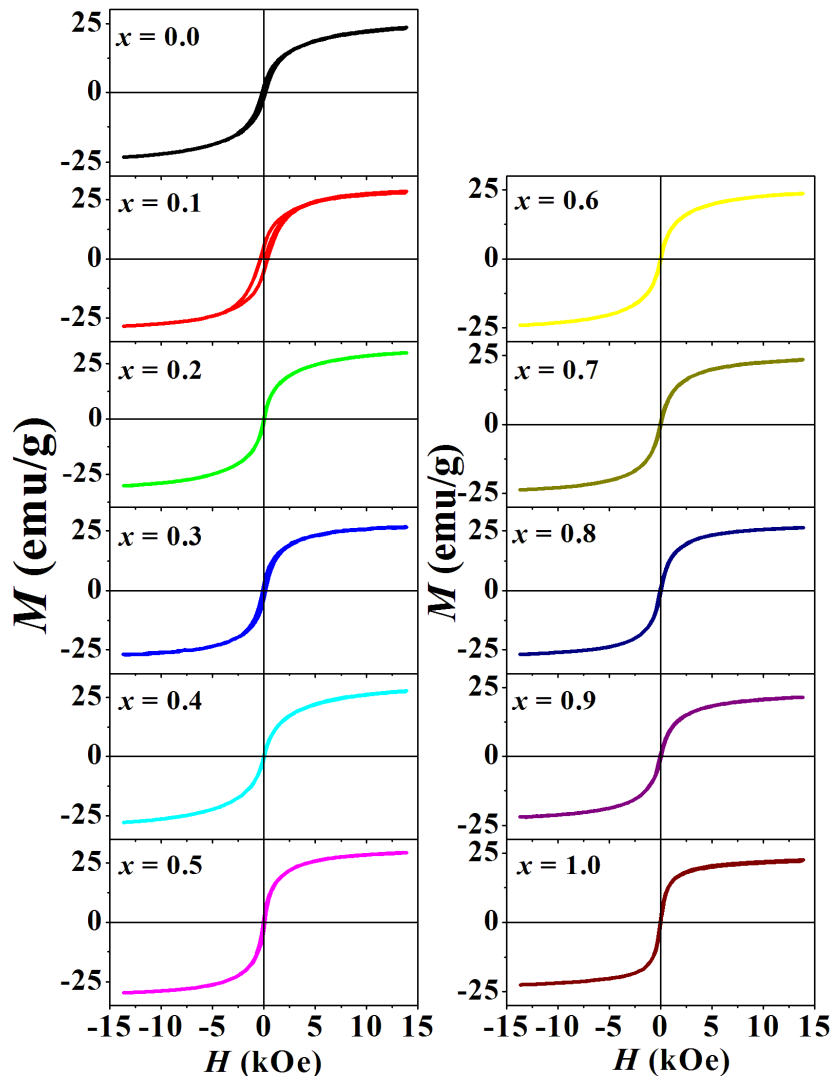
Figure 4.13: Magnetic hysteresis loops for $Ni_xCo_{1-x}Fe_2O_4$ nanoferrites at room temperature.

The small coercivity is usually typical of superparamagnetism of nanoparticles [55]. Table 4.5 shows the variation of coercive fields H_c, magnetization M at a maximum

applied field and remanent magnetization M_r for $Ni_xCo_{1-x}Fe_2O_4$ nanoferrites with the nickel content x at room temperature. The table also includes values of crystallite sizes D and sample preparation pressure P from Table 4.1 which can be related particularly to the coercive fields H_c.

Table 4.5: Coercive field H_c, magnetization M at maximum applied field and remanent magnetization M_r for $Ni_xCo_{1-x}Fe_2O_4$ nanoferrites at room temperature.

x	H_c (Oe)	M (emu/g)	M_r (emu/g)	P (psi)	D (nm)
0.0	147.7	23.4	1.95	70	10.90
0.1	338.8	28.5	5.21	140	13.62
0.2	14.7	30.1	0.33	50	8.60
0.3	124.0	27.0	2.63	110	13.12
0.4	14.7	27.8	0.25	40	8.13
0.5	51.3	29.5	1.51	110	12.79
0.6	13.1	23.9	0.24	60	9.09
0.7	24.6	23.6	0.41	40	7.85
0.8	24.6	26.6	0.55	50	8.42
0.9	28.8	21.7	0.46	40	8.54
1.0	12.8	22.5	0.36	120	13.08

The variation of the coercive fields with the Ni content x is shown in Figure 4.14. The correlation between coercivity and particle size can clearly be seen and confirmed in Figure 4.15. Larger coercivity is observed for bigger particles. This can be explained by Néel relaxation time in Equation (2.4.23) which depends on the particle size. When the relaxation time is smaller than the measurement time, there occurs magnetization flips within a material which then create randomly directed magnetic moments. This decreases the total magnetization of the material. So when the relaxation time is bigger than the measurement time, the magnetic moments maintain the same direction during measurement, which increases the

magnetization. The sample $x = 0.1$ has the largest coercive field in the series. This is consistent with the highest values of hyperfine fields and highest D values as well as highest synthesis pressure P of 140 psi.
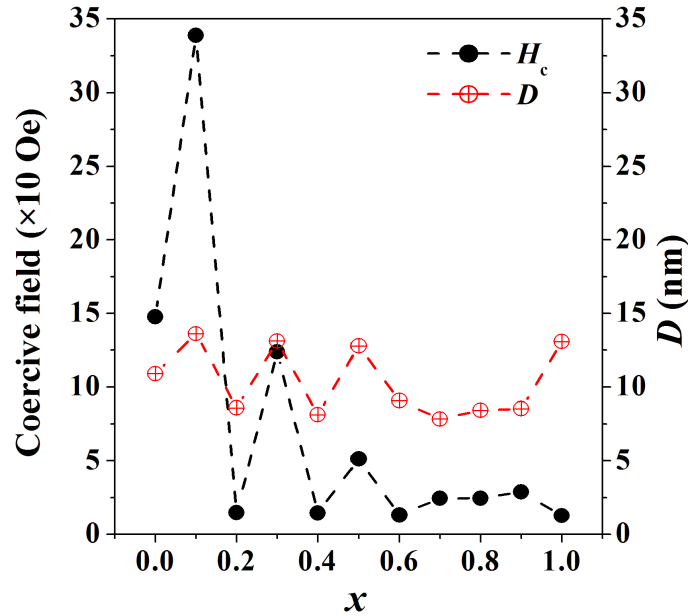
Figure 4.14: Coercivity of the $Ni_xCo_{1-x}Fe_2O_4$ nanoferrites.

4.2.4 Electrical resistivity

The electrical resistivity measurements in the temperature range $25\,°C \leq T \leq 130\,°C$ were performed using the four probe method on some of the samples. The resistivity was assumed to vary according to the Arrhenius Equation (3.6.3). Figures 4.16 and 4.17 show the plots of $\ln\rho$ against T^{-1} for $Ni_xCo_{1-x}Fe_2O_4$ ($x = 0.8, 0.9$).

Two faces of the same pellet show different slopes which means different energy gaps (activation energy) for the faces. This behaviour has been reported by Abdallah *et al.* [17]. The conduction in these materials can be assumed to be due to electron hopping between the divalent (Ni^{2+}, Co^{2+}) and the trivalent (Ni^{3+}, Co^{3+}, Fe^{3+}) ions. The measured activation energies and resistivities extrapolated to 0 K for $Ni_xCo_{1-x}Fe_2O_4$ ($x = 0.8, 0.9$) are shown in Table 4.6. The results show semiconducting behaviour in the two studied ferrites.
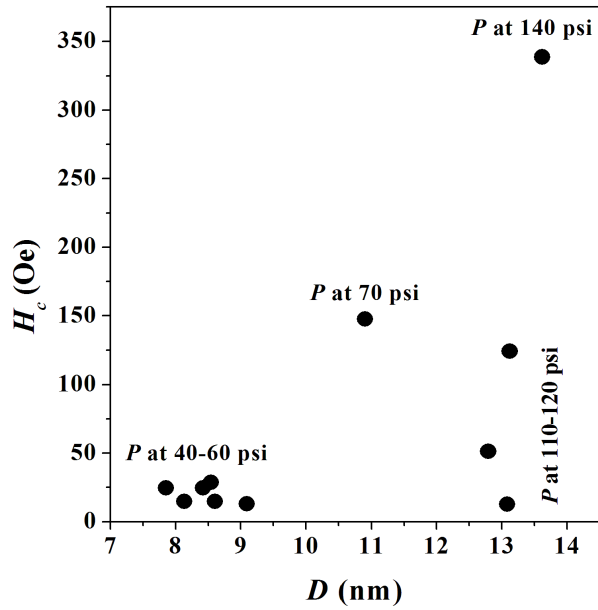
Figure 4.15: The correlation between coercive fields H_c and particle sizes D of the $Ni_xCo_{1-x}Fe_2O_4$ nanoferrites.
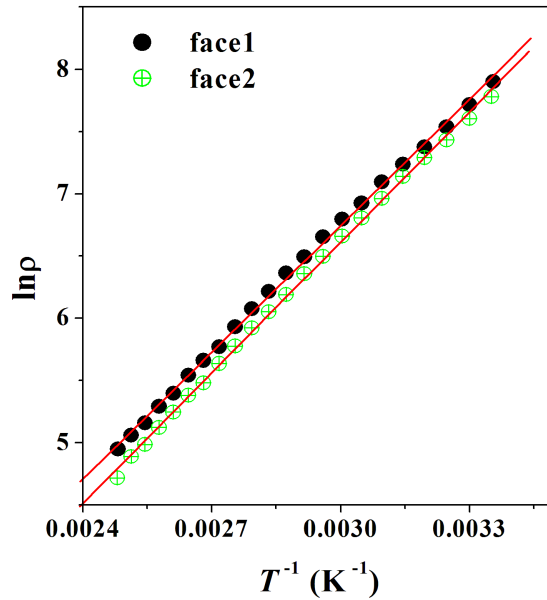
Figure 4.16: Plot of $\ln \rho$ against T^{-1} for $Ni_{0.8}Co_{0.2}Fe_2O_4$.
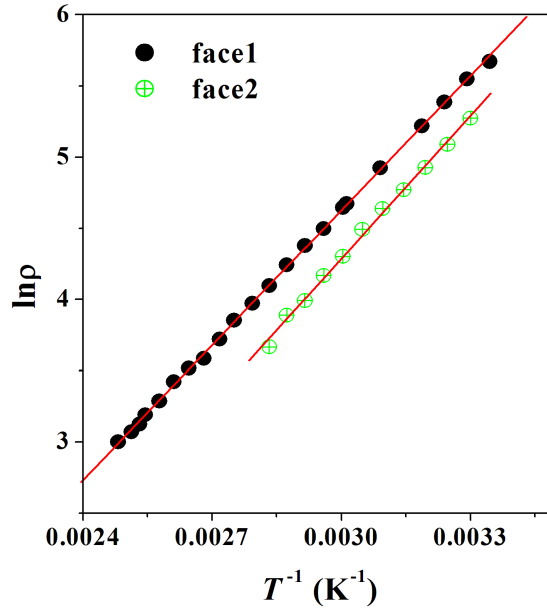
Figure 4.17: Plot of $\ln \rho$ against T^{-1} for $Ni_{0.9}Co_{0.1}Fe_2O_4$.

Table 4.6: Activation energy E_{a1} and resistivity at 0 K ρ_{01} (face 1), E_{a2} and ρ_{02} (face 2) for $Ni_xCo_{1-x}Fe_2O_4$ ($x = 0.8$, 0.9).

x	E_{a1}	ρ_{01}	E_{a2}	ρ_{02}
	(eV)	($\Omega\,m$)	(eV)	($\Omega\,m$)
	± 0.003	± 0.0003	± 0.003	± 0.0003
0.8	0.292	0.0322	0.301	0.0207
0.9	0.272	0.0079	0.288	0.0032

4.3 Conclusions

$Ni_xCo_{1-x}Fe_2O_4$ ($x = 0.0$ to 1.0 incremented by 0.1) nanoferrites were synthesized by the glycol-thermal technique. Single phase cubic spinel formation was confirmed by XRD for nearly all compounds, except $x = 0.7$ to 0.9 nanoferrites which had small impurities that were suspected to be from NiFe. The crystallite sizes that were obtained ranged from 7.85 nm to 13.62 nm. The crystallite sizes appear to be highly correlated to the reaction pressure. Room temperature ^{57}Fe Mössbauer analysis revealed ferrimagnetic behaviour for the nanoparticles $x = 0.0$ to 0.6 and 1.0. The nanoparticles for $x = 0.7$ to 0.9, which had the smallest particle sizes in the series, showed greater doublet areas. The increased paramagnetic behaviour observed in these particles could be due to their small crystallite sizes and impurity phases in their structures. At 80 K, well resolved Mössbauer spectra are achieved for the studied $x = 0.1$, 0.5, 0.7 and 0.9 nanoparticles. The isomer shifts and hyperfine fields are more enhanced. The amount of paramagnetic nanoparticles decreases at 80 K. The hyperfine fields of the sample with $x = 0.1$ across a temperature range 80 K$\leq T \leq$483 K decreased to zero at 483 K where the spectrum was fitted by two doublets only. A total magnetic phase transformation from ferrimagnetism to paramagnetism occurs at about 478 K. Magnetization measurements through hysteresis loops reveal superparamagnetic behaviour for the nanoparticles as confirmed by the Mössbauer analysis. The samples do not reach saturation magnetization at the highest applied field of 14 kOe. There is also high correlation between the coercivity, crystallite sizes and sample preparation pressure. The increased coercive fields at higher crystallite sizes is in line with the transformation from single to multi-domain structure. Electrical resistivity measurements show semiconducting behaviour for the measured pellets which also show differences in properties for the two faces of the same pellet.

Chapter 5

Properties of annealed Ni$_x$Co$_{1-x}$Fe$_2$O$_4$ nanoparticles

5.1 Introduction

Magnetic nanoparticles have attracted tremendous interest recently due to their exciting properties and potential applications in important technologies such as site-specific drug delivery, magnetic separation, magnetic resonance imaging (MRI) and in the treatment of cancer and hyperthermia [56]. Ferrites have high electrical resistivity, relatively high permeability at radio frequencies, low eddy current losses, low power losses and robust mechanical hardness, and hence form an interesting group of magnetic materials [57, 58]. ZnFe$_2$O$_4$ and CoFe$_2$O$_4$ nanoparticles have improved stability, magnetic induction heating and cell viability making them suitable candidates for magnetic hyperthermia, where AC magnetic fields can be used to induce a rise in temperature [56]. NiFe$_2$O$_4$ ferrites are widely used in drug delivery, MRI, ferro-fluids, gas sensors, microwave absorbers and information storage devices due to their high initial permeability and resistivity [59]. Magnetic nanoparticles are known to have large surface-to-volume ratio and size dependent properties. By controlling the particle size and composition, the surface properties can be tuned for possible applications of the nanomaterials. Besides particle size, the properties of ferrites are dependent on microstructure and their composition which are sensitive to sample preparation technique and conditions [60, 61].

Synthesis of the nanophase ferrites has thus become an important part of modern ceramic research. Bulk compounds are usually prepared by solid state reaction method [57, 61–63]. This technique involves prolonged high temperature heat treatments and grinding of the sample during preparation which can lead to mass loss [64]. The control of the desired stoichiometry can therefore be difficult to achieve and there is increased risk of contamination of the sample from the grinding surfaces. Wet chemical methods such as auto-combustion [60, 64, 65], co-precipitation [66], sol-gel [24, 67, 68], oxalate precursor [69] techniques have been developed which do not require high sintering temperatures and do not involve grinding surfaces. Besides low cost, these wet chemical synthesis techniques can produce fine particles directly and the corresponding bulk compounds can be produced by further annealing at higher temperatures. The physical and chemical properties of ferrites are dependent on several factors such as sintering temperature, heating rate, cooling rate, type and amount of dopants and particle size [59]. For example heat treatment effects on the structural and magnetic properties of Mn-doped Ni ferrites prepared by auto-combustion method have been reported by Kumar *et al.* [60, 70]. Abosheiasha *et al.* [59] have also reported sintering effects on the properties of Ca-doped Ni ferrite ($Ni_{0.92}Ca_{0.08}Fe_2O_4$) prepared by citrate precursor method.

$CoFe_2O_4$ is a hard ferrite (has high coercive field and moderate saturation magnetization) with high magnetocrystalline anisotropy associated with Co atoms. It has remarkable chemical stability making it suitable for many practical applications such as audio tapes and high density recording disks [63]. On the other hand, $NiFe_2O_4$ oxide is a soft ferrite with low magnetocrystalline anisotropy. It has applications in electronic devices such as inductors and transformers [24]. Both $CoFe_2O_4$ and $NiFe_2O_4$ in ideal states have inverse spinel structure where all Co^{2+} and Ni^{2+} ions are in octahedral (B) sites and Fe^{3+} ions are equally distributed between tetrahedral A and octahedral B sites. Since A and B sites magnetic moments are antiparallel, the magnetization in these compounds is expected to be influenced more by Co^{2+} ($2 \mu_B$) and Ni^{2+} ($3 \mu_B$) ions. Mixed Ni-Co ferrites can be expected to have unique properties which could be significantly different from pure Ni-ferrite or Co-ferrite.

In this chapter we report on changes to properties of two mixed Ni-Co ferrites

due to changes in crystallite sizes induced by thermal annealing. The as-prepared $Ni_{0.3}Co_{0.7}Fe_2O_4$ ($x = 0.3$) and $Ni_{0.5}Co_{0.5}Fe_2O_4$ ($x = 0.5$) nanosized compounds were chosen for this study because these samples had the greatest crystallite sizes in the series. The choice of $x = 0.3$ and $x = 0.5$ is also pertinent for the present study because one composition has equal atomic proportion of Co and Ni, and the other has slightly more Co content in order to confirm the role of increased magnetocrystalline anisotropy. We have published this work in the Journal of Alloys and Compounds [71].

5.2 Results and discussion

5.2.1 X-ray difraction

The XRD data was used to confirm formation of cubic spinel phase of the compounds and to estimate sizes of the fine particles produced. The XRD spectra of the oxides annealed at different temperatures are shown in Figure 5.1. The reflections from the atomic planes 111, 220, 311, 400, 422, 511 and 440 are identified and are characteristic of single phase cubic spinel structure of $CoFe_2O_4$ and $NiFe_2O_4$ phases according to PDF cards (791744 for $CoFe_2O_4$ and 742081 for $NiFe_2O_4$) [51]. The crystallite size values listed in Tables 5.1 and 5.2 were calculated using the Debye-Scherrer formula [24, 65, 66]. The narrowing of the peaks with increasing sintering temperature indicates increasing particle size. As shown in Figure 5.2, crystallite sizes increase with increasing annealing temperature from about 13 nm to about 110 nm after annealing at 1100 °C.

Typical values of lattice parameters a, deduced from XRD data are shown in Tables 5.1 and 5.2 for $Ni_{0.3}Co_{0.7}Fe_2O_4$ and $Ni_{0.5}Co_{0.5}Fe_2O_4$ oxides respectively. There is no significant change in the lattice parameter with increasing annealing temperature. The X-ray densities computed from the values of lattice parameters [58] are also given in Tables 5.1 and 5.2. These are comparable to those reported previously for similar bulk compounds [58, 72].
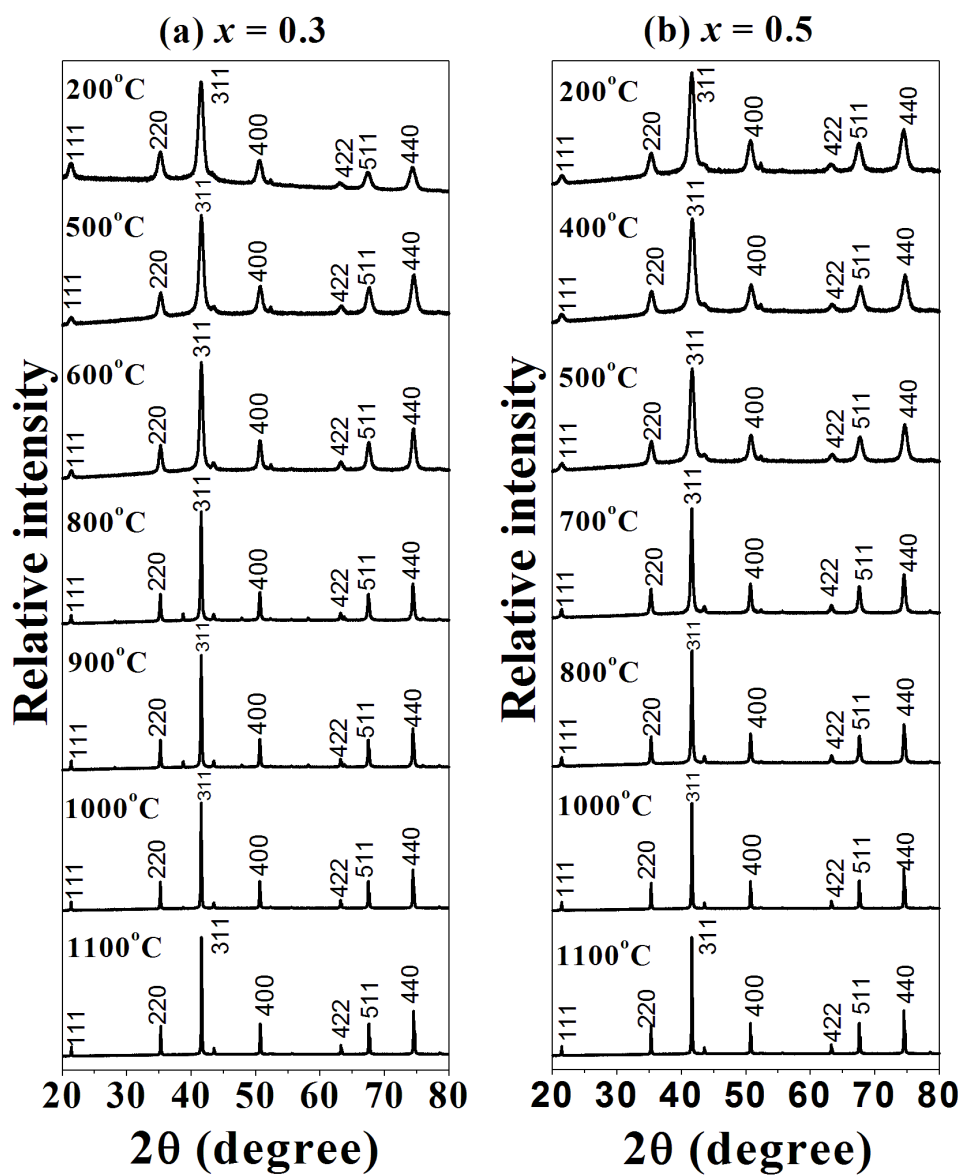
Figure 5.1: X-ray diffraction (XRD) patterns for the $Ni_xCo_{1-x}Fe_2O_4$ where $x = 0.3$, 0.5.

Table 5.1: Crystallite size D, lattice parameter a and XRD density ρ_{XRD} with increasing annealing temperature for $Ni_{0.3}Co_{0.7}Fe_2O_4$.

T	D	a	ρ_{XRD}
(°C)	(nm)	(Å)	(g/cm^3)
	±0.2	±0.001	±0.01
200	12.9	8.383	5.29
500	15.1	8.364	5.33
600	17.8	8.364	5.32
700	29.8	8.375	5.30
800	41.9	8.372	5.31
900	51.6	8.373	5.31
1000	93.8	8.372	5.32
1100	111.4	8.371	5.31

Table 5.2: Crystallite size D, lattice parameter a and XRD density ρ_{XRD} with increasing annealing temperature for $Ni_{0.5}Co_{0.5}Fe_2O_4$.

T	D	a	ρ_{XRD}
(°C)	(nm)	(Å)	(g/cm^3)
	±0.2	±0.001	±0.01
200	12.9	8.366	5.30
400	13.5	8.347	5.30
500	16.1	8.353	5.29
700	28.9	8.364	5.30
800	40.9	8.364	5.32
900	57.2	8.362	5.33
1000	64.8	8.361	5.32
1100	91.7	8.364	5.31
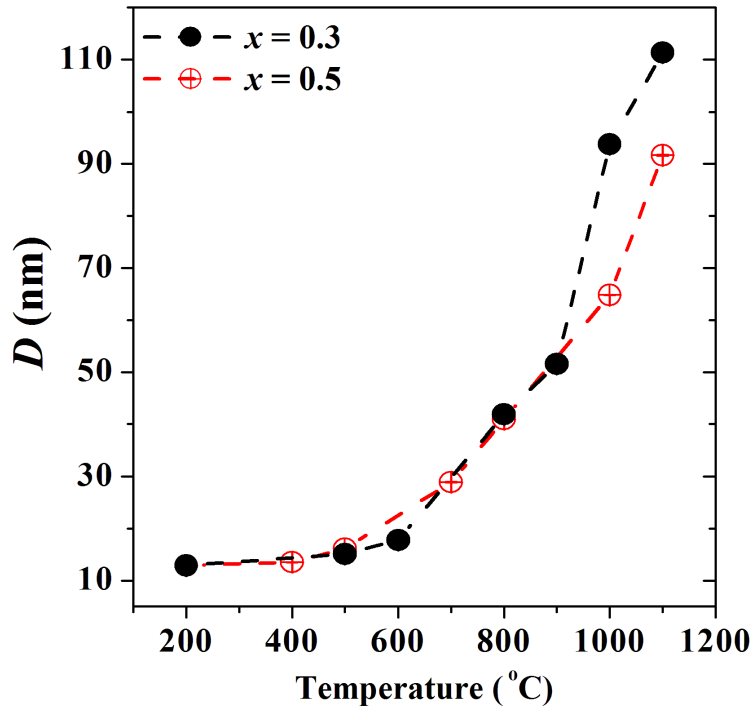
Figure 5.2: Variation of the crystallite size with increasing annealing temperature for $Ni_xCo_{1-x}Fe_2O_4$ where $x = 0.3, 0.5$.

5.2.2 FTIR, HRSEM and HRTEM

In Figure 5.3 we show typical Fourier transform infrared (FTIR) spectra recorded in the frequency range 380-4000 cm^{-1} as a function of annealing temperature. The two strong absorption bands between 380 cm^{-1} and 600 cm^{-1} are indicative of cubic spinel phase [58]. The bands centered at about 400 cm^{-1} and 550 cm^{-1} are due to vibrations at the octahedral (B) and tetrahedral (A) sites respectively. The difference in the peak positions is related to distances Fe^{3+} to O^{2-} at A or B sites [61, 62]. There is no significant change in the peak positions observed with increasing particle size. A higher mode of vibration (wave number) at the A compared to B sites may be due to shorter bond length of the metal-oxygen (Fe^{3+}-O^{2-}) at the tetrahedral sites [73]. A weak band at about 1000 cm^{-1} could be due to small amounts of chloride ions left during the washing stage in the synthesis process. The bands corresponding to wave numbers about 1600 cm^{-1} and 3400 cm^{-1} for the as-prepared sample are associated with bending and stretching of H-O-H bonds [6]
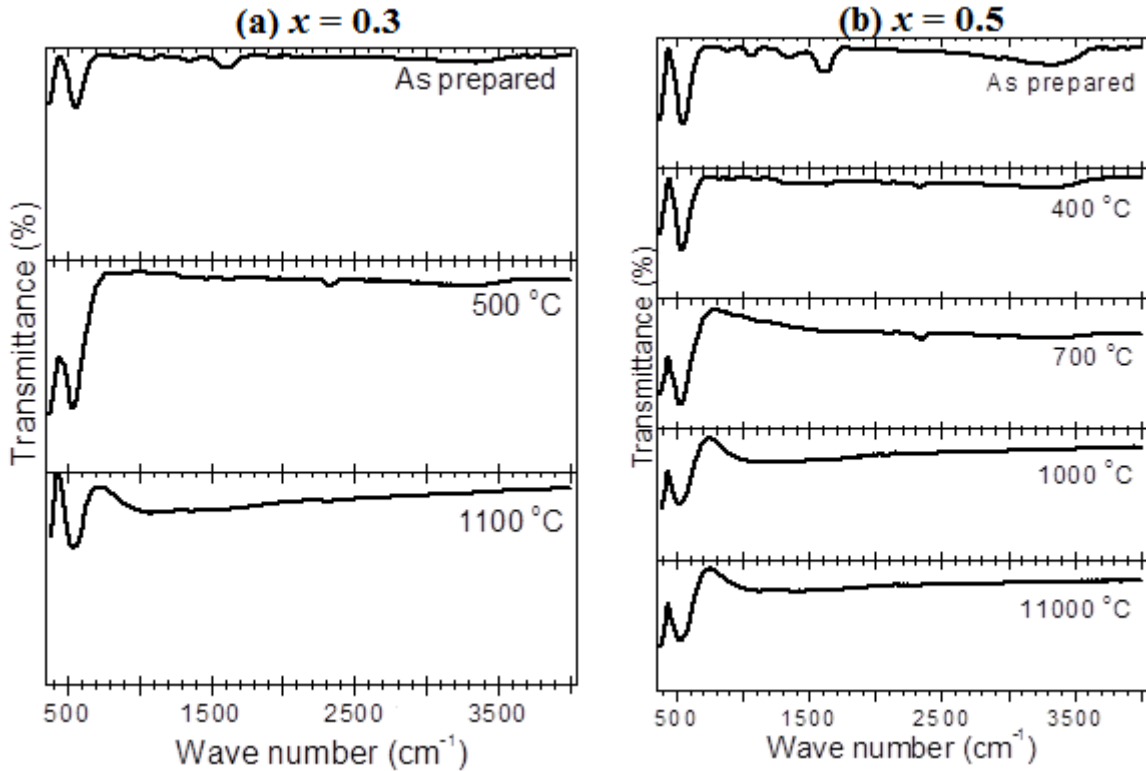
Figure 5.3: FTIR for the $Ni_xCo_{1-x}Fe_2O_4$ where (a) $x = 0.3$ and (b) $x = 0.5$.

showing the presence of free absorbed water. These bands disappear after annealing the as-prepared sample above 400 °C. The absorption band at about 2400 cm^{-1} is attributed to atmospheric CO_2 [73]. This was not observed in samples annealed at temperatures higher than 900 °C.

The elemental compositions of the as-prepared $Ni_xCo_{1-x}Fe_2O_4$ ($x = 0.3$, 0.5) were deduced by the energy dispersive X-ray (EDX) measurements. The EDX spectra shown in Figure 5.4 indicate the presence of Ni, Co, Fe and O in the samples. The insets in Figure 5.4 show weight percentage values of the detected elements. As shown in Table 5.3, the obtained atomic percentage values of the detected elements are comparable to the expected values.

The particle size and morphology of the synthesized nanoparticles were visualized by high resolution transmission electron microscopy (HRTEM). The HRTEM images in Figure 5.5 indicate nearly spherical nanoparticles with average particle sizes of 13±3 nm and 12±3 nm for the as-prepared $x = 0.3$ and $x = 0.5$ samples respectively. These values are similar to those estimated from XRD spectra.

73
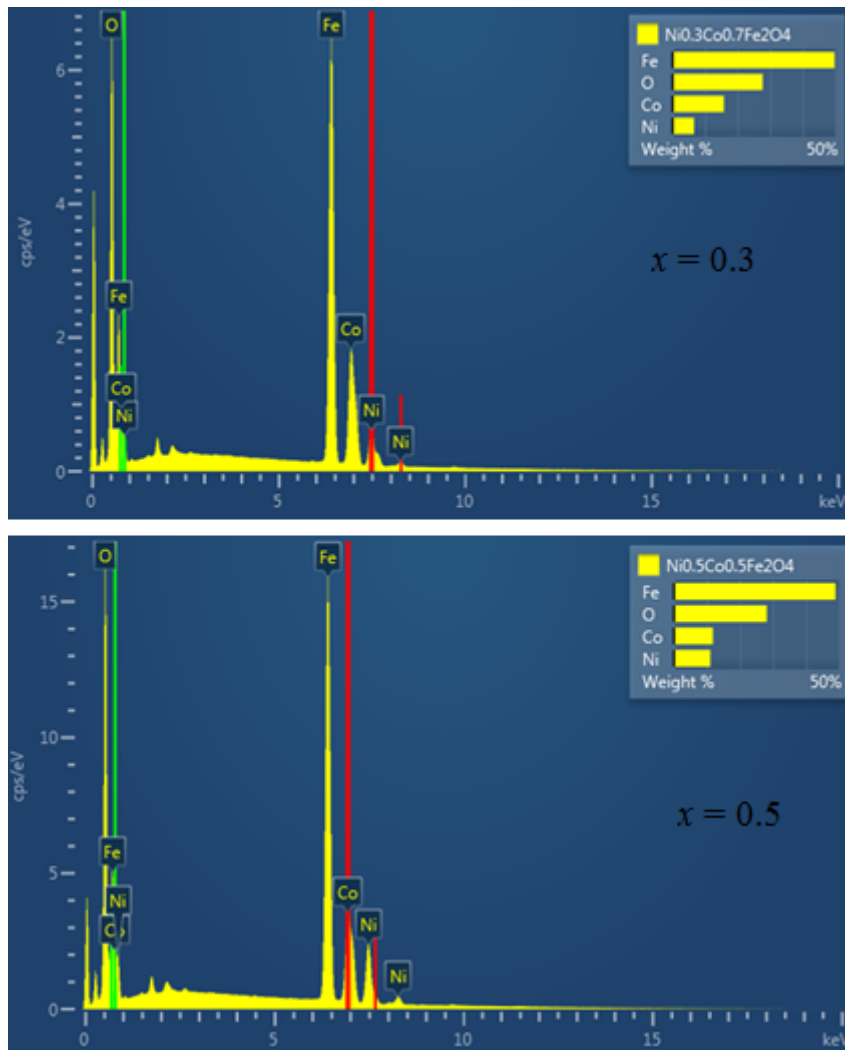
Figure 5.4: EDX measurements for the $\text{Ni}_x\text{Co}_{1-x}\text{Fe}_2\text{O}_4$ where $x = 0.3$ and 0.5.
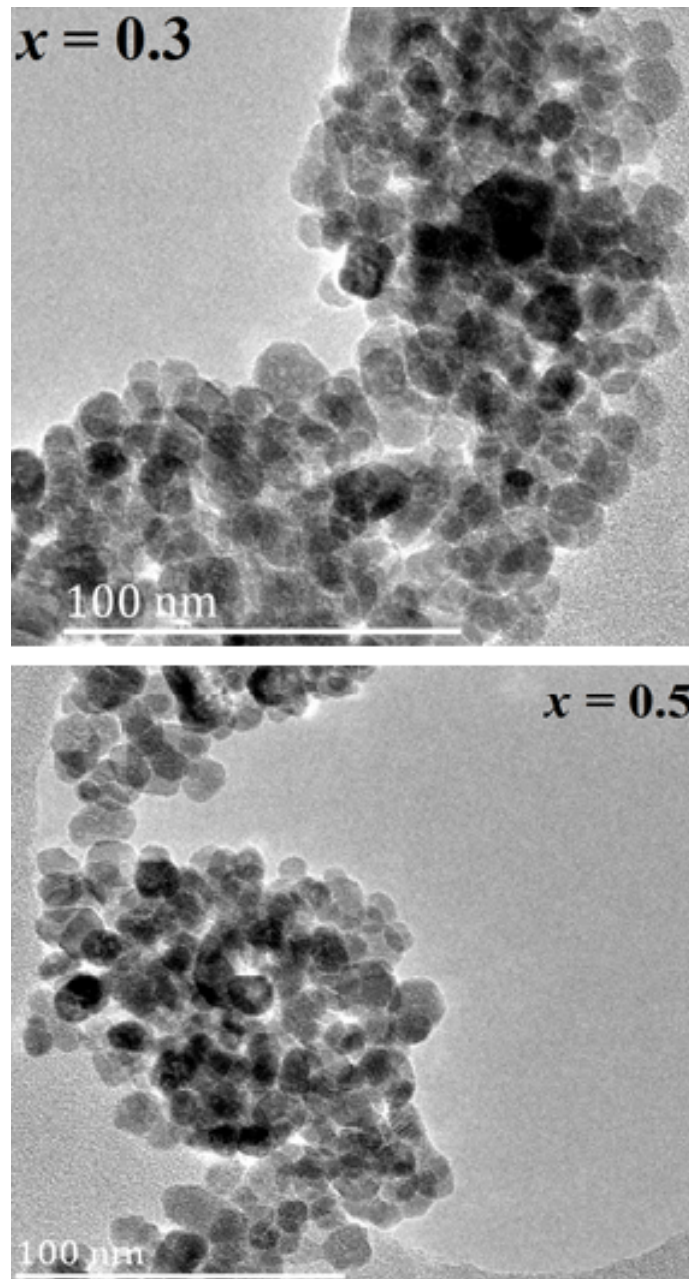
Figure 5.5: HRTEM images for the $Ni_xCo_{1-x}Fe_2O_4$ where $x = 0.3$ and 0.5.

Table 5.3: Comparison between the expected and EDX measured atomic percentages of the elements for the as-prepared $Ni_xCo_{1-x}Fe_2O_4$ ($x = 0.3, 0.5$).

Element	Expected value (%)		Measured value (%)	
	$x = 0.3$	$x = 0.5$	$x = 0.3$	$x = 0.5$
			± 0.2	± 0.2
Ni	4.3	7.1	3.8	6.2
Co	10.0	7.1	8.9	6.5
Fe	28.6	28.6	29.7	29.1
O	57.1	57.1	57.7	58.2

5.2.3 Mössbauer spectroscopy

The Mössbauer spectra of the as-prepared and annealed samples recorded at room temperature are shown in Figure 5.6. The spectra for all the samples show well-resolved Zeeman splitting which could be fitted with two sextets and one doublet. Each sextet corresponds to Fe^{3+} ions in ordered spin state distributed on tetrahedral (A) and octahedral (B) sites. A doublet is associated with a fraction of small nanoparticles in paramagnetic state. Sextets and doublets were assigned to A or B sites based on the fitted results of isomer shifts and hyperfine fields. The A site isomer shift and hyperfine fields are supposed to be lower at A site because of higher symmetry. The line widths and Fe fractions are also shown in Tables 5.4 and 5.5. There is no significant change in isomer shifts with increasing annealing temperature. The s-electron density is therefore not significantly affected by crystallite growth. Figure 5.7 and 5.8 show the variation of hyperfine fields with annealing temperature. The lower values of A-site relative to B-site hyperfine fields are due to the more covalent nature of the Fe^{3+}-O^{2-} bonds at the tetrahedral site compared to those at B site [74]. A general increase in hyperfine fields with increasing grain size is observed. We attribute the increase in hyperfine fields with increasing particle size to a decrease in relaxation rate. In a collection of interacting nanoparticles, there is

76
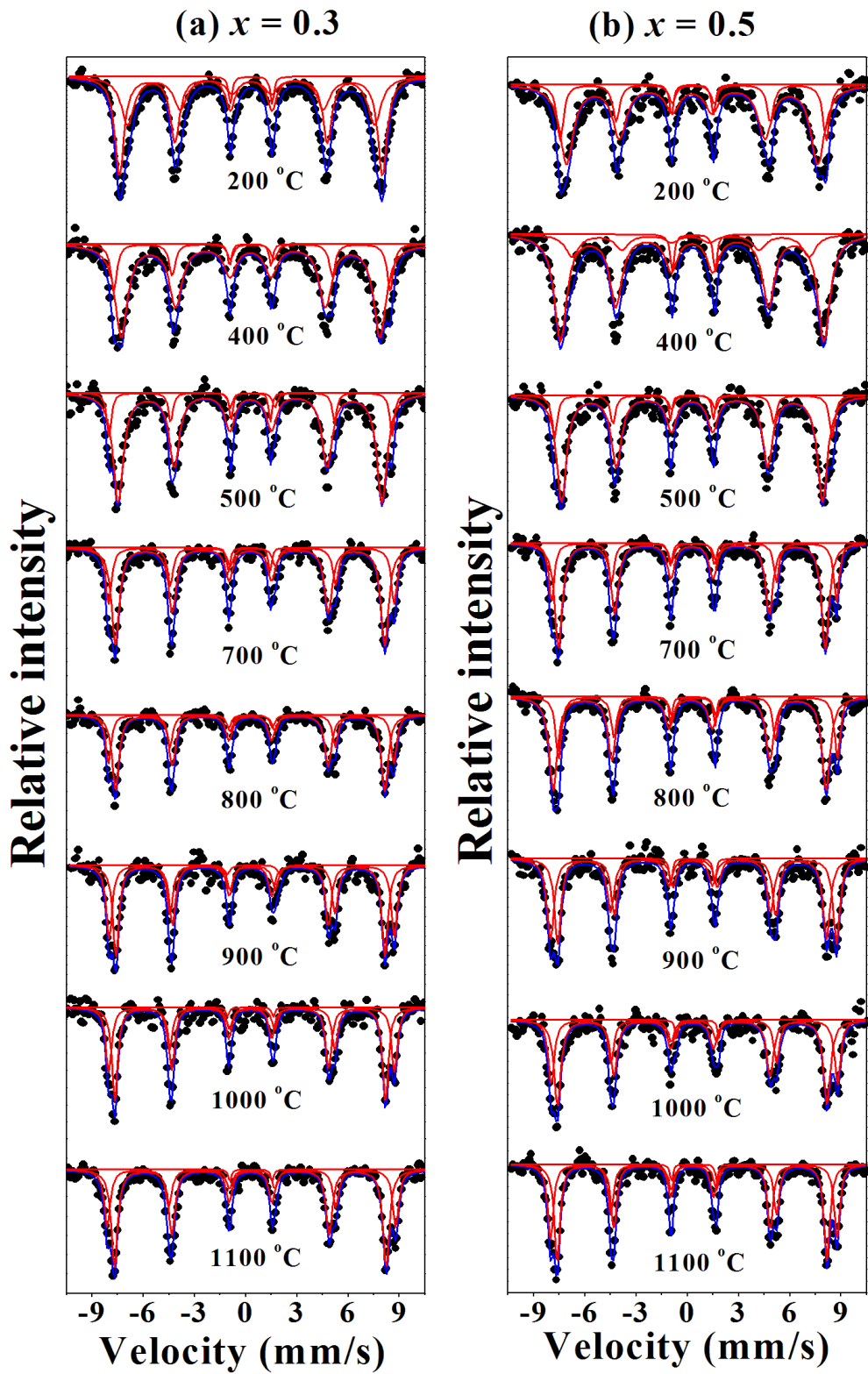
Figure 5.6: Mössbauer spectra for $Ni_xCo_{1-x}Fe_2O_4$ where $x = 0.3, 0.5$.

a relaxation of the magnetization vector of the cluster of nanoparticles bounded by magnetic dipole interaction. The relaxation rate is related to particle's volume (V) and anisotropy energy density (K) by Néel's equation [75]

$$\tau = \tau_0 \exp\left(-\frac{KV}{k_B T}\right) \qquad (5.2.1)$$

Néel's relaxation is the reorientation of the magnetic moments within the particles. The reduced values of hyperfine fields for samples with smaller crystallite sizes can also be attributed to collective excitations in small particles as explained in reference [76]. A reduction in line widths with increasing annealing temperature occurs. The A-site line widths appear to be sensitive to particle size.

Table 5.4: Variation of the isomer shift σ, hyperfine field H, line width Γ and site population f for $Ni_{0.3}Co_{0.7}Fe_2O_4$ nanoferrites at room temperature.

T	σ_A	σ_B	H_A	H_B	Γ_A	Γ_B	f_A	f_B
(°C)	(mm/s)	(mm/s)	(kOe)	(kOe)	(mm/s)	(mm/s)	(%)	(%)
	±0.03	±0.02	±3	±2	±0.03	±0.04	±0.1	±0.2
200	0.34	0.31	448	478	0.47	0.33	39.3	57.5
500	0.27	0.34	479	514	0.36	0.16	81.8	14.9
600	0.28	0.36	483	514	0.27	0.25	60.3	35.2
700	0.26	0.38	489	519	0.27	0.21	66.4	29.8
800	0.26	0.36	489	518	0.24	0.20	63.1	33.0
900	0.28	0.38	489	518	0.22	0.21	54.5	43.1
1000	0.26	0.36	491	519	0.20	0.21	57.6	40.9
1100	0.28	0.36	493	524	0.22	0.22	62.7	35.5

5.2.4 Magnetization

The hysteresis loops recorded at room temperature up to a field of 14 kOe for the annealed $Ni_xCo_{1-x}Fe_2O_4$ ($x = 0.3$, 0.5) oxides are shown in Figure 5.9. The values

Table 5.5: Variation of the isomer shift σ, hyperfine field H, line width Γ and site population f for $Ni_{0.5}Co_{0.5}Fe_2O_4$ nanoferrites at room temperature.

T (°C)	σ_A (mm/s)	σ_B (mm/s)	H_A (kOe)	H_B (kOe)	Γ_A (mm/s)	Γ_B (mm/s)	f_A (%)	f_B (%)
	±0.03	±0.02	±3	±2	±0.03	±0.04	±0.1	±0.2
200	0.28	0.34	456	483	0.49	0.24	71.4	24.6
400	0.29	0.28	430	478	0.47	0.43	18.0	77.7
500	0.19	0.35	474	504	0.35	0.19	79.9	17.2
600	0.27	0.39	482	511	0.29	0.22	68.0	28.5
700	0.26	0.39	485	517	0.27	0.19	68.7	27.6
800	0.16	0.52	496	506	0.29	0.20	65.6	30.7
900	0.13	0.51	502	506	0.25	0.23	48.6	48.1
1000	0.27	0.39	489	520	0.24	0.21	58.9	38.4
1100	0.27	0.37	490	520	0.20	0.20	55.7	41.9
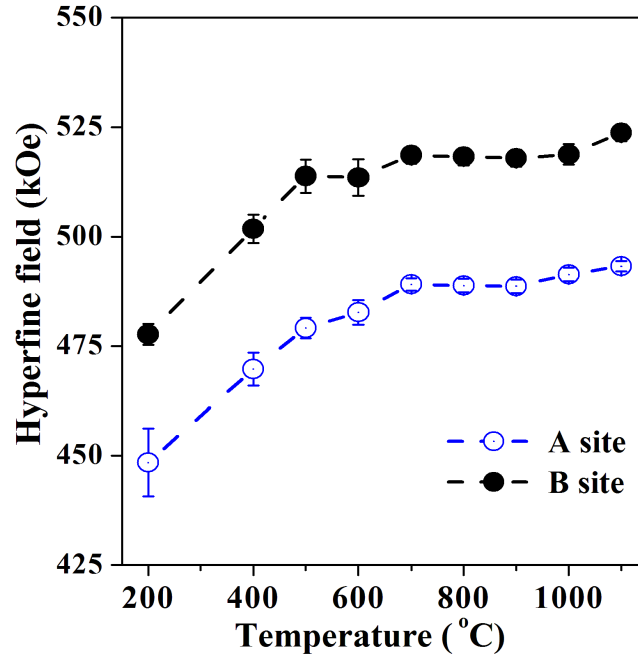
Figure 5.7: Hyperfine fields at A and B sites for $Ni_{0.3}Co_{0.7}Fe_2O_4$.
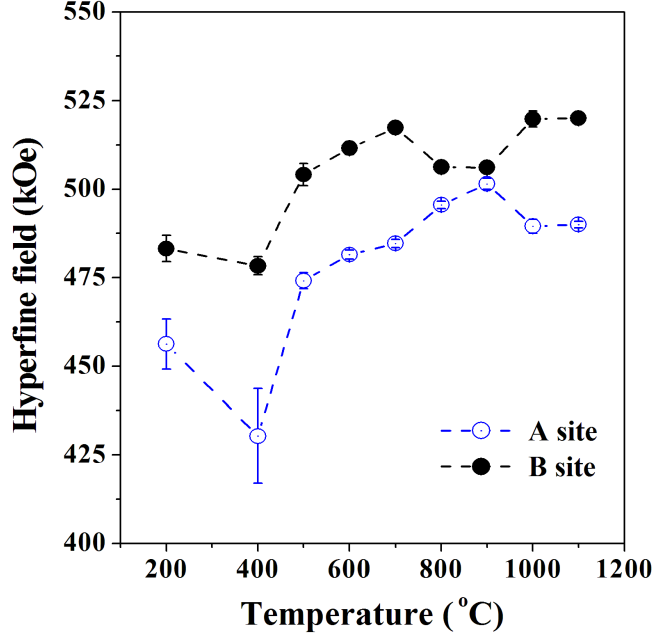
Figure 5.8: Hyperfine fields at A and B sites for $Ni_{0.5}Co_{0.5}Fe_2O_4$.

of coercive field H_c, saturation magnetization M_s and residual magnetization M_r estimated from hysteresis loops are given in Tables 5.6 and 5.7.

For $x = 0.3$, M_s increases from 30 emu/g to about 66 emu/g. This is associated with increase in crystallite size from 13 nm for the as-prepared sample to 111 nm after annealing at 1100 °C. Enhanced magnetization is indicative of stronger magnetic superexchange interaction in bulk samples. Reduced magnetization in compounds with fine powders may be due existence of spin-glass-like structures at the surface or exhibiting noncollinear spins structure or the existence of a dead layer at the surface of the nanoparticles [51, 67], that prevent the core spins to align in the magnetic field direction and thus causing reduced magnetization. Thermal annealing can also affect the distribution of metals ions between A and B sites. The net magnetization comes as a result of uncompensated magnetic moments mediated by A-B superexchange interactions.

As shown in Figure 5.10, the coercive fields for the $Ni_xCo_{1-x}Fe_2O_4$ ($x = 0.3$) oxide initially increases (from $\approx$100 Oe) and reaches to a maximum (at $\approx$1000 Oe) after annealing at 700 °C with increasing sintering temperature. H_c then reduces with further increase in the annealing temperature. A similar behavior is observed

80

(a) x = 0.3 **(b) x = 0.5**
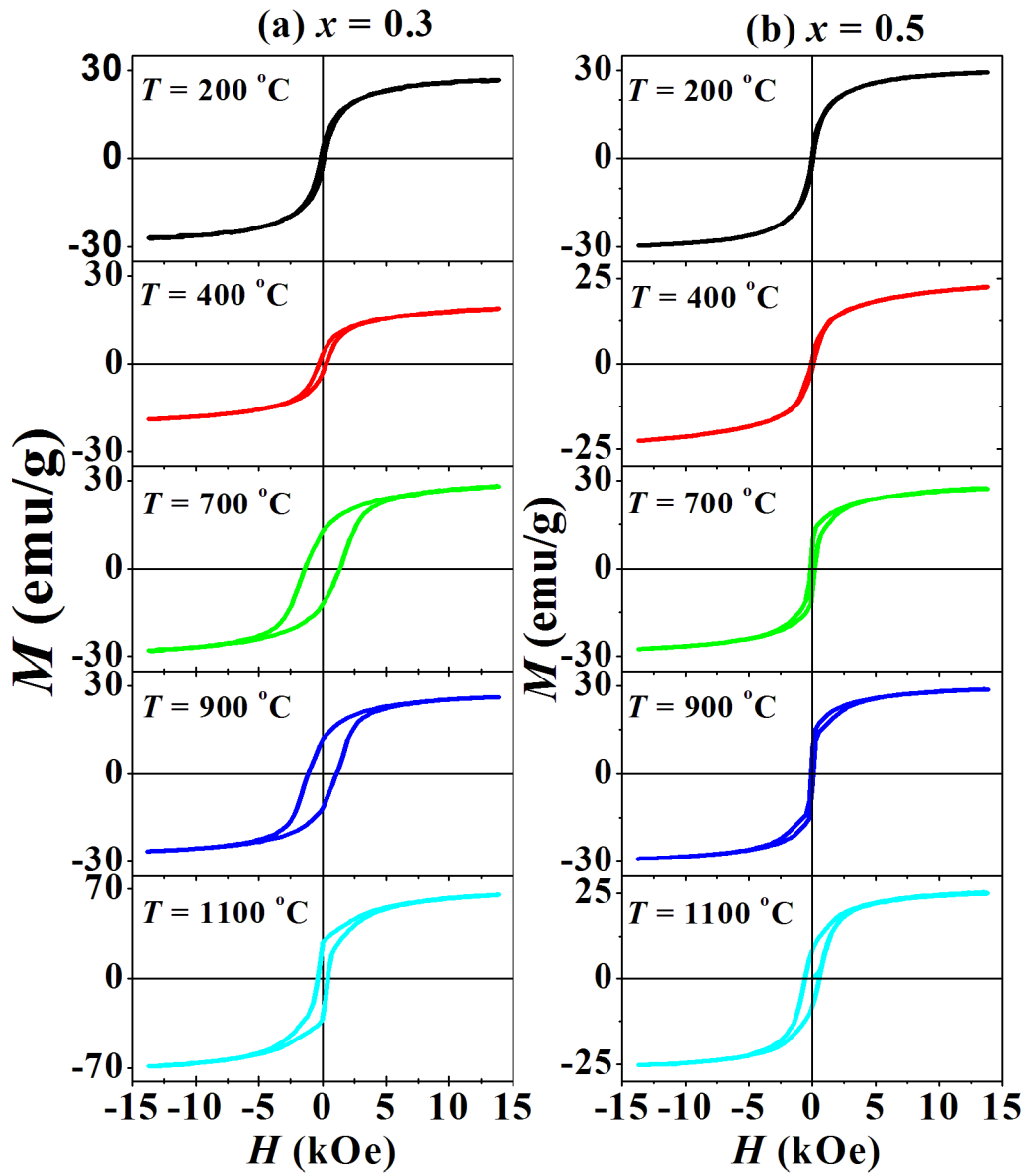
Figure 5.9: Magnetic hysteresis loops for annealed $Ni_xCo_{1-x}Fe_2O_4$ where $x = 0.3$, 0.5.

Table 5.6: Coercive field H_c, saturation magnetization M_s and remanent magnetization M_r for annealed $Ni_{0.3}Co_{0.7}Fe_2O_4$ nanoferrites with annealing temperature.

T	H_c	M_s	M_r
(°C)	(Oe)	(emu/g)	(emu/g)
	±0.01	±0.01	
200	123.54	29.74	2.8
400	265.08	18.92	3.0
500	485.19	26.64	10.2
600	896.99	26.36	9.2
700	1348.10	28.14	12.3
900	1080.02	26.22	11.6
1000	394.26	65.64	25.9
1100	392.03	65.63	5.4

Table 5.7: Coercive field H_c, saturation magnetization M_s and remanent magnetization M_r for annealed $Ni_{0.5}Co_{0.5}Fe_2O_4$ nanoferrites with temperature.

T	H_c	M_s	M_r
(°C)	(Oe)	(emu/g)	(emu/g)
	±0.01	±0.01	
200	47.63	29.40	1.3
400	88.54	22.57	1.6
500	171.88	21.93	3.0
700	155.23	27.24	8.3
800	113.09	27.90	7.4
900	85.21	28.79	6.6
1000	91.45	61.43	6.0
1100	543.21	63.47	8.1

for $x = 0.5$. This variation in H_c with crystallite growth, shown in Figure 5.11, is attributed to the effect of crossover from single- to multi-domain behavior at a critical particle size. For magnetic materials there is a threshold particle size, below which single domain structure exists. Below this critical grain size the increase in energy due to domain wall formation is higher than the reduction in the energy due to domain formation. For single-domain particles, H_c is expected to increase with increasing particle size [51, 67]. The generally higher values of coercive fields for the oxide ($x = 0.3$) with high content of Co ions have been observed.
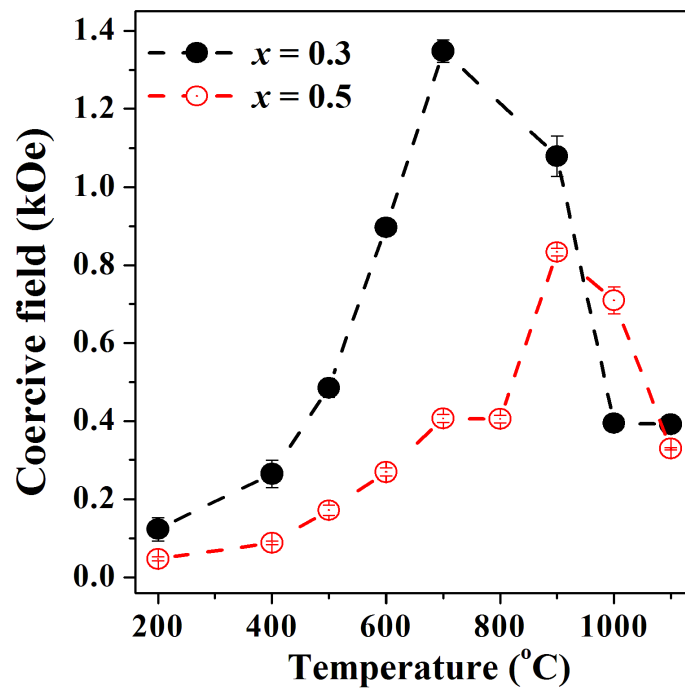
Figure 5.10: Variation of coercivity with annealing temperature for the $Ni_x Co_{1-x} Fe_2 O_4$ where $x = 0.3, 0.5$.

According to the Stoner-Wohlfarth theory, H_c is related to anisotropy constant (K_1) and saturation magnetization by [59]

$$H_c = \frac{0.98 K_1}{M_s}. \tag{5.2.2}$$

Higher coercive fields for the compound with higher concentration of Co atoms ($Ni_{0.3} Co_{0.7} Fe_2 O_4$) can be explained by high magnetocrystalline anisotropy of the Co^{2+} compared to Ni^{2+} ions [24]. For multi-domain particles the effect of increasing
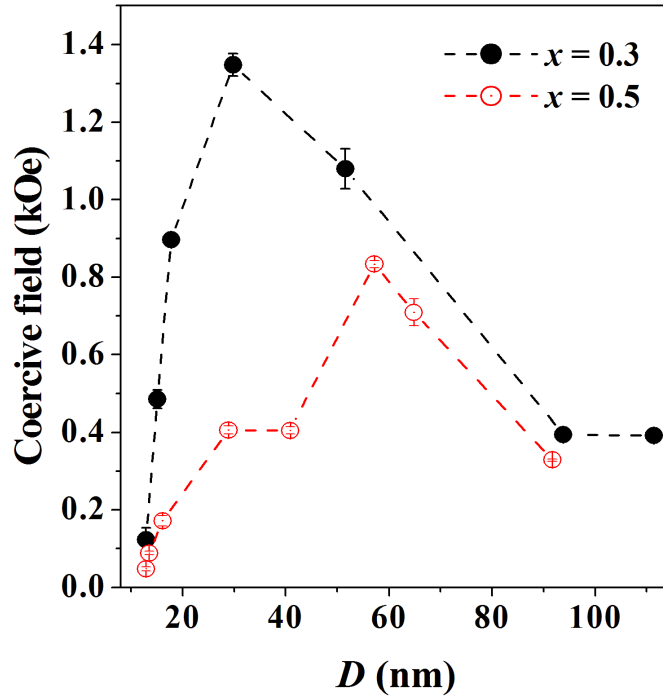
Figure 5.11: Variation of coercivity with particle size for the $Ni_xCo_{1-x}Fe_2O_4$ where $x = 0.3$, 0.5.

magnetization by increasing particle size is more prominent and H_c reduces according to Equation (5.2.2).

5.3   Conclusions

$Ni_xCo_{1-x}Fe_2O_4$ ($x = 0.3$, 0.5) nanosized compounds have been synthesized by glycol-thermal method. Thermal annealing shows significant effects on the magnetic properties. The current results show coercivity and hyperfine magnetic fields that are sensitive to particle size. The variation of coercive fields with increasing annealing temperature indicates a transition from single domain to multidomain structure at a critical crystallite size of about 30 nm for $x = 0.3$. Bulk properties emerge at the highest annealing temperatures.

Chapter 6

Properties of $Co(RE)_{0.1}Fe_{1.9}O_4$ nanoferrites

6.1   Introduction

The properties of spinel nanoferrites dependent on the cation distribution on the tetrahedral (A) and octahedral (B) sites. $CoFe_2O_4$ has a partially inverse spinel structure where the Co^{2+} ions occupy mainly the B site [3, 77]. Fe^{3+} ions are split between the A and B sites. Fe^{3+}-Fe^{3+} interactions dictate the magnetic properties in ferrites [5]. The surrounding ions may influence these interactions indirectly by shielding the Fe^{3+} ions or directly by substituting some of Fe^{3+} with different ions, such as the rare earth $(RE)^{3+}$ ions. The RE ions have been found to enhance the properties of ferrites for applications such as high-density recording, magneto-electric and biomedical sciences [55, 78, 79].

One of the limitations of incorporating the RE^{3+} ions into the spinel structure is attributed to the larger ionic radii of the RE that has been discussed in detail previously [55, 80]. Meng *et al.* [79] have studied the series $CoFe_{2-x}Y_xO_4$ and found that for $x > 0.2$, the spinel structure had some impurities formed which were said to be from the $YFeO_3$ species. Tahar *et al.* [77] have reported the magnetic properties of $CoFe_{1.9}(RE)_{0.1}O_4$ with $RE =$ La, Ce, Nd, Sm, Eu, Gd, Tb and Ho. The blocking temperatures of the superparamagnetic particles were found to decrease on substitution with the RE ions. The magnetic behaviour of the particles were found

to correlate well with their particle size. Reduction of magnetic properties has been observed on rare earth substitution due to the dilution of magnetic (Fe^{3+}-Fe^{3+}) interaction [5, 55]. The study of $CoFe_{2-x}Gd_xO_4$ where $x = 0.0$, 0.1, 0.3, 0.5 by Zhao *et al.* found that the coercivity and saturation magnetization decrease with x. Adsorption capabilities of the nanoferrites for dyes was also found to improve.

In this chapter we have studied the structural, magnetic and electrical properties of $Co(RE)_{0.1}Fe_{1.9}O_4$ (RE = Ce, Nd, Sm, Gd, Dy, Er and Yb) nanoferrites synthesized by the glycol-thermal technique. Characterization of the samples was performed by X-ray diffraction (XRD), high-resolution transmission electron microscopy (HRTEM), ^{57}Fe Mössbauer spectroscopy, vibrating sample magnetometer (VSM) and by the four probe resistivity measurement method.

6.2 Results and discussion

6.2.1 X-ray diffraction

Figure 6.1 shows the XRD patterns of the powdered samples of $Co(RE)_{0.1}Fe_{1.9}O_4$ nanoferrites. Single phase cubic spinel structured samples were produced with no significant phase impurities. The HRTEM images, measured at 100 nm, for samples of RE = Ce, Nd and Er are shown in Figure 6.2. These samples seem to have spherical particles.

Table 6.1 shows the particle size D, HRTEM particle diameter D_{TEM}, lattice parameter a, XRD desity ρ_{XRD} as well as the synthesis pressure P inside the reactor during the glycol-thermal reaction process. The particle sizes were calculated from the full width at half range maximum of the most intense XRD peak (311) by the Scherrer Equation (3.3.4). The crystallite size range from 8.36 nm to 13.72 nm which confirms the nano-range of the particle sizes. The HRTEM particle diameters D_{TEM} that were estimated directly from the HRTEM images are in agreement with XRD particle sizes for the measured samples. Figure 6.3 shows the variation of crystallite size with the RE substitution. The particle size seem to have a high correlation with the reaction pressure (i.e. bigger particles for high pressures) [53]. This is confirmed by the plot of D versus P in Figure 6.4 which has a correlation coefficient
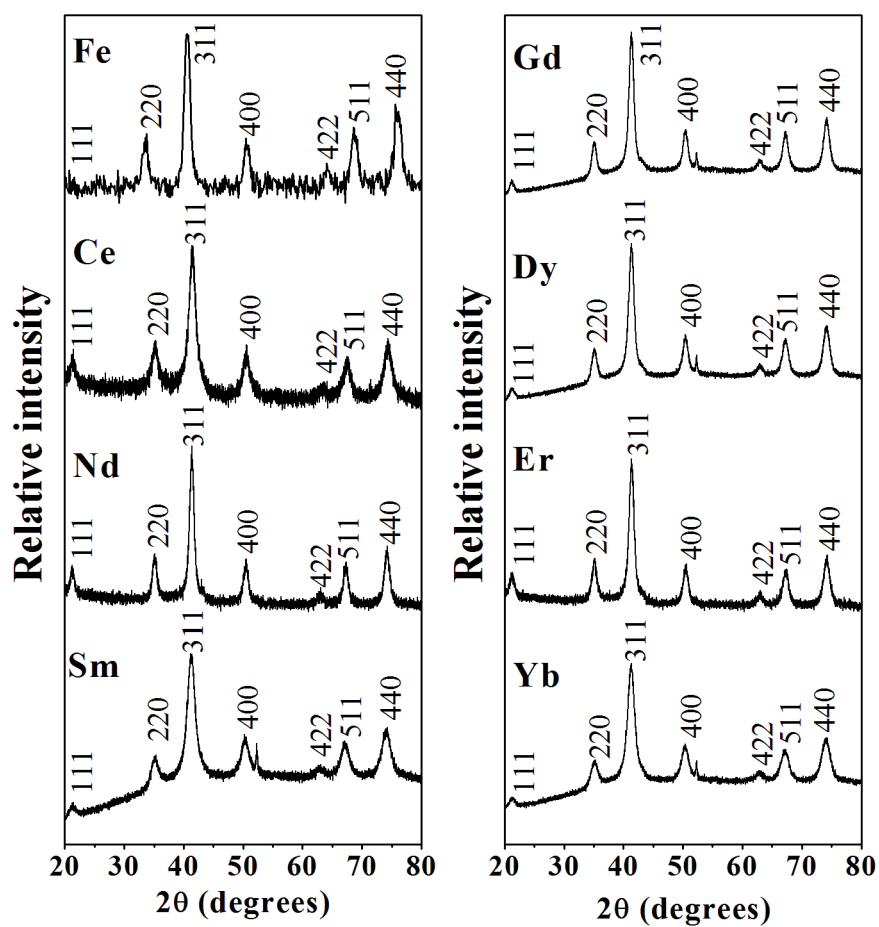
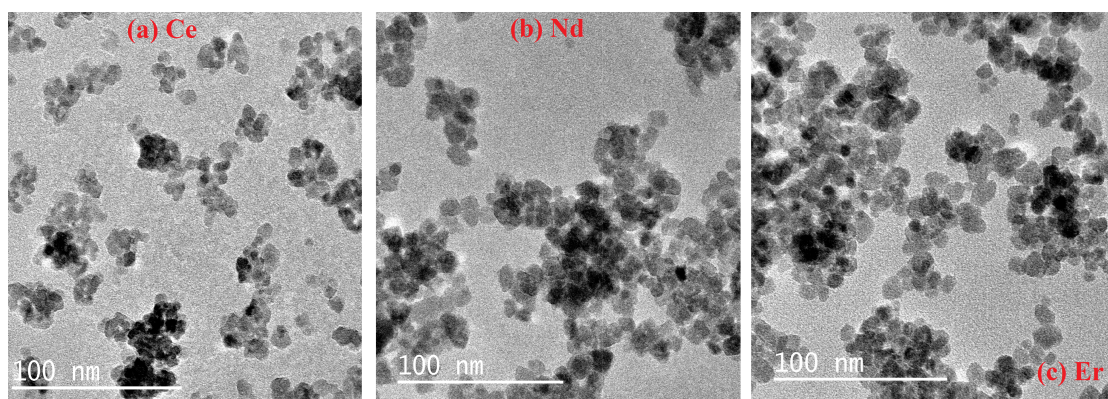Figure 6.1: XRD patterns for the $Co(RE)_{0.1}Fe_{1.9}O_4$ nanoferrites.

Figure 6.2: HRTEM images for $Co(RE)_{0.1}Fe_{1.9}O_4$ ($RE = $ (a) Ce, (b) Nd, (c) Er) nanoferrites.

Table 6.1: Sample preparation pressure P, crystallite size D, lattice parameter a and XRD density ρ_{XRD} for the $Co(RE)_{0.1}Fe_{1.9}O_4$ nanoferrites.

RE	P (psi)	D (nm)	D_{TEM} (nm)	a (Å)	ρ_{XRD} (g/cm^3)
		±0.06	±3	±0.005	±0.01
Fe	70	10.90	–	8.386	5.28
Ce	60	9.46	9	8.377	5.49
Nd	70	13.72	14	8.396	5.47
Sm	30	8.36	–	8.403	5.46
Gd	70	12.67	–	8.397	5.49
Dy	60	11.37	–	8.395	5.51
Er	60	12.33	12	8.394	5.52
Yb	40	9.08	–	8.402	5.52

of 0.81173.

The variation of the lattice parameter, calculated by Equation (3.3.3), is shown in Figure 6.5. The increase of a in allsamples is evident, except for the Ce sample which has a smaller a than for $CoFe_2O_4$. We attribute this increase to the substitution of Fe^{3+} ions by the larger RE^{3+} ions [5, 55, 77]. The value of a for $Co(RE)_{0.1}Fe_{1.9}O_4$ (RE = Fe, Ce, Nd, Sm and Gd) samples are close to previously reported values [5, 77].

The XRD density was calculated from the lattice parameter by Equation (3.3.6). Figure 6.6 shows the variation of the XRD density with the RE substitution. The XRD density increases with the increasing RE $4f$ electrons. A similar behaviour has been reported previously [5].

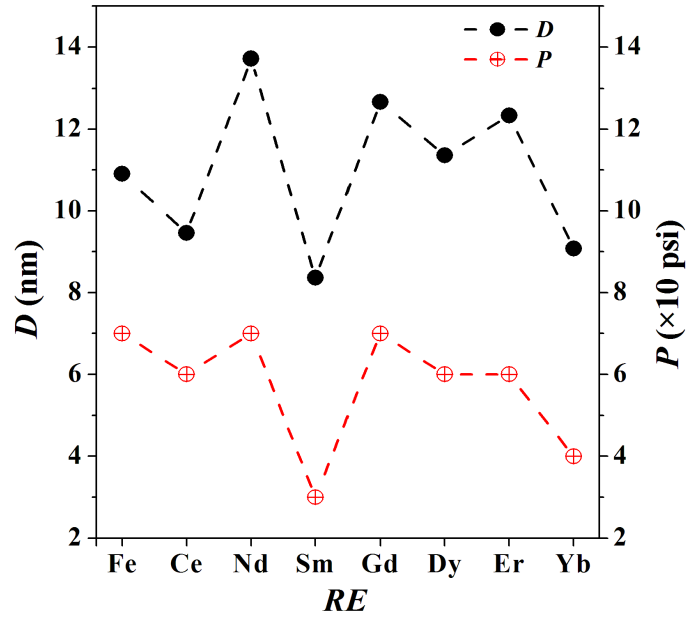Figure 6.3: Variation of the particle sizes and synthesis pressure with RE for $Co(RE)_{0.1}Fe_{1.9}O_4$ nanoferrites.
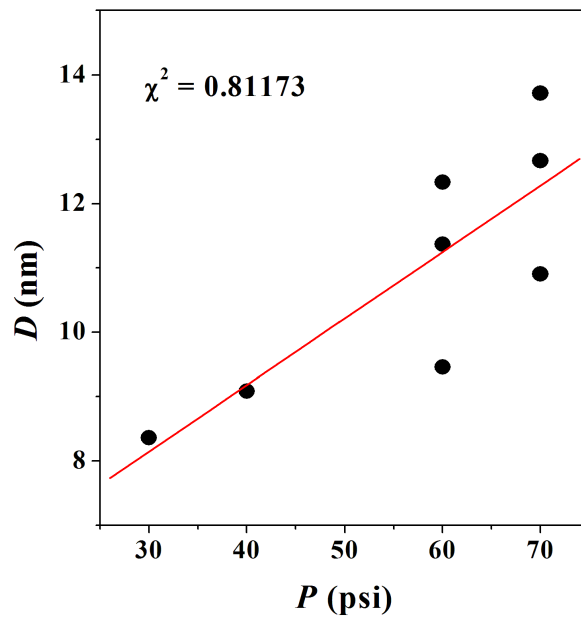
Figure 6.4: The correlation between particle size D and synthesis pressure P for $Co(RE)_{0.1}Fe_{1.9}O_4$ nanoferrites.
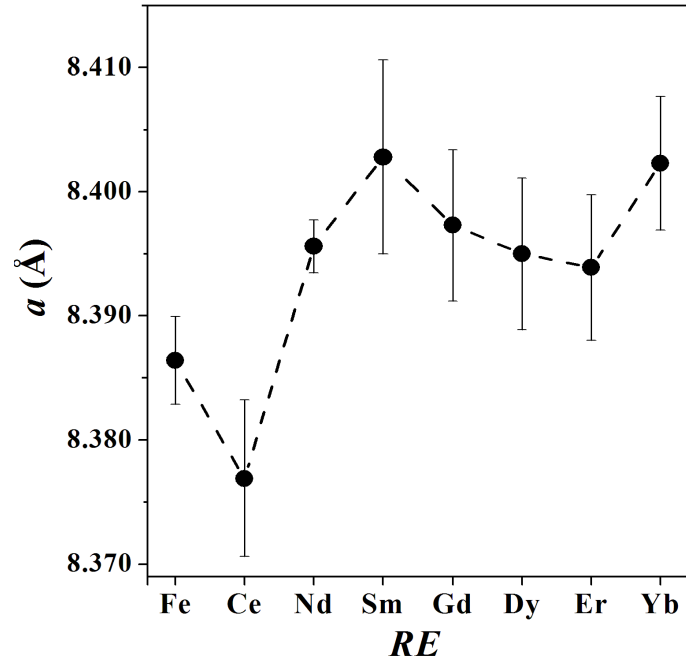
Figure 6.5: Lattice parameter for $Co(RE)_{0.1}Fe_{1.9}O_4$ nanoferrites.
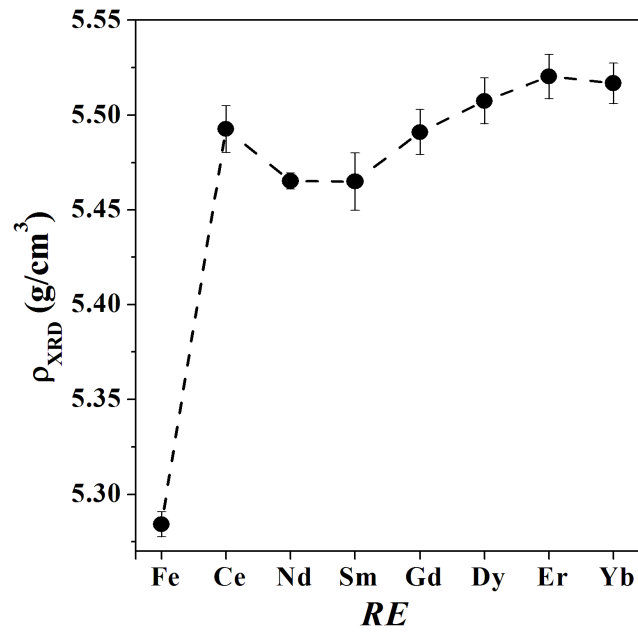
Figure 6.6: X-ray density ρ_{XRD} for $Co(RE)_{0.1}Fe_{1.9}O_4$ nanoferrites.

6.2.2 Mössbauer spectroscopy

The ^{57}Fe Mössbauer spectra were analyzed using the Recoil Mössbauer analysis software. The Mössbauer spectra for the $Co(RE)_{0.1}Fe_{1.9}O_4$ nanoferrites recorded at room temperature are shown in Figure 6.7. The spectra were fitted with two sextets and one doublet. The sextets correspond to the magnetically ordered Fe^{3+} ions on the A and B sites. The doublet accounts for the Fe^{3+} ions in a paramagnetic state. Well resolved Zeeman splitting is observed for the RE = Nd, Gd, Dy and Er nanoparticles. The RE = Ce, Sm and Yb nanoparticles show increased doublet areas which means enhanced magnetic disorder. The spectra reveal ferrimagnetic states for the nanoparticles. The Mössbauer parameters are shown in Table 6.2.
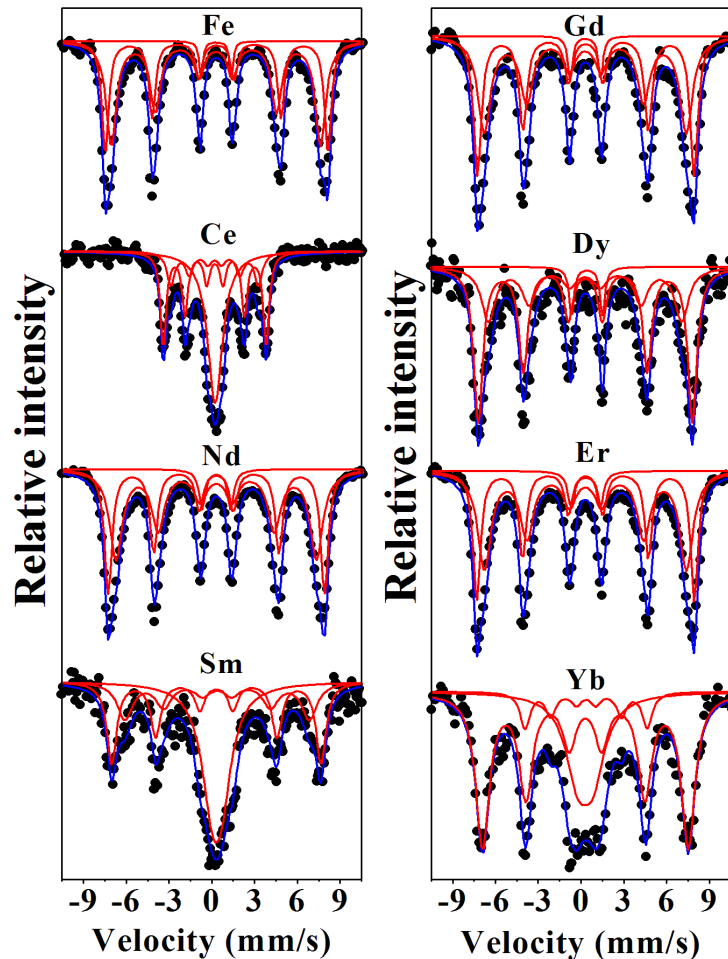
Figure 6.7: Mössbauer spectra for $Co(RE)_{0.1}Fe_{1.9}O_4$ nanoferrites.

Not much changes in the isomer shifts are observed with the substitution of Fe^{3+}

with RE^{3+}. The line widths also do not change that much and the hyperfine fields seem to correlate well with the particle sizes.

Table 6.2: Variation of the isomer shift σ, hyperfine field H, line width Γ and site population f for $Co(RE)_{0.1}Fe_{1.9}O_4$ nanoferrites at room temperature.

| RE	σ_A (mm/s)	σ_B (mm/s)	H_A (kOe)	H_B (kOe)	Γ_A (mm/s)	Γ_B (mm/s)	f_A (%)	f_B (%)
	± 0.06	± 0.02	± 7	± 2	± 0.07	± 0.05	± 7	± 6
Fe	0.28	0.33	455	484	0.43	0.28	57	40
Ce	0.20	0.21	190	223	0.33	0.25	19	40
Nd	0.31	0.32	436	470	0.54	0.32	52	42
Sm	0.37	0.32	401	455	0.65	0.42	24	34
Gd	0.29	0.32	439	471	0.54	0.33	51	45
Dy	0.28	0.30	420	465	0.58	0.39	32	62
Er	0.30	0.31	439	473	0.56	0.31	54	40
Yb	0.36	0.30	266	447	0.40	0.58	10	63

Figure 6.8 shows the variation of the hyperfine fields on the A and B sites with the RE^{3+} substitution in $Co(RE)_{0.1}Fe_{1.9}O_4$. The decrease in the hyperfine fields of the RE substituted nanoparticles may be attributed to the weakening of the superexchange interaction as a result of RE substitution [55].

6.2.3 Magnetization

The magnetization measurements were performed on a vibrating sample magnetometer (VSM). Figure 6.9 shows the magnetic hysteresis loops for the $Co(RE)_{0.1}Fe_{1.9}O_4$ nanoferrites in the applied field -14 kOe$\leq H \leq$14 kOe. Not much coercivity can be observed from the loops which is typical of superparamagnetism in nanoparticles [55]. At maximum applied field $H = 14$ kOe, the magnetization M of the samples is not saturated. The coercive field H_c, magnetization M at the highest field
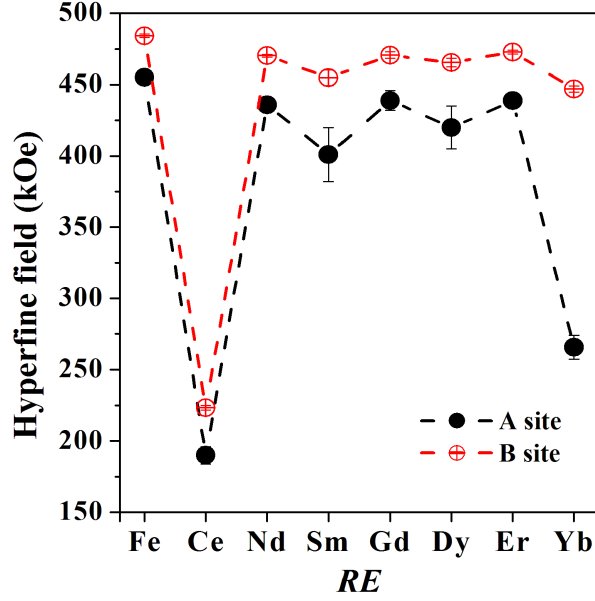
Figure 6.8: Hyperfine fields at A and B sites for $Co(RE)_{0.1}Fe_{1.9}O_4$ nanoferrites.

and remanent magnetization M_r which were deduced from the hysteresis curves for $Co(RE)_{0.1}Fe_{1.9}O_4$ nanoferrites, are shown in Table 6.3. The table also includes the synthesis pressure P and the particle sizes D from Table 6.1.

Figure 6.10 shows the variation of coercivity and the crystallite sizes with the RE substitution. The coercivity decreases for the RE substituted nanoparticles due to the weakening of the superexchange interaction. Moreover the coercivity can be seen to correlate well with the particle sizes which is confirmed in Figure 6.11 with a correlation of 0.98423 (this correlation excludes pure $CoFe_2O_4$).

6.2.4 Electrical resistivity

The electrical resistivity measurements at temperatures 25 °C$\leq T \leq$130 °C were done by the four probe method. Some of the measured samples did not show any conductivity. The resistivity was assumed to vary according to Arrhenius Equation (3.6.3). Figures 6.12 and 6.13 show the plots of $\ln \rho$ against T^{-1} for $Co(RE)_{0.1}Fe_{1.9}O_4$ (RE = Nd, Sm) nanoferrites. The different faces of the same pellet show different slopes which translates to different energy gaps (activation energy). This behaviour for the pellets has been reported by Abdallah *et al.* [17]. The conduction
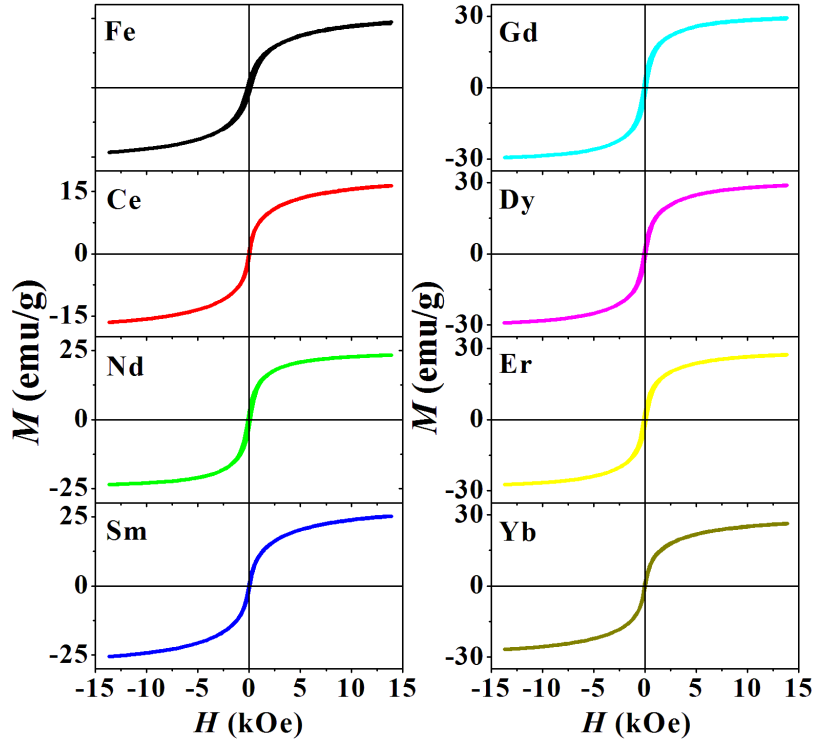
Figure 6.9: Magnetic hysteresis loops of the $Co(RE)_{0.1}Fe_{1.9}O_4$ nanoferrites.

Table 6.3: Coercive field H_c, magnetization M and remanent magnetization M_r for $Co(RE)_{0.1}Fe_{1.9}O_4$ nanoferrites.

RE	H_c	M	M_r	P	D
	(Oe)	(emu/g)	(emu/g)	(psi)	(nm)
Fe	147.7	23.4	1.95	70	10.90
Ce	27.1	16.5	0.42	60	9.46
Nd	93.6	23.4	2.16	70	13.72
Sm	15.8	25.4	0.31	30	8.36
Gd	92.2	29.3	2.56	70	12.67
Dy	66.1	29.0	1.78	60	11.37
Er	82.0	27.4	2.11	60	12.33
Yb	16.7	26.5	0.40	40	9.08
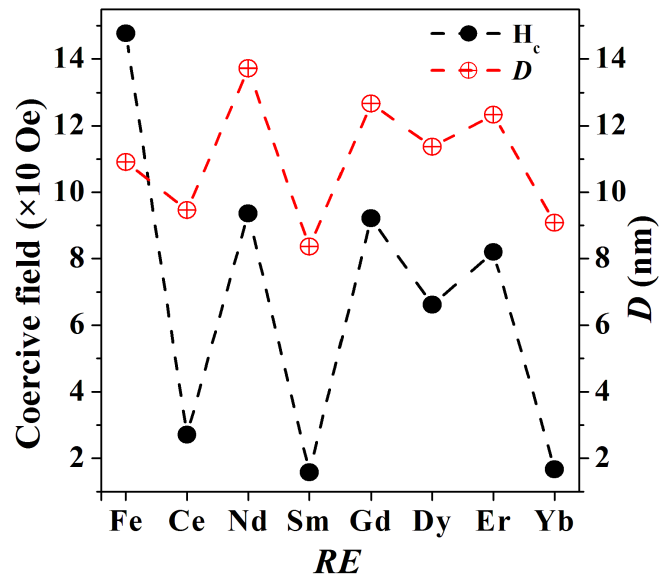
Figure 6.10: Coercive fields of the $Co(RE)_{0.1}Fe_{1.9}O_4$ nanoferrites.
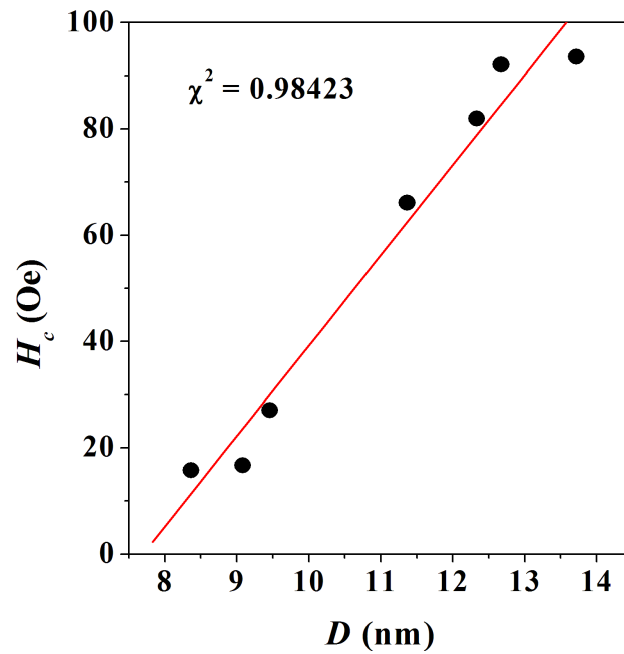
Figure 6.11: Correlation between coercive fields H_c and particle sizes D of the $Co(RE)_{0.1}Fe_{1.9}O_4$ nanoferrites.
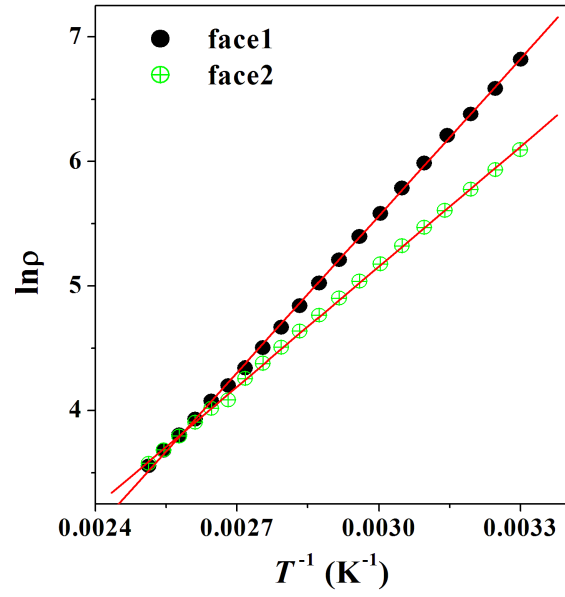
Figure 6.12: Graphical representation of $\ln \rho$ against T^{-1} for $CoNd_{0.1}Fe_{1.9}O_4$.
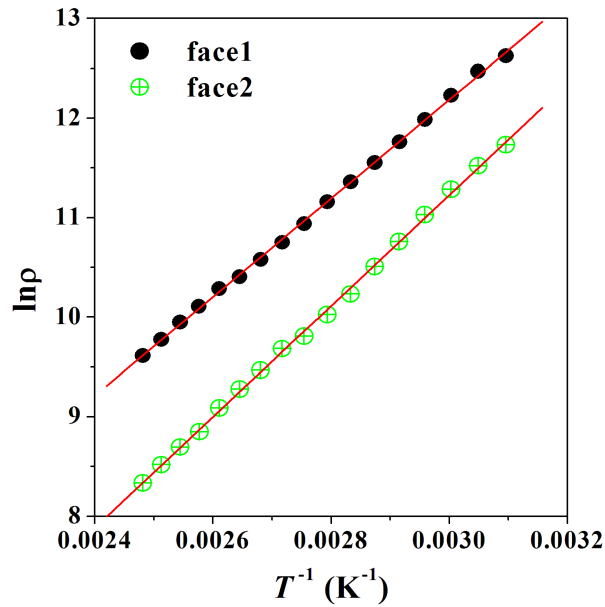
Figure 6.13: Graphical representation of $\ln \rho$ against T^{-1} for $CoSm_{0.1}Fe_{1.9}O_4$.

in these pellets may have been between the divalent (Co^{2+}) and the trivalent (Co^{3+}, Fe^{3+}) ions. The measured activation energies and resistivity extrapolated to 0 K for $Co(RE)_{0.1}Fe_{1.9}O_4$ (RE = Nd, Sm) are shown in Table 6.4 which we relate to semiconducting behaviour.

Table 6.4: Activation energy E_{a1} and resistivity at 0 K ρ_{01}(face 1), E_{a2} and ρ_{02} (face 2) for $Co(RE)_{0.1}Fe_{1.9}O_4$ (RE = Nd, Sm).

RE	E_{a1} (eV)	ρ_{01} ($\Omega\,m$)	E_{a2} (eV)	ρ_{02} ($\Omega\,m$)
	±0.002	±0.0006	±0.002	±0.0006
Nd	0.362	0.0009	0.277	0.0112
Sm	0.427	0.0683	0.480	0.0041

6.3 Conclusions

We have successfully prepared $Co(RE)_{0.1}Fe_{1.9}O_4$ (RE = Ce, Nd, Sm, Gd, Dy, Er and Yb) nanoferrites by a glycol-thermal technique. The crystallite size range from 8.36 nm to 13.72 nm. HRTEM results also confirm XRD results for the measured samples. There is an increase of the lattice parameter on substitution of Fe^{3+} by the larger radii RE^{3+} ions. Room temperature Mössbauer spectra show ferrimagnetic behaviour for the nanoparticles. A decrease in hyperfine fields on substitution of the Fe^{3+} by non-magnetic RE^{3+} ions is evidence of the weakening superexchange interaction. The lowest hyperfine fields and isomer shifts are observed for RE = Ce. Magnetization measurements through the hysteresis loops reveal superparamagnetic behaviour of the nanoparticles which was also confirmed by Mössbauer analysis. The samples do not reach saturation magnetization at the highest applied field. There is a strong correlation between coercivity and crystallite size. Electrical resistivity measurements reveal a semiconducting behaviour for the studied pellets. Differences in the electrical properties of the two faces of a pellet are also observed.

Chapter 7

General conclusions

We have studied the structural, magnetic and electrical properties of $Ni_xCo_{1-x}Fe_2O_4$ ($x = 0.0$ to 1.0 incremented by 0.1) nanoferrites synthesized by the glycol-thermal technique. Single phase formation was achieved for $x = 0.0$ to 0.6 and 1.0. Impurity peaks were observed for $x = 0.7$ to 0.9 nanoferrites. The crystallite sizes range from 7.85 nm to 13.62 nm. Room temperature ^{57}Fe Mössbauer analysis reveals ferrimagnetic behaviour for the nanoparticles. Paramagnetic behaviour was observed for $x = 0.7$ to 0.9 nanoferrites at room temperature. Well resolved Mössbauer spectra at 80 K for $x = 0.1$, 0.5, 0.7 and 0.9 nanoparticles reveal more enhanced hyperfine parameters which we associate with increased magnetic order. Mössbauer measurements against temperature for the sample with $x = 0.1$ from 80 K to 483 K reveal a magnetic transition from ferrimagnetism to paramagnetism at 473 K $\leq T \leq 483$ K. Magnetization measurements confirm superparamagnetism of the nanoparticles. Strong correlation between the coercive fields, hyperfine fields and crystallite sizes have also been observed.

Thermal annealing of $x = 0.3$, 0.5 nanoparticles shows significant effects on the magnetic properties. The current results show coercive fields and hyperfine fields which are sensitive to crystallite size. The variation of coercivity with increasing annealing temperature show evidence of a transition from single to multidomain structure at a critical particle size of about 30 nm for $x = 0.3$ and bulk properties emerge at the highest annealing temperatures.

The $Co(RE)_{0.1}Fe_{1.9}O_4$ (RE = Ce, Nd, Sm, Gd, Dy, Er and Yb) nanoferrites have

also been prepared by the glycol-thermal technique. The crystallite sizes range from 8.36 nm to 13.72 nm. The lattice parameter is increased due to the substitution of Fe^{3+} by the larger radii RE^{3+} ions. Room temperature Mössbauer spectra show ferrimagnetic behaviour of the nanoparticles. A decrease in the hyperfine fields is attributed to the weakening of the superexchange interaction. Magnetization measurements confirmed superparamagnetism of the nanoparticles. Strong correlation between the coercivity and the crystallite sizes was also observed. Preliminary results of resistivity measurements have demonstrated semiconducting behaviour in both $Ni_xCo_{1-x}Fe_2O_4$ and $Co(RE)_{0.1}Fe_{1.9}O_4$.

We have demonstrated the critical role of the sample synthesis conditions on the properties of the nanoferrite oxides studied here. In particular, we have demonstrated a close connection between the crystallite size and magnetic properties with synthesis pressure inside the reactor vessel. This is a key finding that has important implications in the synthesis of materials with particular crystallite sizes and reproducible properties.

Bibliography

[1] Daliya S Mathew and Ruey-Shin Juang. An overview of the structure and magnetism of spinel ferrite nanoparticles and their synthesis in microemulsions. *Chemical Engineering Journal*, 129(1):51–65, 2007.

[2] Patrick Masina, Thomas Moyo, and Hafiz MI Abdallah. Synthesis, structural and magnetic properties of $Zn_xMg_{1-x}Fe_2O_4$ nanoferrites. *Journal of Magnetism and Magnetic Materials*, 381:41–49, 2015.

[3] Won-Ok Choi, Jae-Gwang Lee, Byung-Sub Kang, and Kwang Pyo Chae. Crystallographic and magnetic properties of nano-sized nickel substituted cobalt ferrites synthesized by the sol-gel method. *Journal of Magnetics*, 19(1):59–63, 2014.

[4] `http://www.slideshare.net/icaer2013/291-sarita`. Accessed: 2016-08-21.

[5] AK Nikumbh, RA Pawar, DV Nighot, GS Gugale, MD Sangale, MB Khanvilkar, and AV Nagawade. Structural, electrical, magnetic and dielectric properties of rare-earth substituted cobalt ferrites nanoparticles synthesized by the co-precipitation method. *Journal of Magnetism and Magnetic Materials*, 355:201–209, 2014.

[6] Dong-Hwang Chen and Xin-Rong He. Synthesis of nickel ferrite nanoparticles by sol-gel method. *Materials Research Bulletin*, 36(7):1369–1377, 2001.

[7] K Maaz, Arif Mumtaz, SK Hasanain, and Abdullah Ceylan. Synthesis and magnetic properties of cobalt ferrite ($CoFe_2O_4$) nanoparticles prepared by wet chemical route. *Journal of Magnetism and Magnetic Materials*, 308(2):289–295, 2007.

[8] A Tavakoli, M Sohrabi, and A Kargari. A review of methods for synthesis of nanostructured metals with emphasis on iron compounds. *Chemical Papers*, 61 (3):151–170, 2007.

[9] Hafiz MI Abdallah and Thomas Moyo. Structural and magnetic studies of $(Mg, Sr)_{0.2}Mn_{0.1}Co_{0.7}Fe_2O_4$ nanoferrites. *Journal of Alloys and Compounds*, 562:156–163, 2013.

[10] JZ Msomi, HMI Abdallah, T Moyo, and A Lančok. Structural and magnetic properties of $Mn_xCo_{1-x}Fe_2O_4$ ferrite nanoparticles. *Journal of Magnetism and Magnetic Materials*, 323(5):471–474, 2011.

[11] Dong-Sik Bae, Sang-Woo Kim, Hae-Weon Lee, and Kyong-Sop Han. Synthesis and characterization of nanosize $Co_xNi_{1-x}Fe_2O_4$ powders by glycothermal process. *Materials Letters*, 57(13):1997–2000, 2003.

[12] Sonal Singhal, J Singh, SK Barthwal, and K Chandra. Preparation and characterization of nanosize nickel-substituted cobalt ferrites $(Co_{1-x}Ni_xFe_2O_4)$. *Journal of Solid State Chemistry*, 178(10):3183–3189, 2005.

[13] CN Chinnasamy, A Narayanasamy, N Ponpandian, K Chattopadhyay, K Shinoda, B Jeyadevan, K Tohji, K Nakatsuka, T Furubayashi, and I Nakatani. Mixed spinel structure in nanocrystalline $NiFe_2O_4$. *Physical Review B*, 63(18): 184108, 2001.

[14] G Ravi Kumar, K Vijaya Kumar, and YC Venudhar. Electrical conductivity and dielectric properties of copper doped nickel ferrites prepared by double sintering method. *International Journal of Modern Engineering Research*, 2(2): 177–185, 2012.

[15] IH Gul, AZ Abbasi, F Amin, M Anis-ur Rehman, and A Maqsood. Structural, magnetic and electrical properties of $Co_{1-x}Zn_xFe_2O_4$ synthesized by co-precipitation method. *Journal of Magnetism and Magnetic Materials*, 311(2): 494–499, 2007.

[16] IH Gul and A Maqsood. Structural, magnetic and electrical properties of cobalt ferrites prepared by the sol–gel route. *Journal of Alloys and Compounds*, 465 (1):227–231, 2008.

[17] HMI Abdallah, T Moyo, and JZ Msomi. Mössbauer and electrical studies of $Mn_xCo_{1-x}Fe_2O_4$ compounds prepared via glycothermal route. *Journal of superconductivity and novel magnetism*, 24(1-2):669–673, 2011.

[18] Hafiz MI Abdallah and Thomas Moyo. Electrical properties of $Mn_{0.5}Co_{0.5}Fe_2O_4$ nanoparticle synthesized via high-energy milling technique.

[19] F Einar Kruis, Heinz Fissan, and Aaron Peled. Synthesis of nanoparticles in the gas phase for electronic, optical and magnetic applications: a review. *Journal of Aerosol Science*, 29(5):511–535, 1998.

[20] SA Saafan, TM Meaz, EH El-Ghazzawy, MK El Nimr, MM Ayad, and M Bakr. AC and DC conductivity of nizn ferrite nanoparticles in wet and dry conditions. *Journal of Magnetism and Magnetic Materials*, 322(16):2369–2374, 2010.

[21] Quentin A Pankhurst, J Connolly, Stephen K Jones, and JJ Dobson. Applications of magnetic nanoparticles in biomedicine. *Journal of physics D: Applied physics*, 36(13):R167, 2003.

[22] Ibrahim Sharifi, H Shokrollahi, and S Amiri. Ferrite-based magnetic nanofluids used in hyperthermia applications. *Journal of Magnetism and Magnetic Materials*, 324(6):903–915, 2012.

[23] S Amiri and H Shokrollahi. The role of cobalt ferrite magnetic nanoparticles in medical science. *Materials Science and Engineering: C*, 33(1):1–8, 2013.

[24] M Mozaffari, J Amighian, and E Darsheshdar. Magnetic and structural studies of nickel-substituted cobalt ferrite nanoparticles, synthesized by the sol–gel method. *Journal of Magnetism and Magnetic Materials*, 350:19–22, 2014.

[25] RC Kambale, PA Shaikh, SS Kamble, and YD Kolekar. Effect of cobalt substitution on structural, magnetic and electric properties of nickel ferrite. *Journal of Alloys and Compounds*, 478(1):599–603, 2009.

[26] John M D Coey. *Magnetism and magnetic materials*. Cambridge University Press, 2010.

[27] `http://images.slideplayer.com/19/5756281/slides/slide_43.jpg`. Accessed: 2016-06-01.

[28] Charles Kittel. *Introduction to solid state physics*. Wiley, 2005.

[29] `https://global.britannica.com/science/ferromagnetism`. Accessed: 2016-07-15.

[30] David Jiles. *Introduction to magnetism and magnetic materials*. CRC press, 1991.

[31] M Benz. Superparamagnetism: theory and applications. *Discussion*, 2012.

[32] PP Masina. *Magnetic properties of $Mg_{1-x}Zn_xFe_2O_4$ nanoferrites and tetracycline-ferrite nanocomposites*. University of KwaZulu-Natal, MSc Dissertation, 2013.

[33] `http://www.electronics-micros.com/img/figure/b-h-curve1.jpg`. Accessed: 2016-11-21.

[34] JZ Msomi, T Moyo, and TB Doyle. Magnetic properties of bulk and nano-sized (Zn, Cu, Cd)$_{0.5}$Ni$_{0.5}$Fe$_2$O$_4$ ferrites. *Journal of Magnetism and Magnetic Materials*, 310(2):2534–2536, 2007.

[35] Scott A Speakman. Basics of x-ray powder diffraction. *Retrieved June*, 12, 2013.

[36] `http://web.utk.edu/~alshibli/research/3DXRD/3dxrd.php`. Accessed: 2016-02-10.

[37] Ahmad Monshi, Mohammad Reza Foroughi, and Mohammad Reza Monshi. Modified scherrer equation to estimate more accurately nano-crystallite size using xrd. *World Journal of Nano Science and Engineering*, 2(03):154, 2012.

103

[38] Phillip Gütlich. Mössbauer spectroscopy principles and applications. *Institut für Anarganische Chemie und Analytische Chemie*, 2002.

[39] NN Greenwood and TC Gibb. *Mossbauer Spectroscopy*. Chapman and Hall Ltd London, 1971.

[40] `http://www.rsc.org/images/simple_spectrum_tcm18-12013.gif`. Accessed: 2016-11-21.

[41] `http://www.rsc.org/Membership/Networking/InterestGroups/` `MossbauerSpect/Intropart1.asp`. Accessed: 2016-03-07.

[42] Alfred G Maddock. *Mossbauer Spectroscopy: Principles and Applications.* Woodhead Publishing, 1997.

[43] `http://geea.lyellcollection.org/content/11/2/129/F5.large.jpg`. Accessed: 2016-04-12.

[44] S. Andriamonje et al. Search for 14.4-keV solar axions emitted in the M1-transition of Fe-57 nuclei with CAST. *JCAP*, 0912:002, 2009. doi: 10.1088/1475-7516/2009/12/002.

[45] Frank J Berry. *Mössbauer Spectroscopy*. Cambridge University Press, 2005.

[46] P Gütlich. Mössbauer spectroscopy in chemistry. In *Mössbauer spectroscopy*, pages 53–94. Springer, 1975.

[47] `http://serc.carleton.edu/research_education/geochemsheets/` `techniques/mossbauer.html`. Accessed: 20015-06-11.

[48] `https://www.researchgate.net/figure/277828439_fig1_` `Fig-1-Four-Probe-Setup-for-Band-gap-measurement`. Accessed: 2016-05-08.

[49] Yeong Il Kim, Don Kim, and Choong Sub Lee. Synthesis and characterization of $CoFe_2O_4$ magnetic nanoparticles prepared by temperature-controlled coprecipitation method. *Physica B: Condensed Matter*, 337(1):42–51, 2003.

[50] M Bahgat, Min-Kyu Paek, and Jong-Jin Pak. Reduction kinetics and mechanisms of $NiFe_2O_4$ with synthesis of nanocrystalline Fe-Ni alloy. *Materials transactions*, 48(12):3132–3139, 2007.

[51] K Maaz, W Khalid, A Mumtaz, SK Hasanain, J Liu, and JL Duan. Magnetic characterization of $Co_{1-x}Ni_xFe_2O_4$ ($0 \leq x \leq 1$) nanoparticles prepared by co-precipitation route. *Physica E: Low-dimensional Systems and Nanostructures*, 41(4):593–599, 2009.

[52] Itegbeyogene P Ezekiel, Thomas Moyo, and Hafiz M I Abdallah. Structural and magnetic properties of $NiFe_2O_4$/NiFe bimagnet and nife nano-alloy synthesized from thermal reduction of $NiFe_2O_4$. pages 32–37. doi: ISBN:978-0-620-70714-5.

[53] Jenő Gubicza, S Nauyoks, Levente Balogh, János Lábár, TW Zerda, and Tamás Ungár. Influence of sintering temperature and pressure on crystallite size and lattice defect structure in nanocrystalline SiC. *Journal of materials research*, 22(05):1314–1321, 2007.

[54] Kwang Mo Noh, Young Bae Lee, Woo Hyun Kwon, Jeoung Yun Kang, Won-Ok Choi, and Kwang Pyo Chae. Crystallographic and magnetic properties of Co, Zn, Ni-Zn substituted nano-size manganese ferrites synthesized by sol-gel method. *Journal of Magnetics*, 21(3):308–314, 2016.

[55] Hafiz MI Abdallah, T Moyo, and JZ Msomi. Magnetic properties of nano-sized $Mg_{0.5}Mn_{0.5}(RE)_{0.1}Fe_{1.9}O_4$ ferrites synthesized by glycol–thermal method. *Journal of Magnetism and Magnetic Materials*, 332:123–129, 2013.

[56] DV Kurmude, CM Kale, PS Aghav, DR Shengule, and KM Jadhav. Super-paramagnetic behavior of zinc-substituted nickel ferrite nanoparticles and its effect on mossbauer and magnetic parameters. *Journal of Superconductivity and Novel Magnetism*, 27(8):1889–1897, 2014.

[57] Sea-Fue Wang, Yung-Fu Hsu, Kai-Mou Chou, and Jeng-Ting Tsai. Effects of co-dopants on the magnetic properties of Ni–Zn ferrites. *Journal of Magnetism and Magnetic Materials*, 374:402–410, 2015.

[58] Amna Hassan, Muhammad Azhar Khan, Muhammad Shahid, M Asghar, Imran Shakir, Shahzad Naseem, Saira Riaz, and Muhammad Farooq Warsi. Nanocrystalline $Zn_{1-x}Co_{0.5x}Ni_{0.5x}Fe_2O_4$ ferrites: Fabrication via co-precipitation route with enhanced magnetic and electrical properties. *Journal of Magnetism and Magnetic Materials*, 393:56–61, 2015.

[59] HF Abosheiasha and ST Assar. Effects of sintering process on the structural, magnetic and thermal properties of $Ni_{0.92}Ca_{0.08}Fe_2O_4$ nanoferrite. *Journal of Magnetism and Magnetic Materials*, 370:54–61, 2014.

[60] E Ranjith Kumar, R Jayaprakash, and Sanjay Kumar. Effect of annealing temperature on structural and magnetic properties of manganese substituted $NiFe_2O_4$ nanoparticles. *Materials Science in Semiconductor Processing*, 17: 173–177, 2014.

[61] KK Bamzai, Gurbinder Kour, Balwinder Kaur, Manju Arora, and RP Pant. Infrared spectroscopic and electron paramagnetic resonance studies on Dy substituted magnesium ferrite. *Journal of Magnetism and Magnetic Materials*, 345: 255–260, 2013.

[62] MA Amer, TM Meaz, M El-Kestawy, and AI Ghoneim. Magnetic and structural studies of trivalent co-substituted Cd–Mn ferrites. *Journal of Magnetism and Magnetic Materials*, 405:137–144, 2016.

[63] MA Ahmed and AA El-Khawlani. Enhancement of the crystal size and magnetic properties of Mg-substituted Co ferrite. *Journal of Magnetism and Magnetic Materials*, 321(13):1959–1963, 2009.

[64] ACFM Costa, E Tortella, MR Morelli, and RHGA Kiminami. Synthesis, microstructure and magnetic properties of ni–zn ferrites. *Journal of magnetism and magnetic materials*, 256(1):174–182, 2003.

[65] E Ranjith Kumar, T Arunkumar, and T Prakash. Heat treatment effects on structural and dielectric properties of mn substituted $CuFe_2O_4$ and $ZnFe_2O_4$ nanoparticles. *Superlattices and Microstructures*, 85:530–535, 2015.

[66] H El Moussaoui, T Mahfoud, S Habouti, K El Maalam, M Ben Ali, M Hamedoun, O Mounkachi, R Masrour, EK Hlil, and A Benyoussef. Synthesis and magnetic properties of tin spinel ferrites doped manganese. *Journal of Magnetism and Magnetic Materials*, 405:181–186, 2016.

[67] Rakesh Malik, S Annapoorni, Subhalakshmi Lamba, V Raghavendra Reddy, Ajay Gupta, Parmanand Sharma, and Akihisa Inoue. Mössbauer and magnetic studies in nickel ferrite nanoparticles: effect of size distribution. *Journal of Magnetism and Magnetic Materials*, 322(23):3742–3747, 2010.

[68] M Ben Ali, K El Maalam, H El Moussaoui, O Mounkachi, M Hamedoun, R Masrour, EK Hlil, and A Benyoussef. Effect of zinc concentration on the structural and magnetic properties of mixed Co–Zn ferrites nanoparticles synthesized by sol–gel method. *Journal of Magnetism and Magnetic Materials*, 398:20–25, 2016.

[69] UR Ghodake, ND Chaudhari, RC Kambale, JY Patil, and SS Suryavanshi. Effect of Mn^{2+} substitution on structural, magnetic, electric and dielectric properties of Mg–Zn ferrites. *Journal of Magnetism and Magnetic Materials*, 407: 60–68, 2016.

[70] E Ranjith Kumar, Aleksandr S Kamzin, and T Prakash. Effect of particle size on structural, magnetic and dielectric properties of manganese substituted nickel ferrite nanoparticles. *Journal of Magnetism and Magnetic Materials*, 378: 389–396, 2015.

[71] JZ Msomi, B Ndlovu, T Moyo, and NSE Osman. Mössbauer and magnetic properties of annealed $Ni_xCo_{1-x}Fe_2O_4$ nanoparticles. *Journal of Alloys and Compounds*, 683:149–156, 2016.

[72] Asghari Maqsood, Kishwar Khan, M Anis-ur Rehman, and Muhammad Ali Malik. Structural and electrical properties of Ni-Co nanoferrites prepared by co-precipitation route. *Journal of superconductivity and novel magnetism*, 24 (1-2):617–622, 2011.

[73] A Pradeep, P Priyadharsini, and G Chandrasekaran. Sol–gel route of synthesis of nanoparticles of $MgFe_2O_4$ and xrd, ftir and vsm study. *Journal of Magnetism and Magnetic Materials*, 320(21):2774–2779, 2008.

[74] M Almokhtar, Atef M Abdalla, and MA Gaffar. Phase analysis study of copper ferrite aluminates by x-ray diffraction and mössbauer spectroscopy. *Journal of magnetism and magnetic materials*, 272:2216–2218, 2004.

[75] Raul Gabbasov, Michael Polikarpov, Valery Cherepanov, Michael Chuev, Iliya Mischenko, Andrey Lomov, Andrew Wang, and Vladislav Panchenko. Mössbauer, magnetization and x-ray diffraction characterization methods for iron oxide nanoparticles. *Journal of Magnetism and Magnetic Materials*, 380: 111–116, 2015.

[76] Steen Mørup. Mössbauer effect in small particles. *Hyperfine interactions*, 60 (1-4):959–973, 1990.

[77] L Ben Tahar, M Artus, S Ammar, LS Smiri, F Herbst, M-J Vaulay, V Richard, J-M Grenèche, F Villain, and F Fievet. Magnetic properties of $CoFe_{1.9}RE_{0.1}O_4$ nanoparticles (RE = La, Ce, Nd, Sm, Eu, Gd, Tb, Ho) prepared in polyol. *Journal of Magnetism and Magnetic Materials*, 320(23):3242–3250, 2008.

[78] J Blanusa, B Antic, A Kremenovic, AS Nikolic, L Mazzerolles, S Mentus, and V Spasojevic. Particle size effect on Néel temperature in Er_2O_3 nanopowder synthesized by thermolysis of 2, 4-pentadione complex. *Solid State Communications*, 144(7):310–314, 2007.

[79] Xiangdong Meng, Haibo Li, Jingyan Chen, Liu Mei, Keqiang Wang, and Xiao Li. Mössbauer study of cobalt ferrite nanocrystals substituted with rare-earth Y^{3+} ions. *Journal of Magnetism and Magnetic Materials*, 321(9):1155–1158, 2009.

[80] G Dascalu, T Popescu, M Feder, and OF Caltun. Structural, electric and magnetic properties of $CoFe_{1.8}RE_{0.2}O_4$ (RE = Dy, Gd, La) bulk materials. *Journal of Magnetism and Magnetic Materials*, 333:69–74, 2013.